THE DESIGN OF MULTIFUNCTIONAL HYDROGEL NANOPARTICLES FOR DRUG DELIVERY

A Dissertation
Presented to
The Academic Faculty

by

Michael Hughes Smith

In Partial Fulfillment
of the Requirements for the Degree
Doctor of Philosophy in the
School of Chemistry and Biochemistry

Georgia Institute of Technology
May 2012

THE DESIGN OF MULTIFUNCTIONAL HYDROGEL NANOPARTICLES FOR DRUG DELIVERY

Approved by:

Dr. L. Andrew Lyon, Advisor
School of Chemistry and Biochemistry
Georgia Institute of Technology

Dr. Robert Dickson
School of Chemistry and Biochemistry
Georgia Institute of Technology

Dr. Jiri Janata
School of Chemistry and Biochemistry
Georgia Institute of Technology

Dr. Facundo Fernandez
School of Chemistry and Biochemistry
Georgia Institute of Technology

Dr. Anselm Griffin
School of Materials Science and Engineering
Georgia Institute of Technology

Date Approved: February 9, 2012

This dissertation is dedicated to the memory of Daniel Jacques Marcus
(February 6, 1985 - January 27, 1998)

ACKNOWLEDGEMENTS

I wish to thank my family for all of their support over these years, including my parents, brother and sister. Their kindness, sense of humor, and enthusiasm for this research has kept me pushing towards my goals. I also wish to thank my wonderful wife, Sarah, for all of her help and for the happiness she has brought into my life. I owe an enormous debt of gratitude to the scientists of the Lyon group. I have been so fortunate to work with these talented and creative people. In particular, Jeffrey Gaulding and Grant Hendrickson have helped me in many aspects of my work, from experimental design to generating new hypotheses and ideas. I would also like to thank Erin Dickerson, Toni South, William Blackburn, Kimberly Clarke, Emily Herman, Xiaobo Hu, Mark Spears, and many others. Most of all, I would like to thank Andrew Lyon for giving me the chance to participate in his research program. I want to thank Professor Lyon for his wisdom, patience, and for all of the opportunities that he has provided.

I decided to dedicate this dissertation to the memory of Daniel “Dan the Man” Marcus. Growing up in Larchmont, New York, Dan and I were friends since early elementary school. Of all of the memories I have of Dan, I distinctly remember his love of Erector sets, model roller coasters, and his curiosity for all things science. Whereas I would fold paper planes that would crash feet in front of me, Dan would diligently review books on the subject and construct multi-component paper aircraft that would glide gracefully across the neighborhood. His intellect and talents were an inspiration, and a great motivator for my work. I want to thank Dan’s parents, Steve and Emily Marcus, for all of their support after his passing.

TABLE OF CONTENTS

LIST OF TABLES

LIST OF FIGURES

LIST OF SCHEMES

LIST OF SYMBOLS

r_h	Hydrodynamic radius
M_w	Weight-average molar mass
r_{rms}	Root-mean-square radius
A2	Second Virial Coefficient
r_g	Gravimetric radius
I	Intensity of scattered light
I_0	Intensity of incident light
α	Polarizability of scatterer
θ	Scattering angle
λ	Wavelength
r	Distance between detector and scattering volume
c	Concentration
$R(\theta)$	Rayleigh ratio
K	Optical constant
n_0	Refractive index of solvent
dn/dc	Refractive index increment
V	Scattering volume
N_A	Avogadro's number
$P(\theta)$	Scattering form factor
k	Boltzmann's constant
η	Viscosity
T	Temperature
t^0	Void time

V^0	Void volume
V_c	Crossflow rate
w	Channel thickness
t_R	Retention time
D	Diffusion coefficient
ε_0	Relative dielectric constant
ε	Electrical permittivity
v_E	Electrophoretic mobility

LIST OF ABBREVIATIONS

PLGA	Poly(lactic-co-glycolic acid)
LHRH	Luteinizing Hormone-Releasing Hormone
NIPAm	*N*-isopropylacrylamide
NIPMAm	*N*-isopropylmethacrylamide
BIS	*N,N'*-methylenebis(acrylamide)
AAc	Acrylic acid
DMAEMA-Q	[2-(methacryloyloxy)ethyl]trimethylammonium chloride
PEG	Poly(ethylene glycol)
DMHA	*N,O*-(dimethacryloyl)hydroxylamine
DHEA	(1,2-dihydroxyethylene)bisacrylamide
APS	Ammonium persulfate
KPS	Potassium persulfate
v50	2,2'-azobis(2-methylpropionamidine)dihydrochloride
DTA	Dodecyltrimethylammonium bromide
SDS	Sodium dodecyl sulfate
AFA	Acrylamido fluorescein
EDC	1-ethyl-3-methyl-(3-dimethylaminopropyl)carbodiimide
NHSS	*N*-hydroxysulfosuccinimide
EMCA	*N*-ε-maleimidocaproic acid
LCST	Lower Critical Solution Temperature
VPTT	Volume Phase Transition Temperature
MPS	Mononuclear Phagocyte System

RES	Reticuloendothelial System
EPR	Enhanced Permeability and Retention
EGF	Epidermal Growth Factor
BBB	Blood Brain Barrier
siRNA	Small Interfering Ribonucleic Acid
RNAi	RNA Interference
DLS	Dynamic Light Scattering
MALS	Multiangle Light Scattering
A4F	Asymmetrical Flow Field-Flow Fractionation
CG-SLS	Composition Gradient Static Light Scattering
NTA	Nanoparticle tracking analysis
RGD	Rayleigh-Gans-Debye Model
MWCO	Molecular Weight Cut-Off
EphA2	Erythropoietin-producing hepatocellular receptor
RCF	Relative Centrifugal Force

SUMMARY

The application of therapeutic proteins and small interfering RNA (siRNA) molecules for disease treatment is an important yet challenging concept in modern medicine. To date, billions of dollars have been invested in the development of various drug candidates. However, the poor pharmacological properties of those compounds continue to limit progress towards viable human therapeutics, especially when intravenous delivery routes are considered. For instance, biological macromolecules are often incapable of targeting disease sites, can be immunogenic, or they can induce toxicity at off-target tissues. In response to the shortcomings of siRNA and protein drugs, many nanoparticle carriers are being pursued. Nanoparticles are designed to encapsulate, protect, and transport therapeutics to diseased cells. To be effective in this role, the delivery vehicle must overcome a series of biological hurdles over the course of delivery. Thus, dynamic, multifunctional nanoparticles are needed that can perform multiple in vivo functions.

Hydrogel particles are a unique class of polymeric biomaterials for drug delivery applications. Depending on their diameter, particles are either categorized as nanogels (less than 100 nanometers) or microgels (up to several micrometers). Similar to macroscopic hydrogels, nanogels and microgels contain a large fraction of water within their structure, can retain their architecture despite mechanical stress, and are generally soft/pliable. Particles are composed of synthetic hydrophilic polymers, cross-linked into porous networks that are capable of encapsulating and releasing macromolecules. In

addition to those features, stimuli-responsive nanogels and microgels may be synthesized by incorporating responsive polymers into the hydrogel matrix.

In this dissertation, nanogels and microgels were investigated as candidate vehicles for macromolecule therapeutics, including siRNA and proteins. Chapter 1 is provided for additional background into the physicochemical properties of the particles. The chapter also discusses the relevant biological barriers faced by the vehicles during intravenous delivery, chemistries that may improve disease targeting, and factors that govern biocompatibility. In Chapter 3, proof-of-principle experiments show the utility of multifunctional nanogels for siRNA delivery. Using simple core/shell nanogel architectures, siRNA molecules were delivered to chemosensitize drug resistant ovarian cancer cells *in vitro*. In Chapter 4 biodegradable nanogels were synthesized that may enable the clearance of the vehicles following repeated administration *in vivo*. Chapter 5 describes the detailed assessment of microgels that rapidly decompose in response to sodium periodate. The decomposition revealed key differenced in network composition for microgels composed of two different thermoresponsive polymers. In Chapter 6, charge microgels were investigated for the encapsulation of a model therapeutic protein. The loading of the protein was found to be tunable with respect to the chemistry of the hydrogel network. Chapter 7 is provided to summarize in-progress projects to modulate the loading of siRNA, and improve targeting and stealth for those vehicles. The chapter also proposes new avenues of research to improve the carriers.

New light scattering methods were developed in this dissertation to provide detailed, direct assessments of the particle properties. For example, through multiangle light scattering (MALS) the decomposition of microgels (Chapters 4 and 5) was

monitored through changes in particle molar mass from network erosion. In another example, the loading of proteins within various microgels and nanogels was assessed through changes in particle molar mass (Chapter 6 and 7). To explain those methodologies, Chapter 2 is provided to briefly review some light scattering principles used in the work. Together, the chapters of this dissertation reveal nanogels and microgels as promising carriers for macromolecule drug candidates. By combining the knowledge gained throughout this work, next-generation carriers may be pursued with improved performance in the treatment of disease.

CHAPTER 1

INTRODUCTION

Adapted from

Smith MH, Lyon LA. *Acc. Chem. Res.*, 2012 (ASAP) DOI: 10.1021/ar200216f

Hendrickson GR*, Smith MH*, South AB*, Lyon LA. *Adv. Funct. Mater.* 2010, 20, (11), 1697-1712
**equal contributing author*

Smith MH, South AB, and Lyon LA in Hydrogel Micro and Nanoparticles, *Wiley-VCH,* 2012 (in press)

1.1 Polymeric Biomaterials and Drug Delivery

Biomaterials have enabled profound contributions to medicine over the last several decades, from extracorporeal devices, like contact lenses and kidney dialyzers, to implantable devices, including vascular grafts and pacemakers.[1] These materials are designed to interface with biological tissues and are capable of either augmenting, interacting with, or replacing natural functions in the body.[1] The diverse range of biomaterial functionalities has led to the treatment of several diseases and has deeply impacted medicine as a whole.

British ophthalmologist Harold Ridley developed some of the earliest applications of implantable polymers. While observing wounds to the eyes of fighter pilots following World War II, Ridley noticed that imbedded shards of the Spitfire canopy (poly(methyl methacrylate)) had a tendency to heal without excessive inflammation and infection. These early observations led to the first intraocular device for the treatment of cataracts.[2] Millions of these devices are now used in the treatment of ocular disease each year.

The implementation of many other biomaterials also came in the post-war biomedicine boom. Like the implants inspired by the Spitfire canopy, these treatments typically used nonspecific, off-the-shelf components that were readily available. For

example, the first artificial kidney was inspired by the first hemodialysis machine invented by Willem Kolff. The Kolff machine employed cellulose acetate for dialysis tubing, a material commonly used at the time for sausage casing. Other significant medical devices would also include commodity plastics in their design. Early vascular grafts used a common textile polymer known as Dacron, introduced in 1950 by DuPont. Despite the fact that off-the-shelf materials were applied in those examples, the devices were effective in the treatment of medical problems. However, serious conflicts could also result from their use. Early dialysis tubing had an increased risk of platelet activation. Likewise, Dacron grafts were limited in their diameter and also increased the likelihood of clot formation. These limitations have motivated the development of more specific materials that are safer at the biological interface.

One of the principal limitations of early polymeric biomaterials was their lack of compatibility with living tissues, or biocompatibility. All biomaterials, whether implanted or injected, experience what is described as the 'wound healing response' when administered to the body. This response occurs after injury, such as an incision, resulting in inflammatory responses, foreign body reactions, and fibrous encapsulation of the biomaterial, medical device, or prosthesis.[3] As safer and more effective biomaterials are developed for medical applications, their chemical, physical, and biological properties must be improved to either reduce or mediate the host response.

By the 1970s, many researchers were interested in imparting drug-releasing properties to polymeric materials. In particular, the delivery of macromolecules, such as peptides, proteins, or oligonucleotides had become attractive. Large-quantity production of these high molar mass drugs became possible through advancements in genetic engineering, providing new possibilities for disease treatment. However, those molecules generally showed poor characteristics in vivo, such as rapid degradation or recognition by the immune system. By encapsulating macromolecule therapies within polymeric devices, the drugs could be protected from immediate destruction and would be delivered

to specific regions of the body (avoiding off-target effects and toxicity). The first peptide-eluting biomaterial was approved in 1989 by the U.S. Food and Drug Administration (FDA). The material was composed of a poly(lactic-co-glycolic acid) (PLGA), a copolymer that is susceptible to ester hydrolysis in water. For instance, microparticles are formed by mixing PLGA with macromolecules in certain organic solvents (i.e. dichloromethane).[4] The hydrophobicity of the particle prevents water from penetrating and degrading the interior polymer matrix, while erosion at the water interface drives the release of encapsulated macromolecules. Thus, by tuning the ratio of hydrophobic and hydrophilic components of PLGA (i.e. the ratio of lactic and glycolic acid, respectively), the rate of water penetration, polymer degradation, and subsequent drug release may be tuned from hours to months. The FDA-approved device, leuprolide acetate (Lupron Depot®), was formulated for the slow release of luteinizing hormone-releasing hormone (LHRH). The polymer system has become one of the most widely applied devices for treating advanced prostate cancer, endometriosis, and precocious puberty. In addition to this device, an array of other polymeric materials has been introduced, that are profoundly impactful for modern medicine.[5-7]

There are generally two delivery routes for polymeric devices: localized delivery, where therapies are administered directly to the tissue of interest, or systemic delivery (i.e. intravenous injection), where formulations are administered into the bloodstream. Although localized delivery has the benefit of enhancing bioavailability and reducing adverse effects, many tissues can only be reached through the systemic route. Intravenous delivery technologies are challenging, usually involving circulating nanoparticle carriers that must protect the drug cargo from degradation by serum nucleases, resist recognition by the immune system, and show tissue-specific uptake via cell targeting.

Multiple colloidal materials have been investigated for their potential as delivery vehicles, including liposomes,[8-11] metallic and semiconductor nanoparticles,[12-18] surfactant and block copolymer micelles,[19-20] and other polymeric constructs.[21-27]

Although the physicochemical properties of these materials differ drastically, many of the sample principles apply for efficacy in vivo. In order to achieve a high therapeutic index, these constructs require (1) the ability to encapsulate, protect, and release loaded solutes in a predictable fashion, (2) remain in circulation while avoiding an immune response (which may hinder the transit of nanoparticles), (3) localize specifically at the diseased site of interest, and (4) occupy the tissue for a reasonable duration for possible uptake by diseased cells and solute delivery.[28-30]

This dissertation discusses the design of hydrogel nanocarriers (nanogels or microgels) for application as intravenous delivery vehicles. In contrast to the colloidal materials described above, hydrogel particles have several useful characteristics as biomaterials and drug vectors.

1.2 Hydrogels and Hydrogel Nanoparticles

Hydrogels are a promising class of biomaterials for medical applications, including biological sensing, drug delivery, and tissue regeneration. These materials are generally very well-hydrated (absorbing up to 90-99% water by weight) and have an elastic structure.[31] This hydrated, or hydrophilic, property reduces the tendency for proteins to nonspecifically adsorb to the hydrogel, thus imparting "non-fouling" characteristics. The structure of a hydrogel is usually an elastic network of polymers that can encapsulate biological molecules and therapeutics. Through modification of the density of the network, the mechanical properties of the material can be changed to suit their application.

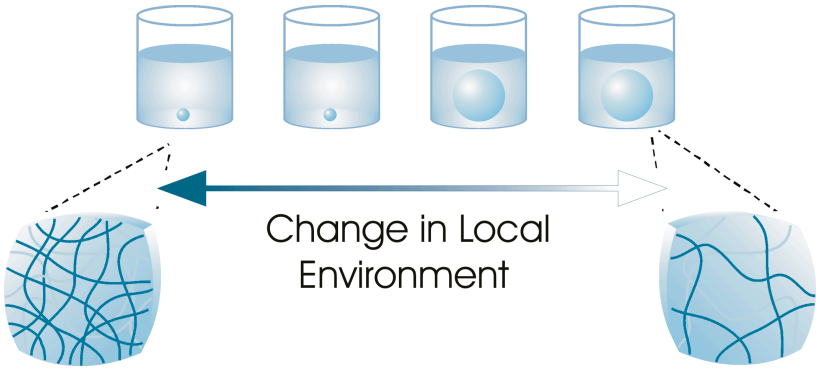

Figure 1.1 Schematic representing the volume phase transition of a responsive hydrogel.

Additionally, hydrogels may be designed to undergo a volume phase transition in response to an external stimulus.[32] A volume phase transition occurs when the network transitions between a solvent-swollen network and a hydrophobic collapsed state due to a change in network solvation. As can be seen in **Figure 1.1,** polymer chain-chain interactions dominate in the collapsed state, resulting in the expulsion of water from the network. In the swollen state, the interactions between the solvent and the polymer chains dominate. Using this principle, a variety of microgels have been engineered to respond to varying pH conditions,[33] light,[34-35] ionic strength,[36] and the presence of macromolecules.[37-39] In the domain of responsive hydrogels, the most commonly studied are those composed of thermoresponsive polymers, which undergo dramatic changes in network swelling as function of temperature.[40]

The most widely studied class of thermoresponsive microgels are those composed of *N*-isopropylacrylamide (NIPAm). At temperatures above ~31 ºC, poly(NIPAm) undergoes an endothermic, entropically-driven phase transition from a random coil to a collapsed globule.[41-42] At low temperatures, pNIPAm interacts with water by hydrogen bonding (primarily through the amide side chains). Additionally, the isopropyl group causes structuring of water, promoting the entropically-driven polymer-polymer interaction (i.e. via the hydrophobic effect). As solution temperatures are elevated, polymer-polymer interactions are favored as hydrogen bonding with the solvent becomes

weaker. The polymer reorganizes to a collapsed globule as the polymer-polymer interactions become dominant, resulting in the expulsion of water. This phase change occurs at a discrete temperature known as the lower critical solution temperature (LCST). When observed in cross-linked networks, the transition temperature is often referred to as the volume phase transition temperature (VPTT).[43-44]

1.2.1 Microgel Synthesis

Free radical precipitation polymerization is a convenient approach to produce microgels or nanogels. This method exploits the thermally-triggered collapse of growing polymer chains to self-assemble the microgel,[45] often resulting in narrow particle size distributions at high yield. For instance, poly(*N*-isopropylacrylamide) (pNIPAm) undergoes an abrupt coil-to-globule transition at ~31 ºC.[46] Typical syntheses are performed by dissolving the monomer (e.g. NIPAm), other comonomers, and a cross-linking agent (e.g. *N,N'*-methylenebis(acrylamide), BIS) in water. The reactants are subsequently heated to a temperature between 60 and 70 ºC (above the LCST). After purging the solution with N_2, the polymerization is initiated by addition of initiator (e.g. ammonium or potassium persulfate, APS/KPS). At these reaction temperatures, persulfates thermally decompose to form sulfate radicals that initiate polymerization. The sulfate radicals attack the NIPAm monomer, which then undergoes chain growth via radical propagation. At a critical chain length (~10 monomer units), the polymer collapses to form a globular particle. The particles then grow in mass by the capture of oligoradicals, monomer addition, or aggregation with other nuclei.[47]

Size is a critical characteristic for several microgel applications. For example, smaller particles (~50-200 nm in diameter) are favorable for intravenous drug delivery applications, where *in vivo* behavior depends greatly on colloidal dimensions.[48] Precipitation polymerization is an enabling scheme for obtaining a wide range of

microgel sizes, where fine control over dimensions is achieved through modification of synthetic components and conditions.

Recently, a new protocol was demonstrated for the synthesis of larger diameter (2.5-5 μm), pH- and temperature-responsive microgels by surfactant-free emulsion polymerization.[49] This size is not traditionally obtainable by dispersion polymerization methods. To accomplish such sizes, we used a temperature ramp from 45 °C to 65 °C during the nucleation stage of the polymerization. In this synthetic scheme, initiation is performed at a much lower temperature. The initiator thermally decomposes at a slower rate, reducing the oligomeric radical concentration and the overall abundance of collapsed nuclei. Additionally, the monomer concentration is higher at this time of the reaction. These conditions favor a higher chain propagation rate than initiation rate, and the growth of fewer, larger nuclei.[49] As the reaction proceeds and monomer is consumed, the propagation rate decreases. The temperature ramp compensates for this, where the temperature was slowly elevated to increase the reaction kinetics.

In contrast, much smaller particles are produced when syntheses are performed at higher temperatures, and when stabilizing agents are added to the system. Specifically, the use of ionic surfactants has yielded nano-sized hydrogel particles (nanogels) via precipitation polymerization. Surfactants likely assist in precursor particle stabilization, decreasing the probability of hydrophobic nuclei aggregation.[47] Thus, nanogel growth likely occurs mainly through oligomer or monomer addition, instead of nuclei fusion. In this scheme, a larger number of small particles are formed as compared to surfactant-free synthesis conditions.

1.2.2 Core/Shell Particle Synthesis

Others have demonstrated the utility of adding hydrogel shells to “hard” nanoparticles (e.g. polystyrene, silica,[50] iron oxide, gold [51]). The resultant particles showed properties governed by the chemistry of the added polymer. Through hydrogel

shell addition, chemical functionalities could be localized in the particle periphery,[36, 52] stimuli-responsive characteristics may be imparted,[53] or the stability of the particles could be enhanced.[54-55] Inspired by those results, the Lyon research group was the first to explore the synthesis of core/shell particle architectures composed entirely of hydrogel.[45] Such core/shell microgels showed intriguing properties, wherein different stimuli-responsive components and chemical functionalities could be imparted into different compartments of a single particle. Since the first report of core/shell microgels in 2000, a number of higher order architectures have been investigated, each demonstrating interesting features in the context of drug delivery. Those particles include multi-shelled structures,[56] erodible particles,[57-59] hollow microgel capsules,[60] and "yolk" shell spheres (**Figure 1.2**).[56]

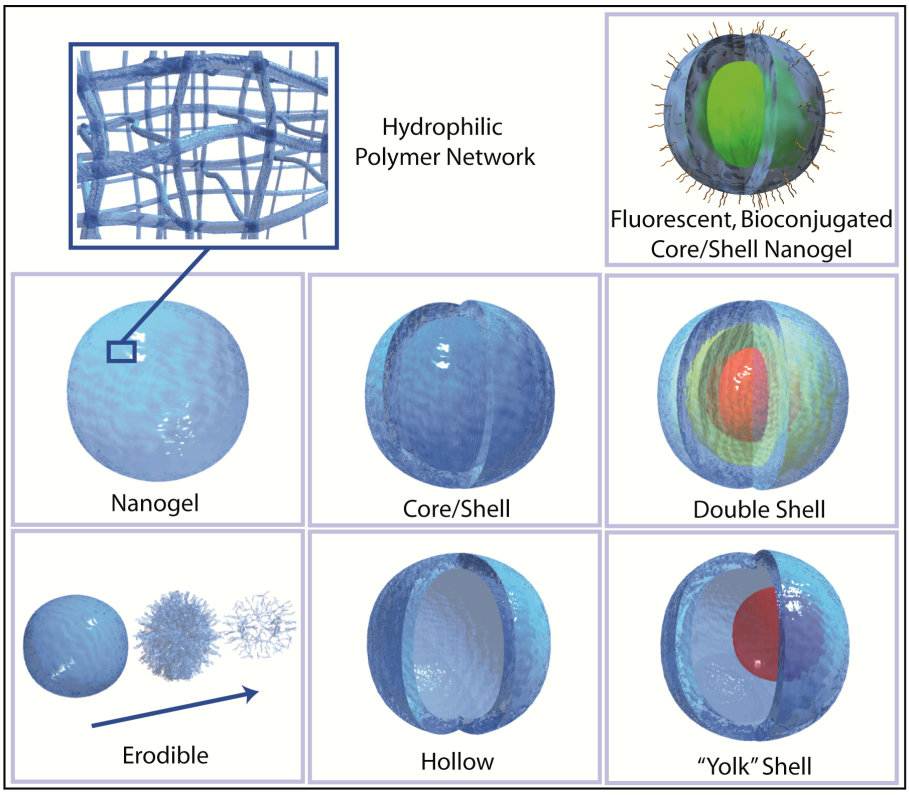

Figure 1.2 Summary of higher-order hydrogel particles reported in recent years. Adapted from reference 61.

Although many of those architectures are being pursued for general drug encapsulation and release properties, the most progress towards drug delivery applications has been with core/shell nanogels. Core/shell nanogels are produced via a "seed and feed" method that involves a two step reaction strategy.[45] In the first step, core particles are synthesized using the method described above (Section 1.2.1). Once a core is synthesized, a hydrogel shell with the desired composition and properties is added. In a typical reaction, the core particles are heated to a temperature above the LCST of the polymer (commonly 70 ºC) and a monomer solution is added to make up the shell composition. The mixture is purged with N_2, and subsequently initiated via the addition of persulfate (APS/KPS) and reacted for several hours. Collapsed microgel cores are hydrophobic under these reaction conditions (above the LCST of the polymer), which promotes the capture of any oligomers formed in solution. It is important to note that the "seed and feed" method requires all oligomers formed in the reaction to precipitate on preformed core particles, otherwise homonucleation of the shell polymer may occur where a second population of microgels is generated. To prevent the homonucleation of shell polymer, optimization is required with respect to the concentration of core particles, initiator, surfactant, and shell monomer. To achieve small particle sizes desired for intravenous application (≤ 100 nm in diameter), syntheses are performed with stabilizing agents added to the system, such as ionic surfactants. Stabilizing components prevent hydrophobic nuclei fusion during precipitation polymerization, thereby promoting particle growth mainly by oligomer or monomer addition.[47]

1.3 Physicochemical Properties of Core/Shell Nanogels

In previous sections, the versatility of microgels and nanogels was briefly described. Through modification of the monomeric components, cross-link density, and other synthetic conditions, a great diversity of microgel species may be generated with unique and often complex physicochemical properties (e.g. swelling or stimuli-

responsivity). In this section, the influence of shell addition on the behavior of microgels is described. For example, we have demonstrated that an added shell can reveal cross-linker heterogeneity within the particle,[62] induce core compression, and modulate the swelling kinetics and thermodynamics of the resulting microgels. An understanding of these characteristics is critical in the design and application of core/shell microgels.

1.3.1 Swelling Thermodynamics

The original core/shell microgels reported by Jones et al. displayed stimuli-responsive behavior and swelling properties that were dependent on the distribution of functional groups within the architecture.[63] Specifically, the location of acidic comonomers such as Acrylic Acid (AAc) significantly affected the VPTT of the resulting microgel. For example, core particles composed of pNIPAm-AAc showed pH-dependent swelling behavior, and had higher VPTT values as the pH was increased from 3.5 to 6.5. These results were attributed to the increased osmotic pressure and Coulombic repulsion caused by the deprotonation of AAc and ingress of solvated ions, which increases swelling and inhibits chain collapse.[64-65] However, the swelling behavior of pNIPAm-AAc core particles was significantly modulated through addition of a pNIPAm shell. After a shell was added, two phase transition temperatures were observed. Whereas the magnitude of shell collapse at 32 °C was strong, the extent of core collapse was greatly hindered. The VPTT associated with the core was greatly depressed at pH 6.5 due to shell-dominated behavior.[63] This behavior was attributed to a compression effect caused by shell addition, which decreases the average inter-chain distance in the core, and thus depressed core VPTT values. When pNIPAm-AAc was conversely localized in the particle shell (with a pNIPAm core), the pNIPAm core had less influence over the swelling of the pNIPAm-AAc copolymer shell. When localized in the shell, less physical restriction to pH-induced swelling was observed for pNIPAm-AAc.[63]

These studies revealed the complexity of the phase transition behavior of core/shell particles. For constructs composed of different hydrogel components, the physicochemical properties of the resulting microgel cannot be easily anticipated through the sum of the individual hydrogel properties. Instead, it is the exterior of a microgel that takes a dominant role in the thermodynamics of particle collapse. The microgel periphery is typically involved in the initial stages of the phase transition, which likely causes this behavior.[66-67] Thus, the chemistry of the shell has mechanical and chemical influence over the solvation of the core compartment.[68]

1.3.2 Network Heterogeneity and Core Compression

As described in previous sections, the presence of cross-linking agents in synthesis is critical for network stability. For example, microgels synthesized via precipitation polymerization require cross-links to prevent polymer dissolution when cooled below the VPTT. Cross-linking is an important structural parameter not only for the basic mechanical properties of microgels systems (degree of particle solvation, equilibrium swelling volume), but also for the density (mesh size) and dimensions (hydrodynamic diameter) of the resulting particles.[69-70] Since the distribution of segments within the network is heavily influenced by the amount of cross-linker used in synthesis, we cannot easily consider microgels as homogenous spheres. For instance, lightly cross-linked pNIPAm particles (< 7 mol% BIS) show a radial distribution of cross-links throughout the particle. Particles of this type are typically described through a "gradient model", since cross-linker distribution is highest near the particle center. This effect is caused by a faster incorporation rate of BIS during particle growth, resulting in an inhomogeneous distribution of cross-links.[44, 70-71] In contrast, particles with higher cross-linker content (> 7 mol% BIS) are not effectively described by the gradient model.[72] Instead, these microgels resemble a compact gel particle, with perhaps a more random

distribution of highly cross-linked regions. These particles typically show less network solvation, swelling, and a higher internal density of polymer chains.

The morphology of microgel particles is further complicated by the addition of a shell compartment. Specifically, adding a shell via the "seeded" precipitation polymerization scheme often induces compressive forces on the core. Depending on the morphology of the core particles, the magnitude of compression may vary. For example, Jones et al. showed that for loosely cross-linked particles, the size of resulting core and core/shell particles below the VPTT were identical.[73] Evidence of shell addition is only seen when the two particles are compared in the collapsed state (above the VPTT). For this particle type, shell addition restricts the swelling of the core, resulting in a core compression effect. In contrast, when higher cross-link density (10 mol% BIS) particles are employed as the core, a size increase was observed at all temperatures following shell addition.[73] These data suggest that core particles containing fewer cross-links are perturbed to a larger extent through shell addition than highly cross-linked microgels.

Multiple other factors influence the magnitude of compression induced by a shell, including the presence of charge in the core,[73] and the overall thickness of the added shell layer.[74] By increasing the amount of monomer present during shell addition, Jones et al. modulated the thickness of the resulting shell.[74] For loosely cross-linked microgels (~2 mol% BIS), particle size increased systematically as a function of shell thickness at temperatures both above and below the particle VPTT. However, the size increase was much more apparent for particles in the collapsed state, which suggests shell-restricted swelling (or compression) of the cores.[74] Particles with a higher cross-link density (~10 mol% BIS) showed less perturbation of the core swelling. For the loosely cross-linked microgels, Jones et al. showed that the shell thickness decreased the ability of the core to swell to its original volume.[74] A similar effect was observed for the higher cross-linked system, but the effect was less pronounced.

1.4 Factors influencing biocompatibility and targeting

In subsequent chapters of this dissertation, nanogels are described that were rationally designed to be effective carriers for proteins and small interfering RNA (siRNA) via intravenous routes of administration. To motivate that work, it is important to describe the factors influencing the biocompatibility of the nanogel, and methods to target tumors intravenously.

1.4.1 Nanoparticles and The Mononuclear Phagocytic System

The intravenous administration of targeted nanocarriers is an attractive option for the treatment of cancer, where particles in circulation will reach malignant sites regardless of their location in the animal (e.g. metastatic tumors). However, the ability of a nanogel to effectively target and deliver cargo depends on whether it can circulate long enough to reach its therapeutic site of action. The dimensions of the polymeric material have a significant impact on blood circulation time and the overall bioavailability.[29, 75-80] For example, materials below approximately 50,000 Daltons can be cleared through the kidney.[25] This mass correlates to a particle size of roughly 5-10 nm, resulting in rapid removal through organ extravasation and renal clearance. Particles above this regime are more likely cleared through the mononuclear phagocytic system (MPS) (also known as the reticuloendothelial system).[80]

The MPS is one of the largest biological barriers for virtually all long-circulating nanoparticles in development. This process involves monocytes and macrophages, which are primarily assembled in MPS-related organs such as the spleen, liver, and lymph tissue. The primary function of these cells is in the recognition of foreign materials, in circulation. Nanoparticles are affected by the MPS almost immediately upon intravenous injection, where serum proteins begin interacting with the surface of the nanocarrier.[81] When a nanoparticle encounters blood serum proteins (opsonins), there is a tendency for the protein to stick to the particle through various attractive forces (including van der

Waals, electrostatic, ionic, and hydrophobic).[25] This process is known as opsonization, which makes the nanoparticles much more visible to phagocytic macrophages. Additionally, integrin receptors on macrophages bind a variety of extracellular matrix components and blood proteins (fibronectin, vitronectin) or IgG and IgM antibodies.[82] Finally, ligand-receptor complexation may be mediated by the presence of active cytokines and growth factors. Clearly this is a biologically complex process, where the specific relationship between the physicochemical properties of the polymers, opsonins, macrophages, inflammatory cytokines and growth factors is not fully understood.[83]

In general, there are two types of the mononuclear phagocytes responsible for MPS clearance; circulating monocytes of peripheral blood and fixed, non-circulating tissue macrophages found throughout the body. These non-circulating cells include Knupffer cells of the liver, histocytes in multiple tissues, and phagocytes of the spleen.[30] Once associated with opsonins, macrophages may engulf the foreign material by phagocytosis, resulting in enzyme secretion along with other oxidative-reactive chemical factors to break down the phagocytosed material.

1.4.2 Size and Surface Modification for Enhanced Delivery

Particle size is an important factor in the biodistribution of the material. As previously described, materials with a hydrodynamic diameter less than 5 nm (or 50,000 Da, conservatively), will be removed from the body by the renal system. Particles with diameters significantly larger (~200 nm) demonstrate longer circulation times, where clearance occurs through spleen sequestration and mechanical filtration, and will eventually be removed by the MPS.[29, 77] Particles in the range of 10–70 nm have been considered ideal for long circulation since they are large enough to penetrate smaller capillaries in various body tissues and typically have longer circulation times than similar materials of larger dimensions.[29, 76, 84] If we consider the fact that particles smaller than 100 nm may be enclosed within endocytic vesicles,[85] it becomes clear that particles

within the size range from 10 – 100 nm may be ideal for circulation, accumulation at sites of interest and may participate in endocytosis at the tumor site.

The physical and chemical properties of the nanoparticle surface play an important role for protein adsorption. Extensive efforts have been made in elucidating the mechanism by which opsonins adhere to polymers, and techniques to minimize or slow the opsonization process. As described previously, opsonins adhere to nanoparticles through interactions of varying strength.[25] The importance of the hydrophilic/hydrophobic nature of particles has been observed, where proteins seem to have a higher binding affinity for more hydrophobic surfaces.[86-87] Additionally, ionic character on the nanoparticle surface may dramatically affect opsonization. For example, Tabata et al. have demonstrated the role of nanoparticle surface charge density on the rate of phagocytosis *in vitro.* Phagocytosis is enhanced as the absolute value of zeta potential increases for both negative and positively charged surfaces on the delivery vehicle.[88] In consideration of nanogel circulation, the physicochemical properties of the particle must be considered if opsonin adhesion is to be reduced.

A common method used to slow opsonization is to graft certain polymers to the surface of the nanoparticle, shielding electrostatic and hydrophobic interactions. Multiple species of long hydrophilic polymer chains and non-ionic surfactants have been employed with varying success, including polysaccharides, polyacrylamide, poly(vinyl alcohol), poly(N-vinyl-2-pyrrolidone), and poly(ethylene glycol).[25] These polymers have a high hydrophilicity, are very flexible, and may be capable of shielding hydrophobic and charged particles from blood proteins. Of the multitude of polymers investigated for shielding properties, the most commonly employed and effective material is poly(ethylene glycol) (PEG), and PEG-containing copolymers. PEG is an uncharged, hydrophilic, and non-immunogenic polymer that can be grafted, copolymerized, or adsorbed in the synthesis of polymeric materials.[89-90] The incorporation of PEG may lead to an enhancement in biocompatibility and enhanced stabilization of colloid materials.

The properties that PEG may impart on the nanomaterial is largely dependant on the molecular weight, density, conformation, and flexibility of the chains.[91-92] As can be seen in **Figure 1.3**, density of PEG on the periphery of a particle contributes to it's conformation.

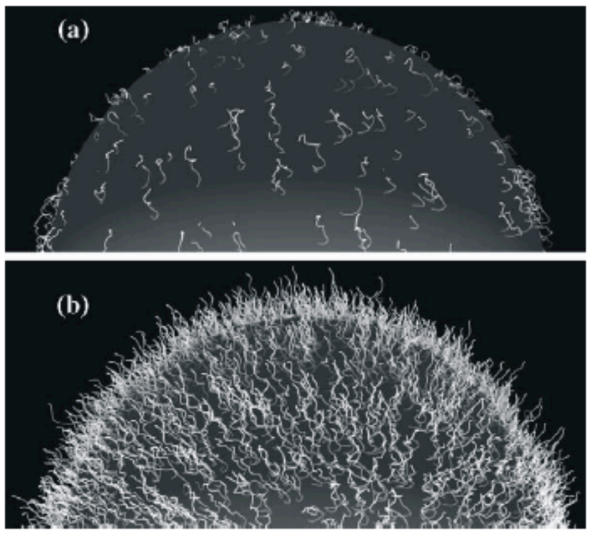

Figure 1.3 Schematic representation of PEG brushes on the periphery of a nanoparticle. Low coverage (a) leads to a "mushroom" topography, whereas high coverage (b) contributes to a "brush" configuration of PEG. Adapted from Ref 91**.**

There have been several theories proposed to explain the mechanism of protein resistance and the described "stealth" effect caused by PEG incorporation. For example, the hydrophilic and flexible nature of the PEG chains allows them to take on an extended conformation in solution. As proteins interact the surface of the particle they encounter extended surface PEG chains and attempt to compress them into the particle. The PEG chains are being forced into a higher energy, compressed, conformation which causes an opposing repulsive force that effectively blocks or repulses the incoming protein.[91-92] If the thickness of the PEG coating is sufficient, opsonization may be hindered *in vivo.*

1.4.3 Active and Passive Cellular Targeting

Intravenously injected particles are commonly targeted to tumors through the enhanced permeability and retention effect (EPR).[93] Through EPR, the size of nanoparticles may allow their passage through characteristically leaky vasculature around tumor sites,[94] where pores between endothelial cells may allow the extravasation of nanoparticles introduced systemically. Localization may be significantly enhanced by incorporation of targeting moieties on the surface of the carrier (e.g. peptides, aptamers, antibodies/antibody fragments, small molecules). Malignant cells may specifically recognize these ligands and imbibe the nanoparticle by receptor mediated endocytosis. This section describes these targeting strategies, and methods to enhance localization and decreased accumulation in healthy tissues.

As cancerous cells replicate at a high rate, vascular tissue must also form rapidly to provide nutrients for the cancerous region. This process is known as angiogenesis, and is important for the development of tumor mass. Before neovascularization, endothelial cells are barely dividing since only about 1 in 10,000 cells undergo cellular division at any given time.[95] As angiogenesis occurs, the rate of endothelial cell division increases enormously (about 50-fold).[96] During this process, endothelial cell growth will require the reorganization of the extracellular matrix, where cell growth will migrate toward the source of angiostimulatory molecules (i.e. tumor cells). For healthy cells, the growth of vasculature is self-limited through the production and release of angioinhibitory molecules. The regulated growth of healthy tissue results in a well-constructed tubular network of endothelium with very small pores between cells (~2 nm).[97] However, this equilibrium between stimulatory and inhibitory molecules may be disrupted for tumors. The accelerated rate of growth of vasculature at tumors facilitates carcinogenesis, but also results in tissues that are physically very different from healthy cells.

Tumor vasculature is characteristically highly permeable or “leaky”, [98] with pores ranging in size from 200 nm to 1.2 μm.[99] In addition, lymphatic drainage from the interstitial tissues within the tumor is commonly hindered.[100] This leaky nature of cancer

was observed by Maeda et al. in the late 1980's, where biocompatible macromolecules had a tendency to accumulate at higher concentrations at tumor sites than healthy tissues.[93, 101] In their mechanistic explanation of the phenomenon, Maeda coined the term enhanced permeability and retention.[48, 93, 100, 102] As a result, polymer drug carriers were designed to exploit EPR to selectively deposit at cancer sites. For example, particles of appropriate size and biocompatibility may circulate for extensive periods of time and deposit through leaky pores in neovasculature. As shown in **Figure 1.4,** accumulation is additionally promoted by poor lymphatic drainage from the region of tumor cells.

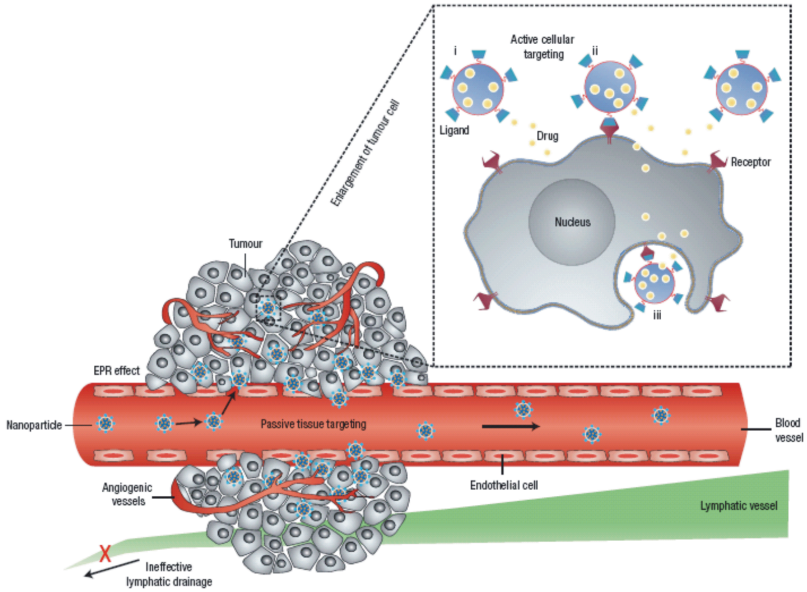

Figure 1.4 Schematic illustration of combined passive targeting (via EPR) and active targeting within tumor tissues. Adapted from Ref 98.

The result of the EPR effect is a possible outlet for passively targeting nanoparticle drug carriers to tumor sites. Through this targeting, the overall systemic dose needed for many therapeutics may be lowered. However, improved therapeutic efficacy and reduced toxicity may be achieved by targeting specific cell surface interactions. This is typically done through the surface conjugation of targeting ligands.

In addition to the vasculature environment, the surface of cancer cells is often unique and can be exploited by drug delivery vehicles for more effective targeting. Solid

tumors characteristically overexpress specific antigens or receptors on their surface, including epidermal growth factor (EGF),[103] TRAIL receptor,[104] folate receptor,[105] and others.[106-107] By functionalizing the surface of nanoparticles with targeting molecules such as antibodies, peptides, or aptamers, the receptor mediated uptake pathways of cancer cells may be exploited.[108-112]

Folate Targeting

Folic acid (or vitamin B9) plays an important role in the biosynthesis of nucleotide bases and is consumed rapidly during cellular proliferation. In general there are two mechanisms by which cells obtain folate, either through the folate carrier or by action of the folate receptor. While the folate carrier is present in virtually all cells and is the primary pathway for folate uptake, the folate receptor is typically on polarized epithelial cells and activated macrophages.[113] This receptor is responsible for preferentially binding and internalizing oxidized folates by receptor mediated endocytosis. Cancer cells frequently overexpress this receptor, which may enable diseased cells to compete for folate when scarce.[114] Folate is an attractive targeting molecule for several reasons, including its specificity to cancer cells, high binding affinity ($K_D \sim 10^{-10}$ M), small size, stability in storage, low cost, and availability.[113, 115]

There are several examples of the targeting of macromolecules and nanoparticles utilizing folate bioconjugation.[113, 116,117] For example, by decorating the surface of temperature-responsive pNIPAm-based nanogels with folate, uptake was readily observed *in vitro* in the presence cancer cells that overexpress the folate receptor.[117] In this case, the targeting molecule was covalently tethered to the amines of the shell of a core/shell nanogel construct. Furthermore, these particles exhibited thermal cytotoxicity when at elevated temperatures (above their volume phase transition temperature).[117] Another example includes the folate-nanogels recently developed by Vinogradov et al., which also demonstrated the efficiency of folate targeting in vitro.[118] Transcellular

transport of their folate-conjugated drug carrier was found to be four times more effective than using the drug alone in their cellular model system.

Galactose Targeting

Like folate, galactose-based targeting of nanoparticles may be a promising route for active cell targeting, specifically for malignant tissues localized in the liver.[119-120] This sugar has a specific binding affinity to asialoglycoprotein receptors in the HepG2 human hepatoblastoma cell line. By conjugating galactose to the surface of pNIPAm-co-AA nanogels, Choi et al. showed a drastic increase in uptake by receptor-mediated endocytosis into blastoma cells.[121] Due to particle temperature responsivity, this group also investigated the temperature-dependent uptake of their nanoparticles. The uptake efficiency was found to increase at elevated temperatures, which may be a result of particle deswelling of above the volume phase transition temperature of the polymer.[121]

Transferrin Targeting

Through conjugation of nanogels (nano-PEG-cross-PEI) bioconjugated with insulin and transferrin molecules, Vinagradov et al. demonstrated the efficient delivery of oligonucleotides across a model blood brain barrier (BBB).[122] Through incorporation of poly(ethylene glycol), circulation times of nanogels was increased, resulting in an increased exposure to the BBB. Although the BBB is impermeable to macromolecules, it has been suggested that nanoparticles at this size scale may participate in receptor-mediated transcytosis in BBB without violating the integrity of the tight junctions of the brain microvascular endothelial cells.[122]

Peptide targeting

Small peptides (6-20 amino acids) are powerful targeting molecules when conjugated to nanoparticle drug carriers. Their ease of synthesis, well-defined and efficient chemical reactions for linkage to nanoparticle surfaces, and decreased likelihood

of generating a harmful immune response make them an attractive alternative to some other targeting moieties.[112, 123-125] Certain peptides may mimic surface receptor ligands, allowing for direct targeting of nanoparticles to cells expressing the receptor target. This bioconjugation could promote the receptor-ligand mediated endocytosis of nanoparticles and enable a pathway for uptake by target cells.

There are several examples of efficient targeting through peptide bioconjugation. Recently, Wolf et al. demonstrated the delivery of small interfering RNA molecules (siRNA) to tumor bearing mice through the bioconjugation of RGD (Arg-Gly-Asp) to PEG-PEI nanoparticles.[126] In another example, Becker et al. bioconjugated the protein transduction domain (PTD) from the HIV-1 Tat protein to their polymer micelle drug delivery vehicles.[127-128] The bioconjugation employed in both examples increased the efficiency of cell penetration for the nanoparticles.

1.5 Outlook

This chapter reviewed some of the chemical features that influence the efficacy and the biocompatibility of nanomaterials for intravenous injection. The list of features needed in a single vehicle is exhaustive, whereas optimizing all of those factors together is a monumental task. At the onset of this dissertation work, nanogels were recognized as a promising opportunity to meet this challenge. Using the synthetic tools developed by Lyon and coworkers, nanoparticles may be synthesized with unique hydrogel compartments, each with designed chemical features for intravenous drug delivery (e.g. for improved targeting, stealth, toxicity, biodistribution, erosion/clearance, and controlled release). Thus, nanogels were investigated in this disseration as a “tunable” platform for generating multifunctional delivery vehicles.

1.6 References

1. Langer, R.; Peppas, N. A., Advances in biomaterials, drug delivery, and bionanotechnology. *AIChE J.* **2003,** *49* (12), 2990-3006.

2. Ratner, B. D.; Bryant, S. J., Biomaterials: Where we have been and where we are going. *Annu. Rev. Biomed. Eng.* **2004,** *6*, 41-75.

3. Anderson, J. M., Biological responses to materials. *Annu. Rev. Mater. Res.* **2001,** *31*, 81-110.

4. Langer, R., Biomaterials in drug delivery and tissue engineering: One laboratory's experience. *Acc. Chem. Res.* **2000,** *33* (2), 94-101.

5. Langer, R., Drug delivery and targeting. *Nature* **1998,** *392* (6679), 5-10.

6. Brem, H.; Piantadosi, S.; Burger, P. C.; Walker, M.; Selker, R.; Vick, N. A.; Black, K.; Sisti, M.; Brem, S.; Mohr, G.; Muller, P.; Morawetz, R.; Schold, S. C., Placebo-Controlled Trial of Safety and Efficacy of Intraoperative Controlled Delivery by Biodegradable Polymers of Chemotherapy for Recurrent Gliomas. *Lancet* **1995,** *345* (8956), 1008-1012.

7. Sullivan, S. P.; Koutsonanos, D. G.; Martin, M. D.; Lee, J. W.; Zarnitsyn, V.; Choi, S. O.; Murthy, N.; Compans, R. W.; Skountzou, I.; Prausnitz, M. R., Dissolving polymer microneedle patches for influenza vaccination. *Nat. Med.* **2010,** *16* (8), 915-U116.

8. Allen, T. M., Long-circulating (sterically stabilized) liposomes for targeted drug-delivery. *Trends Pharmacol. Sci.* **1994,** *15* (7), 215-220.

9. Eavarone, D. A.; Yu, X. J.; Bellamkonda, R. V., Targeted drug delivery to C6 glioma by transferrin-coupled liposomes. *J. Biomed. Mater. Res.* **2000,** *51* (1), 10-14.

10. Storm, G.; Belliot, S. O.; Daemen, T.; Lasic, D. D., Surface Modification of Nanoparticles to Oppose Uptake by the Mononuclear Phagocyte System. *Adv. Drug Delivery Rev.* **1995,** *17* (1), 31-48.

11. Zhou, R.; Mazurchuk, R.; Straubinger, R. M., Antivasculature effects of doxorubicin-containing liposomes in an intracranial rat brain tumor model. *Cancer Res.* **2002,** *62* (9), 2561-2566.

12. Balogh, L.; Nigavekar, S. S.; Nair, B. M.; Lesniak, W.; Zhang, C.; Sung, L. Y.; Kariapper, M. S. T.; El-Jawahri, A.; Llanes, M.; Bolton, B.; Mamou, F.; Tan, W.; Hutson, A.; Minc, L.; Khan, M. K., Significant effect of size on the in vivo biodistribution of gold composite nanodevices in mouse tumor models. *Nanomedicine-Nanotechnology Biology and Medicine* **2007,** *3* (4), 281-296.

13. Choi, H. S.; Liu, W.; Misra, P.; Tanaka, E.; Zimmer, J. P.; Ipe, B. I.; Bawendi, M. G.; Frangioni, J. V., Renal clearance of quantum dots. *Nat. Biotechnol.* **2007,** *25* (10), 1165-1170.

14. Kairdolf, B. A.; Mancini, M. C.; Smith, A. M.; Nie, S. M., Minimizing nonspecific cellular binding of quantum dots with hydroxyl-derivatizied surface coatings. *Anal. Chem.* **2008,** *80* (8), 3029-3034.

15. Liu, W.; Howarth, M.; Greytak, A. B.; Zheng, Y.; Nocera, D. G.; Ting, A. Y.; Bawendi, M. G., Compact biocompatible quantum dots functionalized for cellular imaging. *J. Am. Chem. Soc.* **2008,** *130* (4), 1274-1284.

16. Oyelere, A. K.; Chen, P. C.; Huang, X. H.; El-Sayed, I. H.; El-Sayed, M. A., Peptide-conjugated gold nanorods for nuclear targeting. *Bioconjug. Chem.* **2007,** *18* (5), 1490-1497.

17. Tkachenko, A. G.; Xie, H.; Coleman, D.; Glomm, W.; Ryan, J.; Anderson, M. F.; Franzen, S.; Feldheim, D. L., Multifunctional gold nanoparticle-peptide complexes for nuclear targeting. *J. Am. Chem. Soc.* **2003,** *125* (16), 4700-4701.

18. Tkachenko, A. G.; Xie, H.; Liu, Y. L.; Coleman, D.; Ryan, J.; Glomm, W. R.; Shipton, M. K.; Franzen, S.; Feldheim, D. L., Cellular trajectories of peptide-modified gold particle complexes: Comparison of nuclear localization signals and peptide transduction domains. *Bioconjug. Chem.* **2004,** *15* (3), 482-490.

19. Thurmond, K. B.; Huang, H. Y.; Clark, C. G.; Kowalewski, T.; Wooley, K. L., Shell cross-linked polymer micelles: stabilized assemblies with great versatility and potential. *Colloids and Surfaces B-Biointerfaces* **1999,** *16* (1-4), 45-54.

20. van Nostrum, C. F., Polymeric micelles to deliver photosensitizers for photodynamic therapy. *Adv. Drug Delivery Rev.* **2004,** *56* (1), 9-16.

21. Cheng, J.; Teply, B. A.; Sherifi, I.; Sung, J.; Luther, G.; Gu, F. X.; Levy-Nissenbaum, E.; Radovic-Moreno, A. F.; Langer, R.; Farokhzad, O. C., Formulation of functionalized PLGA-PEG nanoparticles for in vivo targeted drug delivery. *Biomaterials* **2007,** *28* (5), 869-876.

22. Cho, Y. W.; Park, S. A.; Han, T. H.; Son, D. H.; Park, J. S.; Oh, S. J.; Moon, D. H.; Cho, K. J.; Ahn, C. H.; Byun, Y.; Kim, I. S.; Kwon, I. C.; Kim, S. Y., In vivo tumor targeting and radionuclide imaging with self-assembled nanoparticles: Mechanisms, key factors, and their implications. *Biomaterials* **2007,** *28* (6), 1236-1247.

23. Das, M.; Mardyani, S.; Chan, W. C. W.; Kumacheva, E., Biofunctionalized pH-responsive microgels for cancer cell targeting: Rational design. *Adv. Mater.* **2006,** *18* (1), 80-83.

24. Fukukawa, K. I.; Rossin, R.; Hagooly, A.; Pressly, E. D.; Hunt, J. N.; Messmore, B. W.; Wooley, K. L.; Welch, M. J.; Hawker, C. J., Synthesis and characterization of core-shell star copolymers for in vivo PET imaging applications. *Biomacromolecules* **2008,** *9* (4), 1329-1339.

25. Owens, D. E.; Peppas, N. A., Opsonization, biodistribution, and pharmacokinetics of polymeric nanoparticles. *Int. J. Pharm.* **2006,** *307* (1), 93-102.

26. Sergeyev, V. G.; Novoskoltseva, O. A.; Pyshkina, O. A.; Zinchenko, A. A.; Rogacheva, V. B.; Zezin, A. B.; Yoshikawa, K.; Kabanov, V. A., Secondary structure of DNA is recognized by slightly cross-linked cationic hydrogel. *J. Am. Chem. Soc.* **2002,** *124* (38), 11324-11333.

27. Vinogradov, S. V., Colloidal Microgels in Drug Delivery Applications. *Curr. Pharm. Des.* **2006,** *12* (36), 4703-4712.

28. Alexis, F.; Pridgen, E.; Molnar, L. K.; Farokhzad, O. C., Factors affecting the clearance and biodistribution of polymeric nanoparticles. *Mol. Pharm.* **2008,** *5* (4), 505-515.

29. Stolnik, S.; Illum, L.; Davis, S. S., Long Circulating Microparticulate Drug Carriers. *Adv. Drug Delivery Rev.* **1995,** *16* (2-3), 195-214.

30. Prokop, A.; Davidson, J. M., Nanovehicular intracellular delivery systems. *J. Pharm. Sci.* **2008,** *97* (9), 3518-3590.

31. Peppas, N. A.; Hilt, J. Z.; Khademhosseini, A.; Langer, R., Hydrogels in biology and medicine: From molecular principles to bionanotechnology. *Adv. Mater.* **2006,** *18* (11), 1345-1360.

32. Ulijn, R. V.; Bibi, N.; Jayawarna, V.; Thornton, P. D.; Todd, S. J.; Mart, R. J.; Smith, A. M.; Gough, J. E., Bioresponsive hydrogels. *Materials Today* **2007,** *10* (4), 40-48.

33. Hoare, T.; Pelton, R., Highly pH and temperature responsive microgels functionalized with vinylacetic acid. *Macromolecules* **2004,** *37* (7), 2544-2550.

34. Sershen, S. R.; Westcott, S. L.; Halas, N. J.; West, J. L., Temperature-sensitive polymer-nanoshell composites for photothermally modulated drug delivery. *J. Biomed. Mater. Res.* **2000,** *51* (3), 293-298.

35. Suzuki, A.; Tanaka, T., Phase-transition in polymer gels induced by visible-light. *Nature* **1990,** *346* (6282), 345-347.

36. Duracher, D.; Sauzedde, F.; Elaissari, A.; Pichot, C.; Nabzar, L., Cationic amino-containing N-isopropyl-acrylamide-styrene copolymer particles: 2-surface and colloidal characteristics. *Colloid Polym. Sci.* **1998,** *276* (10), 920-929.

37. Hendrickson, G. R.; Lyon, L. A., Bioresponsive hydrogels for sensing applications. *Soft Matter* **2009,** *5* (1), 29-35.

38. Miyata, T.; Asami, N.; Uragami, T., A reversibly antigen-responsive hydrogel. *Nature* **1999,** *399* (6738), 766-769.

39. Hoare, T.; Pelton, R., Charge-switching, amphoteric glucose-responsive microgels with physiological swelling activity. *Biomacromolecules* **2008,** *9* (2), 733-740.

40. Starovoytova, L.; Spevacek, J.; Ilavsky, M., H-1 NMR study of temperature-induced phase transitions in D2O solutions of poly(N-isopropylmethacrylamide)/poly(N-isopropylacrylamide) mixtures and random copolymers. *Polymer* **2005,** *46* (3), 677-683.

41. Heskins, M.; Guillet, J. E., Solution properties of poly(N-isopropylacrylamide). *J. Macromol. Sci. Chem.* **1968,** *A2*, 1441-1455.

42. Kubota, K.; Fujishige, S.; Ando, I., Single-chain transition of poly(n-isopropylacrylamide) in water. *J. Phys. Chem.* **1990,** *94* (12), 5154-5158.

43. Dusek, K.; Patterson, K., Transition on swollen polymer networks induced by intramolecular condensation. *J. Poly. Sci., Poly. Phys. Ed.* **1968,** *6* (7), 1209-16.

44. Pelton, R., Temperature-sensitive aqueous microgels. *Adv. Colloid Interface Sci.* **2000,** *85* (1), 1-33.

45. Jones, C. D.; Lyon, L. A., Synthesis and Characterization of Multiresponsive Core−Shell Microgels. *Macromolecules* **2000,** *33* (22), 8301-8306.

46. Schild, H. G., Poly(N-isopropylacrylamide): experiment, theory and application. *Prog. Polym. Sci.* **1992,** *17* (2), 163-249.

47. Nayak, S.; Lyon, L. A., Soft nanotechnology with soft nanoparticles. *Angew. Chem., Int. Ed.* **2005,** *44* (47), 7686-7708.

48. Maeda, H.; Wu, J.; Sawa, T.; Matsumura, Y.; Hori, K., Tumor vascular permeability and the EPR effect in macromolecular therapeutics: a review. *J. Control. Release* **2000**, 271-284.

49. Meng, Z. Y.; Smith, M. H.; Lyon, L. A., Temperature-programmed synthesis of micron-sized multi-responsive microgels. *Colloid Polym. Sci.* **2009,** *287* (3), 277-285.

50. Zha, L. S.; Zhang, Y.; Yang, W. L.; Fu, S. K., Monodisperse Temperature-Sensitive Microcontainers. *Adv. Mater.* **2002,** *14* (15), 1090-1092.

51. Singh, N.; Lyon, L. A., Au Nanoparticle Templated Synthesis of pNIPAm Nanogels. *Chem. Mater.* **2007,** *19* (4), 719-726.

52. Zhou, G.; Elaissari, A.; Delair, T.; Pichot, C., Synthesis and characterization of surface-cyanofunctionalized poly(N-isopropylacrylamide) latexes. *Colloid Polym. Sci.* **1998,** *276* (12), 1131-1139.

53. Matsuoka, H.; Fujimoto, K.; Kawaguchi, H., Stimuli-response of microsphere having poly(N-isopropylacrylamide) shell. *Polym. J. (Tokyo, Jpn.)* **1999,** *31* (11), 1139-1144.

54. Senff, H.; Richtering, W.; Norhausen, C.; Weiss, A.; Ballauff, M., Rheology of a Temperature Sensitive Coreâ^'Shell Latex. *Langmuir* **1998,** *15* (1), 102-106.

55. Pascale, H.; Christian, P.; Abderrahim, M., Synthesis of hairy acrylic core-shell particles as toughening agents for epoxy networks. *Macromol. Chem. Phys.* **2000,** *201* (6), 632-641.

56. Hu, X.; Tong, Z.; Lyon, L. A., Multicompartment Core/Shell Microgels. *J. Am. Chem. Soc.* **2010,** *132* (33), 11470-11472.

57. Smith, M. H.; Herman, E. S.; Lyon, L. A., Network Deconstruction Reveals Network Structure in Responsive Microgels. *J. Phys. Chem. B* **2011,** *115* (14), 3761-3764.

58. Smith, M. H.; South, A. B.; Gaulding, J. C.; Lyon, L. A., Monitoring the Erosion of Hydrolytically-Degradable Nanogels via Multiangle Light Scattering Coupled to Asymmetrical Flow Field-Flow Fractionation. *Anal. Chem.* **2009,** *82* (2), 523-530.

59. South, A. B.; Lyon, L. A., Direct Observation of Microgel Erosion via in-Liquid Atomic Force Microscopy. *Chem. Mater.* **2010,** *22* (10), 3300-3306.

60. Nayak, S.; Gan, D.; Serpe, M.; Lyon, L., Hollow Thermoresponsive Microgels. *Small* **2005,** *1* (4), 416-421.

61. Smith, M. H.; Lyon, L. A., Multifunctional Nanogels for siRNA Delivery. *Acc. Chem. Res.* **2011**.

62. Gan, D.; Lyon, L. A., Fluorescence nonradiative energy transfer analysis of crosslinker heterogeneity in core-shell hydrogel nanoparticles. *Anal. Chim. Acta* **2003,** *496* (1-2), 53-63.

63. Jones, C. D.; Lyon, L. A., Synthesis and Characterization of Multiresponsive Core-Shell Microgels. *Macromolecules* **2000,** *33* (22), 8301-8306.

64. Fernandez-Nieves, A.; Fernandez-Barbero, A.; Vincent, B.; de las Nieves, F. J., Charge Controlled Swelling of Microgel Particles. *Macromolecules* **2000,** *33* (6), 2114-2118.

65. Ito, S.; Ogawa, K.; Suzuki, H.; Wang, B.; Yoshida, R.; Kokufuta, E., Preparation of Thermosensitive Submicrometer Gel Particles with Anionic and Cationic Chargesâ€ *Langmuir* **1999,** *15* (12), 4289-4294.

66. Wu, C.; Zhou, S., Volume Phase Transition of Swollen Gels: Discontinuous or Continuous? *Macromolecules* **1997,** *30* (3), 574-576.

67. Chi, W., A comparison between the coil-to-globule transition of linear chains and the "volume phase transition" of spherical microgels. *Polymer* **1998,** *39* (19), 4609-4619.

68. Berndt, I.; Pedersen, J. S.; Richtering, W., Temperature-Sensitive Core-Shell Microgel Particles with Dense Shell13. *Angew. Chem., Int. Ed.* **2006,** *45* (11), 1737-1741.

69. Saunders, B. R., On the structure of poly(N-isopropylacrylamide) microgel particles. *Langmuir* **2004,** *20* (10), 3925-3932.

70. Saunders, B. R.; Vincent, B., Microgel particles as model colloids: theory, properties and applications. *Adv. Colloid Interface Sci.* **1999,** *80* (1), 1-25.

71. Gan, D.; Lyon, L. A., Interfacial Nonradiative Energy Transfer in Responsive Core-Shell Hydrogel Nanoparticles. *J. Am. Chem. Soc.* **2001,** *123* (34), 8203-8209.

72. Varga, I.; Gilanyi, T.; Meszaros, R.; Filipcsei, G.; Zrinyi, M., Effect of Cross-Link Density on the Internal Structure of Poly(N-isopropylacrylamide) Microgels. *J. Phys. Chem. B* **2001,** *105* (38), 9071-9076.

73. Jones, C. D.; Lyon, L. A., Shell-Restricted Swelling and Core Compression in Poly(N-isopropylacrylamide) Core-Shell Microgels. *Macromolecules* **2003,** *36* (6), 1988-1993.

74. Jones, C. D.; Lyon, L. A., Dependence of Shell Thickness on Core Compression in Acrylic Acid Modified Poly(N-isopropylacrylamide) Core/Shell Microgels. *Langmuir* **2003,** *19* (11), 4544-4547.

75. Wichterle, O.; Lim, D., Hydrophilic Gels For Biological Use. *Nature* **1960,** *185* (4706), 117-118.

76. Hawley, A. E.; Davis, S. S.; Illum, L., Targeting Of Colloids To Lymph-Nodes - Influence Of Lymphatic Physiology And Colloidal Characteristics. *Adv. Drug Delivery Rev.* **1995,** *17* (1), 129-148.

77. Schiffelers, R. M.; Bakker-Woudenberg, I.; Snijders, S. V.; Storm, G., Localization of sterically stabilized liposomes in Klebsiella pneumoniae-infected rat lung tissue: influence of liposome characteristics. *Biochim. Biophys. Acta, Biomembr.* **1999,** *1421* (2), 329-339.

78. Ishida, O.; Maruyama, K.; Sasaki, K.; Iwatsuru, M., Size-dependent extravasation and interstitial localization of polyethyleneglycol liposomes in solid tumor-bearing mice. *Int. J. Pharm.* **1999,** *190* (1), 49-56.

79. Kong, G.; Braun, R. D.; Dewhirst, M. W., Hyperthermia enables tumor-specific nanoparticle delivery: Effect of particle size. *Cancer Res.* **2000,** *60* (16), 4440-4445.

80. Alexis, F.; Pridgen, E.; Molnar, L. K.; Farokhzad, O. C., Factors affecting the clearance and biodistribution of polymeric nanoparticles. *Molecular Pharmaceutics* **2008**, 505-515.

81. Gref, R.; Minamitake, Y.; Peracchia, M. T.; Trubetskoy, V.; Torchilin, V.; Langer, R., Biodegradable Long-Circulating Polymeric Nanospheres. *Science* **1994,** *263* (5153), 1600-1603.

82. Ward, P. A., Recruitment of inflammatory cells into lung: Roles of cytokines, adhesion molecules, and complement. *J. Lab. Clin. Med.* **1997**, 400-404.

83. Kao, W. Y. J., Evaluation of protein-modulated macrophage behavior on biomaterials: designing biomimetic materials for cellular engineering. *Biomaterials* **1999,** *20* (23-24), 2213-2221.

84. Moghimi, S. M.; Hedeman, H.; Muir, I. S.; Illum, L.; Davis, S. S., An Investigation Of The Filtration Capacity And The Fate Of Large Filtered Sterically-Stabilized Microspheres In Rat Spleen. *Biochim. Biophys. Acta* **1993,** *1157* (3), 233-240.

85. Ogawara, K.; Yoshida, M.; Furumoto, K.; Takakura, Y.; Hashida, M.; Higaki, K.; Kimura, T., Uptake by hepatocytes and biliary excretion of intravenously administered polystyrene microspheres in rats. *J. Drug Target.* **1999,** *7* (3), 213-221.

86. Muller, R. H.; Wallis, K. H.; Troster, S. D.; Kreuter, J., In Vitro Characterization Of Poly(Methyl-Methacrylate) Nanoparticles And Correlation To Their In Vivo Fate. *J. Control. Release* **1992,** *20* (3), 237-246.

87. Lynch, I.; Dawson, K. A., Protein-nanoparticle interactions. *Nano Today* **2008,** *3* (1-2), 40-47.

88. Tabata, Y.; Ikada, Y., Effect Of The Size And Surface-Charge Of Polymer Microspheres On Their Phagocytosis By Macrophage. *Biomaterials* **1988,** *9* (4), 356-362.

89. Gref, R.; Domb, A.; Quellec, P.; Blunk, T.; Muller, R. H.; Verbavatz, J. M.; Langer, R., The Controlled Intravenous Delivery Of Drugs Using PEG-Coated Sterically Stabilized Nanospheres. *Adv. Drug Delivery Rev.* **1995,** *16* (2-3), 215-233.

90. Otsuka, H.; Nagasaki, Y.; Kataoka, K., PEGylated nanoparticles for biological and pharmaceutical applications. *Adv. Drug Delivery Rev.* **2003,** *55* (3), 403-419.

91. Jeon, S. I.; Lee, J. H.; Andrade, J. D.; Degennes, P. G., Protein Surface Interactions In The Presence Of Polyethylene Oxide. 1. Simplified Theory. *J. Colloid Interface Sci.* **1991,** *142* (1), 149-158.

92. Jeon, S. I.; Andrade, J. D., Protein Surface Interactions In The Presence Of Polyethylene Oxide. 2. Effect Of Protein Size. *J. Colloid Interface Sci.* **1991,** *142* (1), 159-166.

93. Matsumura, Y.; Maeda, H., A New Concept For Macromolecular Therapeutics In Cancer-Chemotherapy - Mechanisms Of Tumoritropic Accumulation Of Proteins And The Antitumor Agent Smancs. *Cancer Res.* **1986,** *46* (12), 6387-6392.

94. Monsky, W. L.; Fukumura, D.; Gohongi, T.; Ancukiewcz, M.; Weich, H. A.; Torchilin, V. P.; Yuan, F.; Jain, R. K., Augmentation of transvascular transport of macromolecules and nanoparticles in tumors using vascular endothelial growth factor. *Cancer Res.* **1999,** *59* (16), 4129-4135.

95. Hobson, B.; Denekamp, J., Endothelial Proliferation In Tumors And Normal-Tissues - Continuous Labeling Studies. *Br. J. Cancer* **1984,** *49* (4), 405-413.

96. Fox, S. B.; Gatter, K. C.; Bicknell, R.; Going, J. J.; Stanton, P.; Cooke, T. G.; Harris, A. L., Relationship Of Endothelial-Cell Proliferation To Tumor Vascularity In Human Breast-Cancer. *Cancer Res.* **1993,** *53* (18), 4161-4163.

97. Maeda, H., The enhanced permeability and retention (EPR) effect in tumor vasculature: The key role of tumor-selective macromolecular drug targeting. *Adv. Enzyme Regul.* **2001**, 189-207.

98. Peer, D.; Karp, J. M.; Hong, S.; Farokhzad, O. C.; Margalit, R.; Langer, R., Nanocarriers as an emerging platform for cancer therapy. *Nat. Nanotechnol.* **2007,** *2* (12), 751-760.

99. Hobbs, S. K.; Monsky, W. L.; Yuan, F.; Roberts, W. G.; Griffith, L.; Torchilin, V. P.; Jain, R. K., Regulation of transport pathways in tumor vessels: Role of tumor type and microenvironment. *Proc. Natl. Acad. Sci. U. S. A.* **1998,** *95* (8), 4607-4612.

100. Maeda, H., The enhanced permeability and retention (EPR) effect in tumor vasculature: The key role of tumor-selective macromolecular drug targeting. *J. Control. Release* **2001**, 189-207.

101. Maeda, H.; Matsumura, Y., Tumoritropic And Lymphotropic Principles Of Macromolecular Drugs. *Crit. Rev. Ther. Drug Carrier Syst.* **1989,** *6* (3), 193-210.

102. Maeda, H.; Seymour, L. W.; Miyamoto, Y., Conjugates Of Anticancer Agents And Polymers - Advantages Of Macromolecular Therapeutics In Vivo. *Bioconjug. Chem.* **1992,** *3* (5), 351-362.

103. Chaidarun, S. S.; Eggo, M. C.; Sheppard, M. C.; Stewart, P. M., Expression of Epidermal Growth-Factor (EGF), Its Receptor, And Related Oncoprotein (ERBB-2) In Human Pituitary-Tumors And Response to EGF In-Vitro *Endocrinology* **1994,** *135* (5), 2012-2021.

104. Daniels, R. A.; Turley, H.; Kimberley, F. C.; Liu, X. S.; Mongkolsapaya, J.; Ch'en, P.; Xu, X. N.; Jin, B. Q.; Pezzella, F.; Screaton, G. R., Expression of TRAIL and TRAIL receptors in normal and malignant tissues. *Cell Res.* **2005,** *15* (6), 430-438.

105. Parker, N.; Turk, M. J.; Westrick, E.; Lewis, J. D.; Low, P. S.; Leamon, C. P., Folate receptor expression in carcinomas and normal tissues determined by a quantitative radioligand binding assay. *Anal. Biochem.* **2005,** *338* (2), 284-293.

106. Scholler, N.; Fu, N.; Yang, Y.; Ye, Z. M.; Goodman, G. E.; Hellstrom, K. E.; Hellstrom, I., Soluble member(s) of the mesothelin/megakaryocyte potentiating factor family are detectable in sera from patients with ovarian carcinoma. *Proc. Natl. Acad. Sci. U. S. A.* **1999,** *96* (20), 11531-11536.

107. Bezwoda, W. R., c-erb-B-2 expression and response to treatment in metastatic breast cancer. *Med. Oncol.* **2000,** *17* (1), 22-28.

108. Ryan, J. A.; Overton, K. W.; Speight, M. E.; Oldenburg, C. M.; Loo, L.; Robarge, W.; Franzen, S.; Feldheim, D. L., Cellular uptake of gold nanoparticles passivated with BSA-SV40 large T antigen conjugates. *Anal. Chem.* **2007,** *79*, 9150-9159.

109. Vasir, J. K.; Labhasetwar, V., Targeted drug delivery in cancer therapy. *Technol. Cancer Res. Treat.* **2005,** *4* (4), 363-374.

110. Lee, R. J.; Low, P. S., Delivery of liposomes into cultured KB cells via folate receptor-mediated endocytosis. *J. Biol. Chem.* **1994,** *269* (5), 3198-204.

111. Farokhzad, O. C.; Cheng, J.; Teply, B. A.; Sherifi, I.; Jon, S.; Kantoff, P. W.; Richie, J. P.; Langer, R., Targeted nanoparticle-aptamer bioconjugates for cancer chemotherapy in vivo. *Proc. Natl. Acad. Sci. U. S. A.* **2006,** *103* (16), 6315-6320.

112. Saad, M.; Garbuzenko, O. B.; Ber, E.; Chandna, P.; Khandare, J. J.; Pozharov, V. P.; Minko, T., Receptor targeted polymers, dendrimers, liposomes: Which nanocarrier is the most efficient for tumor-specific treatment and imaging? *J. Control. Release* **2008,** *130* (2), 107-114.

113. Lu, Y. J.; Low, P. S., Folate-mediated delivery of macromolecular anticancer therapeutic agents. *Adv. Drug Delivery Rev.* **2002,** *54* (5), 675-693.

114. Toffoli, G.; Cernigoi, C.; Russo, A.; Gallo, A.; Bagnoli, M.; Boiocchi, M., Overexpression of folate binding protein in ovarian cancers. *Int. J. Cancer* **1997,** *74* (2), 193-198.

115. Reddy, J. A.; Low, P. S., Folate-mediated targeting of therapeutic and imaging agents to cancers. *Crit. Rev. Ther. Drug Carrier Syst.* **1998,** *15* (6), 587-627.

116. Kukowska-Latallo, J. F.; Candido, K. A.; Cao, Z. Y.; Nigavekar, S. S.; Majoros, I. J.; Thomas, T. P.; Balogh, L. P.; Khan, M. K.; Baker, J. R., Nanoparticle targeting of anticancer drug improves therapeutic response in animal model of human epithelial cancer. *Cancer Res.* **2005,** *65* (12), 5317-5324.

117. Nayak, S.; Lee, H.; Chmielewski, J.; Lyon, L. A., Folate-mediated cell targeting and cytotoxicity using thermoresponsive microgels. *J. Am. Chem. Soc.* **2004,** *126* (33), 10258-10259.

118. Vinogradov, S. V.; Zeman, A. D.; Batrakova, E. V.; Kabanov, A. V., Polyplex Nanogel formulations for drug delivery of cytotoxic nucleoside analogs. *J. Control. Release* **2005,** *107* (1), 143-157.

119. Aarnoudse, C. A.; Vallejo, J. J. G.; Saeland, E.; van Kooyk, Y., Recognition of tumor glycans by antigen-presenting cells. *Curr. Opin. Immunol.* **2006,** *18* (1), 105-111.

120. Wu, J.; Nantz, M. H.; Zern, M. A., Targeting hepatocytes for drug and gene delivery: Emerging novel approaches and applications. *Front. Biosci.* **2002,** *7*, D717-D725.

121. Choi, S. H.; Yoon, J. J.; Park, T. G., Galactosylated poly(N-isopropylacrylamide) hydrogel submicrometer particles for specific cellular uptake within hepatocytes. *J. Colloid Interface Sci.* **2002,** *251* (1), 57-63.

122. Vinogradov, S. V.; Batrakova, E. V.; Kabanov, A. V., Nanogels for oligonucleotide delivery to the brain. *Bioconjug. Chem.* **2004,** *15* (1), 50-60.

123. Mok, H.; Park, T. G., Self-crosslinked and reducible fusogenic peptides for intracellular delivery of siRNA. *Biopolymers* **2008,** *89* (10), 881-8.

124. Kim, S.; Jeong, J. H.; Lee, S. H.; Kim, S.; Park, T. G., LHRH Receptor-Mediated Delivery of siRNA Using Polyelectrolyte Complex Micelles Self-Assembled from siRNA-PEG-LHRH Conjugate and PEI. *Bioconjug. Chem.* **2008,** *19*, 2156-2162.

125. Jeong, J. H.; Mok, H.; Oh, Y. K.; Park, T. G., siRNA Conjugate Delivery Systems. *Bioconjug. Chem.* **2008,** *DOI 10.1021/bc800278e*, published online 2008/12/05.

126. de Wolf, H. K.; Snel, C. J.; Verbaan, F. J.; Schiffelers, R. M.; Hennink, W. E.; Storm, G., Effect of cationic carriers on the pharmacokinetics and tumor localization of nucleic acids after intravenous administration. *Int. J. Pharm.* **2007**, 167-175.

127. Becker, M. L.; Remsen, E. E.; Pan, D.; Wooley, K. L., Peptide-derivatized shell-cross-linked nanoparticles. 1. Synthesis and characterization. *Bioconjug. Chem.* **2004,** *15* (4), 699-709.

128. Becker, M. L.; Bailey, L. O.; Wooley, K. L., Peptide-Derivatized Shell-Cross-Linked Nanoparticles. 2. Biocompatibility Evaluation. *Bioconjug. Chem.* **2004,** *15* (4), 710-717.

CHAPTER 2

LIGHT SCATTERING AND COMPLEMENTARY TECHNIQUES

2.1 Introduction to Analytical Methodologies

When investigating nanoparticles for drug delivery, there are a number of physicochemical metrics that are of interest, including the size, shape or aspect ratio, purity, chemical composition, surface charge, and the stability of the particles to name a few. Among those metrics, the size and size distribution for nanostructures are important, often dictating the biological activity and the fate of the particle. Perhaps the most common means to assess nanoparticle dimensions is Dynamic Light Scattering (DLS), where diffusion coefficients are measured from the time-dependent fluctuations of scattered light in solution. The particle r_h is subsequently calculated via the Stokes-Einstein relation. Alternatively, the material may be deposited on a surface and imaged by an optical, electron, or probe microscopy. Although microscopy is a powerful tool for sizing, some samples can yield misleading results when the sample preparation method affects particle swelling (e.g. dehydration) or if sample-substrate interactions disrupt the particle dimensions. In addition, detailed assessment of multicompartment nanogels and microgels is challenging through those approaches. As an example, two polymeric particles of identical r_h may have very different molar mass and density values that may influence their performance in vivo.

In this dissertation, light scattering tools are frequently described for assessing the physical characteristics of nanogels and microgels. Using Multiangle Light Scattering (MALS), the weight-average molar mass (M_w) and root-mean-square radius (r_{rms}) of particles was measured. This brief chapter serves the other sections of the dissertation, describing some basic theory behind molar mass measurements. Asymmetrical flow field-flow fraction (A4F) and Composition Gradient Static Light Scattering (CG-SLS)

were also used throughout this work to complement MALS detection. Basic theory of practice is described for those techniques as well.

2.2 Multiangle Light Scattering of Colloidal Dispersions

When the oscillating electric field of light encounters a very small particle suspended in a homogenous medium (e.g. air, water), the radiation induces an oscillating dipole moment in the particle with a magnitude proportional to the strength of the field and the polarizability of the scatterer. If we were to place a series of detectors around a solution of those particles (being illuminated with polarized laser light), one would notice that the intensity of scattered light is equal at all scattering angles (in the plane perpendicular to the polarization of the incident light). For the scattered light, the intensity can be represented by the ratio of the intensity of scattered light I over the intensity of the incident light I_0 according to Eq. 2.1 (the Rayleigh equation for plane polarized light).[1]

Eq. 2.1
$$\frac{I}{I_0} = \frac{16\pi^2\alpha^2\sin^2\theta}{\lambda^4 r^2}$$

Since the intensity of scattering is proportional to the polarizability of the particle (α), and the polarizability correlates with mass, light scattering may be used to measure the molar mass of various polymers in solution. In order to utilize these principles to calculate the molar mass of scatterers, some assumptions must be made regarding the nature of the light scattering (i.e. the Rayleigh approximation). For the Rayleigh approximation, the electric field of the incident wave is assumed to be homogeneous within the particle. Thus, the particle must be significantly smaller than the wavelength of incident light. The particle is also assumed to respond instantaneously to the oscillating electric field, and that the light does not slow down appreciably within the particle (a

more complete description of the Rayleigh-Gans-Debye approximation is provided in Section 2.2.1).[2] When these two criteria are assumed, the particle will act as a single dipole oscillating in-phase with electric field and will scatter light at all angles. The scattering angle (θ) is defined in **Scheme 2.1**.

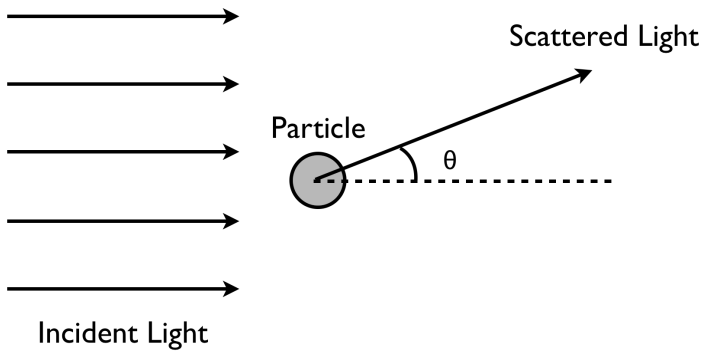

Scheme 2.1. Definition of scattering angle. Adapted from ref 2.

For dilute solutions of polymers in a typical experiment, intensity is quantified by the Rayleigh ratio ($R(\theta)$). The physical meaning of $R(\theta)$ is the attenuation of the incident beam by the loss of intensity after passage through a medium.[1]

Eq. 2.2
$$R(\theta) = \frac{I}{I_0} x \frac{r^1}{\sin^2 \phi}$$

where I is the intensity of the scattered light, I_0 is the intensity of the incident light, r is the distance between the detector and scattering volume, and ϕ is the angle between the plane of polarization of the incident light, and the plane defined by the incident and scattering beams. Thus, for small scatterers in solution with a mass concentration c, the weight average molar mass (M_w) of the polymer can be derived through Eq. 2.3

Eq. 2.3
$$R(\theta) = KcM_w$$

The optical constant K is defined by Eq. 2.4,

$$K = \frac{4\pi^2 n_0^2 V (dn/dc)^2}{\lambda^4 N_A}$$

Eq. 2.4

where n_0 is the refractive index of the solvent, *dn/dc* is the refractive index increment of the scatterer, V is the volume of the sample, and N_A is Avogadro's number. It is important to note the importance of the *dn/dc* in these relationships. The refractive index increment of particles is a result of the local polarizability of atoms within the macromolecule due to the displacement of electrons about their nuclei. For proteins and many peptides, the *dn/dc* value may be accurately predicted based on the amino acid composition of the molecule (typically averaging ~0.190 mL/g).[3] However, without accurate assessment of chemical composition for polymers and proteins, the *dn/dc* must be determined empirically.

2.2.1 Scattering from nanoparticles

When particles are not small relative to the wavelength of the incident beam (i.e. nanogels and microgels), a large amount of destructive interference occurs that reduces the intensity of scattered light when $\theta > 0$. In the following section, several relationships are described which quantitatively interpret this interference to yield size information (in addition to molar mass) for large particles. For a basic understanding, it is useful to review the Rayleigh-Gans-Debye (RGD) model.[2] As described earlier for small scatterers, we must assume that the incident light wave is unaffected by the scattering molecule. More specifically, the refractive index of the molecule is close to the refractive index of the solvent and the total phase shift of the light passing through the molecule is negligible (Eq. 2.5)

Eq. 2.5. $|m-1| << 1$ and $2ka|m-1| << 1$

where a is the size of the molecule (for spheres a denotes a radius), m is the refractive index of the scatterer relative to solvent ($m = n/n_0$) and $k = 2\pi n_0/\lambda$.[2] In contrast to small particles, we can consider a large particle as a collection of scattering subunits that each "experience" a homogeneous field. Each of the scattering units acts as a dipole scatterer, with an excitation and scattering that is independent of other subunits in the molecule. For a large particle, each unit scatters light with a different path length to the detector. Those differences in path lengths cause destructive interference due to phase differences in the scattered light, which ultimately reduces the intensity of light perceived by the detectors (Scheme 2.2) at all angles greater than zero.

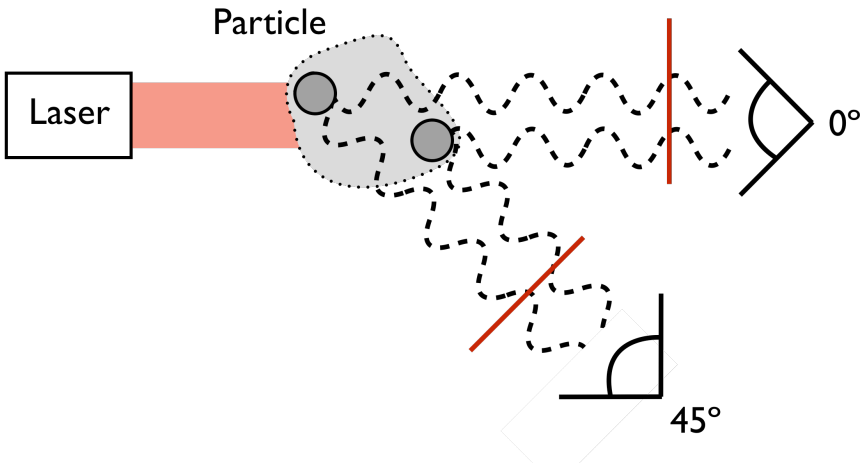

Scheme 2.2 Schematic illustration of the destructive interference for two scattering elements in a single particle. Scattered light (dashed wave) is detected at two angles relative to the incident beam (red).

In **Scheme 2.2**, a particle is shown that is much larger than the wavelength of light. Within the particle are two scattering elements that act as Rayleigh scatterers (dipoles responding instantly to the oscillating electric field of the incident light, scattering in all directions). Light reaching the zero angle detector is thus a sum of the two scattered waves that are in phase (assuming the contribution from transmitted light is

neglected). Alignment of the phases is schematically depicted as a red line (Scheme 2.2). However, at greater angles the light reaching the detector is out of phase due to path length differences in the scattered light, resulting in destructive interference and a decrease in light intensity compared to low angles.

The extent of destructive interference depends upon θ. At $\theta = 0$, the path lengths are equal and the destructive interference is negligible. The differences in intensity may be depicted through a scattering diagram (**Scheme 2.3**), representing the total intensity of scattered light (i.e. the sum of the polarized components of light scattered).

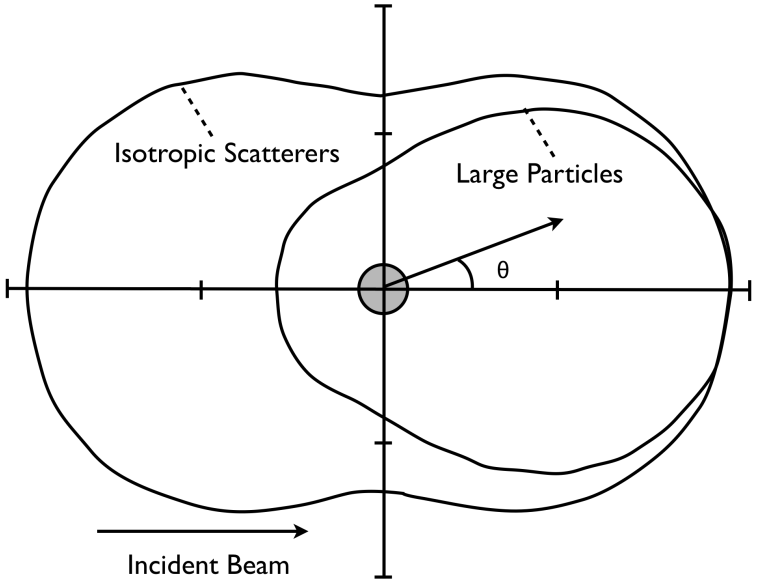

Scheme 2.3 Scattering diagram shows the shape of the scattering intensity as a function of angle for both small (Rayleigh, isotropic scatterers) and large particles.

As can be seen in **Scheme 2.3**, destructive interference occurs for large particles at all angles other than $\theta = 0$. In the limit of low scattering vector ($q = 4\pi n_0 \sin(\theta/2)/\lambda$), where the wavelength is large and scattering angle is low, the observed interference can be quantified by the form factor *P(θ)*.

Eq. 2.6
$$P(\theta) = 1 - \frac{16\pi^2 r_g^2 \sin^2(\theta/2)}{3\lambda^2}$$

where r_g is the gravimetric radius of the scattering molecule (also referred to as a root-mean-square radius, r_{rms}). The value of r_g is determined through integration over all of the mass elements of the molecule with respect to the center of gravity. There is often confusion regarding the subscript "g", which is sometimes referred to as a "radius of gyration". However, this is a misnomer since "gyration" refers to rotation about an axis in fixed space.[4] The r_{rms} may be more specifically defined in Eq. 5 for a molecule

Eq. 2.7
$$< r_{rms}^{\ 2} >= \frac{\sum_i r_i^2 m_i}{\sum_i m_i} = \frac{1}{M}\sum_i r_i^2 m_i$$

where r_i is the distance of element m_i from the center of mass of the molecule with total mass M.

In order to calculate the molar mass value for large spheres, one must eliminate the effects of destructive interference (i.e. measure *R(0)*). Unfortunately, measurements of scattering intensity at $\theta = 0$ are not possible since transmitted light dominates the detector signal. Instead, one measures the scattering intensity at multiple angles and extrapolates the intensity to zero angle. Previous work from Wahlund and coworkers has demonstrated the importance of the extrapolation method employed, where the Debye method for constructing the Debye plot was shown to be the most accurate for spheres.[5] Other common methods include the Zimm and Berry methods for constructing the Debye plot.[6-8] For the Debye method, the Debye plot is constructed with $R(\theta)/Kc$ as the ordinate and $\sin^2(\theta/2)$ as the abscissa (**Figure 2.1**). [9]

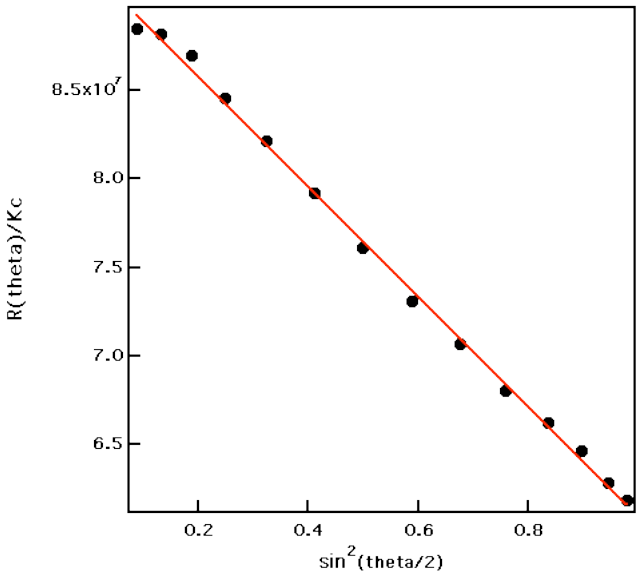

Figure 2.1 Example Debye plot for a nanogel.

Accounting for the form factor Eq. 4., the M_w and r_{rms} for dilute solutions of polymers may be determined through the well-known relationship shown in Eq. 2.8.

Eq. 2.8 $$\frac{R(\theta)}{Kc} = M_w P(\theta) - 2A_2 M^2 P^2(\theta) c + \ldots$$

If the concentration of polymers is assumed to be dilute, the value of A_2 becomes vanishingly small. Simplifying Eq. 5, and combining with Eq. 4, we arrive at the following relationship (Eq. 2.9) where the M_w may be derived from intercept of the Debye plot (0º scattering angle), whereas the r_{rms} may be derived from the slope at the intercept.

Eq. 2.9 $$\frac{R_\theta}{Kc} = M_w \left[1 - \left(\frac{16\pi^2}{3\lambda^2} \right) \langle r_{rms} \rangle^2 \sin^2\left(\frac{\theta}{2} \right) \right]$$

In the case of nanogels, a linear fit procedure to the angle-dependent data in the Debye plot is sufficient for calculating M_w and r_{rms}. As particle size is increased, the shape of the Debye plot changes, as reflected in **Figure 2.2** for latex standards of varying radius.

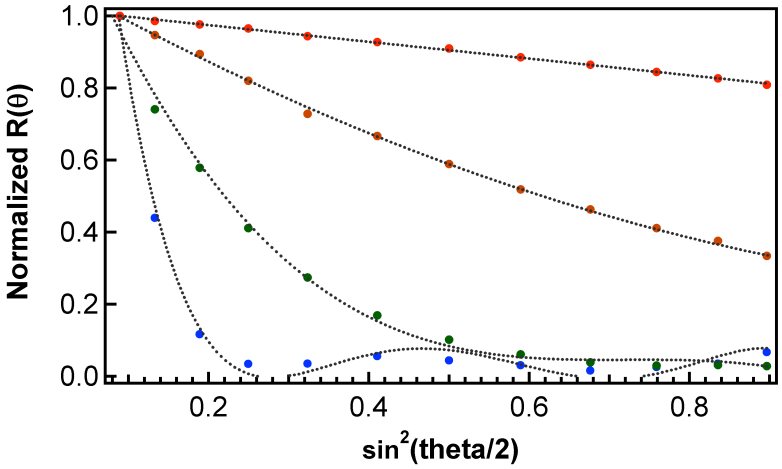

Figure 2.2 Size of polystyrene standards affects angular dependent fitting within the Debye plot. Particle radii represented include 0.0478 μm (red), 0.102 μm (orange), 0.200 μm (green), and 0.326 μm (blue) with corresponding polynomial fitting shown (grey).

Thus, for large nanoparticles and microparticles (>100 nm in diameter), polynomial curve fitting using the least-squares method is used to extrapolate to zero angle.

2.3 Asymmetrical Flow Field-Flow Fractionation

Asymmetrical flow field-flow fractionation (A4F) is frequently used in the separation of macromolecules, including nanoparticles and proteins.[10-17] Selectivity of separation is based on differences in solute diffusion coefficients, making A4F capable of separating a very broad range of macromolecule molar masses. Since A4F channels are open structures, typically ~100-500 μm thick, samples can often be run without filtration. The channels lack a physical stationary phase, which greatly reduces shear forces that can lead to degradation for high molar mass polymers. By separating a single population of particles, A4F further enables the assessment of particle size distributions. Instruments

are commonly composed of an impermeable upper plate that is separated from a porous membrane by a spacer of defined thickness (**Figure 2.3**).

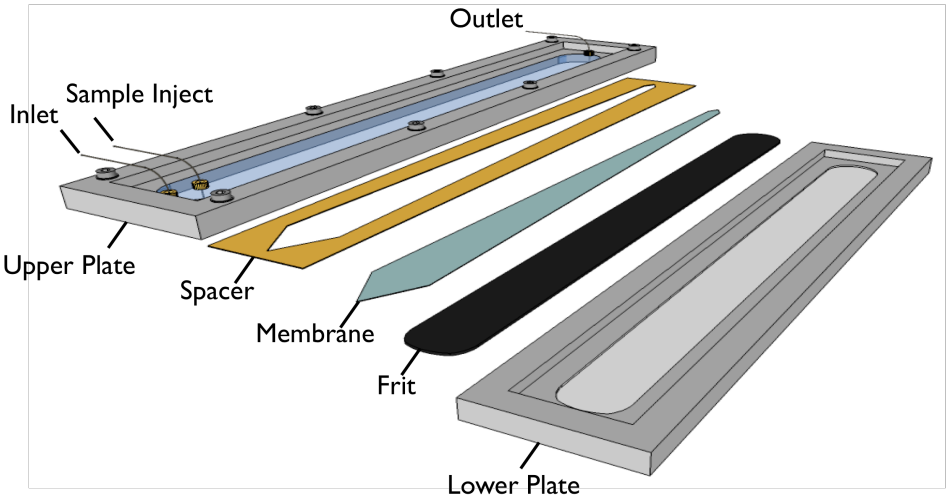

Figure 2.3 Instrument geometry for asymmetrical flow field-flow fractionation.

For the instrument configuration employed in this work, the spacer is 350 μm. The porous membrane is composed of regenerated cellulose (10,000 MWCO) and is supported by a porous frit and a lower plate below, forming a ribbon-like channel. Laminar flow of eluent through the channel results in a parabolic flow velocity, where the flow rates are slowest near the membrane (accumulation wall) and the impermeable upper plate (**Scheme 2.4**).[18]

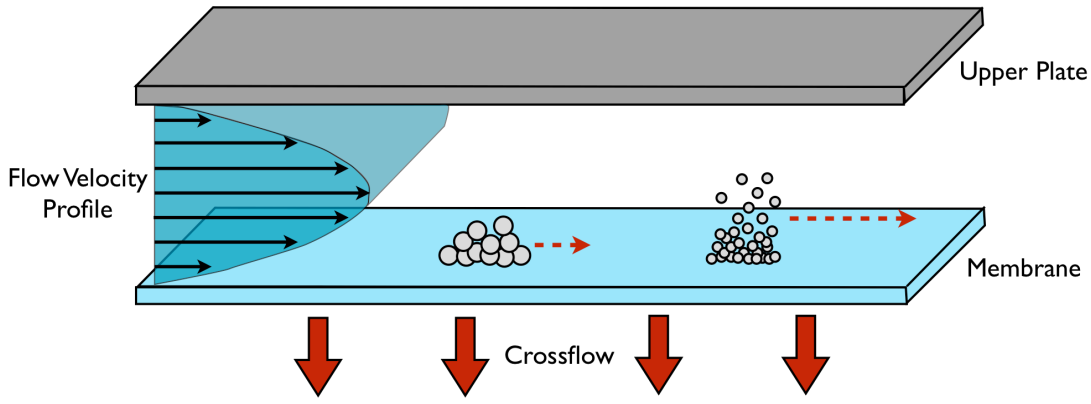

Scheme 2.4 Mechanism of separation via asymmetrical flow field-flow fractionation.

For A4F, a field is generated by pumping eluent through a permeable lower plate, which is covered by an ultrafiltration membrane.[16] This applied field-flow (cross-flow) is perpendicular to channel flow, driving injected particles towards the membrane (accumulation wall). In a typical separation scheme, particles are consistently driven towards the accumulation wall by the cross-flow while thermal motion of particulates (i.e. Brownian motion) counteracts the field. As eluent is eluted, smaller particles assume a higher mean steady-state distance from the wall, and thus elute at a faster rate.[10] In contrast, larger particles (with smaller diffusion coefficients) occupy regions closer to the accumulation wall and have greater retention in the channel.

According to A4F theory, the retention times (t_R) may be use to calculate the hydrodynamic radius (r_h) for eluting particles (Eq. 2.10).

Eq. 2.10
$$r_h = \frac{kT}{\pi\eta t^0 V_C w^2} * t_R$$

where η is the viscosity of the mobile phase, V_c is the crossflow rate, w is the thickness of the channel, and t_0 is the void time (time to elute an unretained solute from the channel).[16]

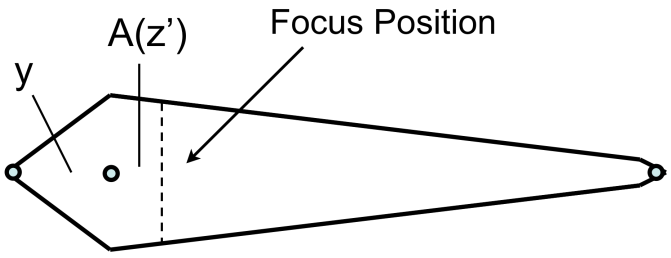

Scheme 2.5 Trapezoidal channel geometry in A4F.

The channel void time may be calculated if the geometry of the accumulation wall is known (**Scheme 2.5**), using Eq. 2.11-12.

Eq. 2.11
$$t^0 = \frac{V^0}{V_c} \ln\left(1 + \frac{V_c}{V_{out}}\left(1 - \frac{A(z') - y}{A_{tot}}\right)\right)$$

Eq. 2.12
$$V^0 = A_{tot} * \text{Height of Channel}$$

where A_{tot} is the area of the accumulation wall, y is the area of the tapered end beside the inlet, $A(z')$ is the uncorrected area of accumulation wall (inlet to focus). Although the spacer has a defined thickness (350 μm), the actual channel height must be experimentally determined since instrument variables (i.e. membrane swelling) may change the actual value of w. The value of w is measured by separating either a small globular protein of known r_h (e.g. ferritin or BSA) or a latex standard bead and subsequently calculating the value of w from Eq. 2.10. The actual channel height is typically ~270 μm (regenerated cellulose swells ~80 μm above the frit).

Although A4F theory may be applied to measure r_h values from separations, experimental variables (temperature gradients, band broadening, membrane interactions, local viscosity heterogeneity in separation) and the frequent need for standards makes the measurements challenging.[19-22] Instead, the A4F theory was applied in this dissertation work to assist in separation method development for a broad range of nanogel and microgel sizes. The eluting particles are conveniently detected by MALS, which is a powerful means to assess both the size and solution-average molar mass for a variety of macromolecules and nanoparticles (Section 2.2.). By coupling a concentration detector (e.g. differential refractometer, dRI) on-line, the *Mw* may be derived from the Debye plot, constructed using the Debye extrapolation method.[5]

2.4 Composition Gradient Static Light Scattering

Composition gradient static light scattering (CG-SLS) is a convenient batch characterization technique to assess the M_w, r_{rms}, and the second virial coefficient (A_2) for dispersions of polymers and proteins. Developed by Allen Minton for rapid quantification of protein interactions, the technique has been enabling for biophysical measurements.[23-25] Using CG-SLS, stoichiometry and equilibrium association constants of reversibly associating complexes can be measured. Additionally, the controlled delivery systems can be applied for rapid measurements of polymer *dn/dc*. However, one of the current limitations of the technique is the amount of sample needed for characterization (especially for binding constants). For most low molar mass samples (proteins, peptides), ~0.5 - 1 mg/mL quantities of material are typically required at large volumes. For example, assessment of equilibrium binding constants requires ~1 mL of each sample stock for a single replicate.[23] However, for high molar mass polymers (such as microgels and nanogels) significantly lower concentrations are required.

An example instrument configuration is shown in **Scheme 2.6**, consisting of three syringes pulling from three distinct reservoirs containing buffers or samples. The instrument is equipped with a degasser and filters in-line. For the instrument configured in **Scheme 2.6**, filters were excluded from syringe 2, which was equipped to deliver nanogels and microgels.

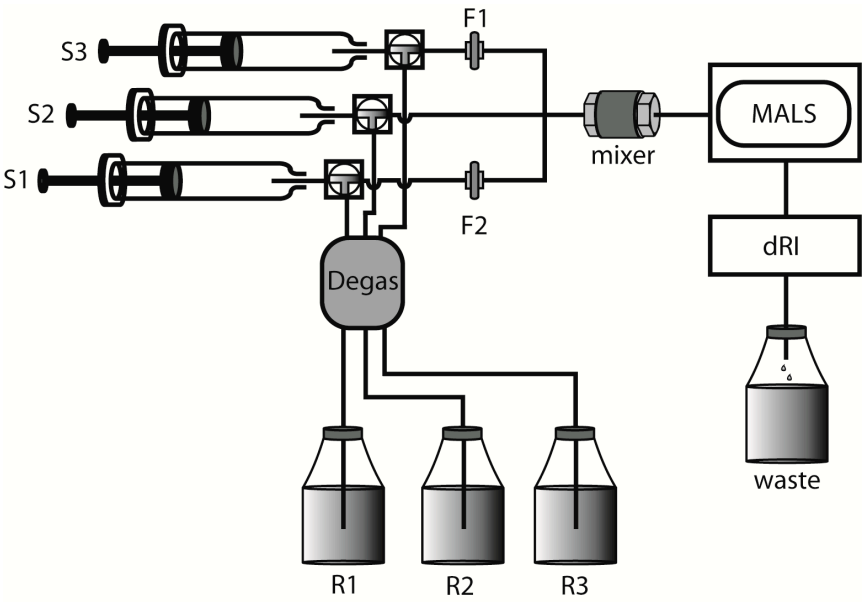

Scheme 2.6. Example schematic of flow system employed for particle characterization via CG-SLS. Buffers and reactants were placed in reservoirs R1-R3 and loaded into syringes S1-S3. Fluid was dispensed by the programmable tri-syringe pump, proceeding through inline 0.1 μm anodisc filters (F1, F2) and a static mixer before reaching the detectors. Filters were excluded from the syringe S2 flow line, containing microgel or nanogel samples.

The tri-syringe pump system is computer controlled, allowing the user to predetermine the sample flow rates (composition gradients) that are administered to the sequential MALS and dRI detectors online.

2.5 Outlook

Together, the techniques described in this chapter permit the design of increasingly complex microgel and nanogel structures. For instance, using MALS, polymer loss from degradable structures can be assessed directly through changes in molar mass (Chapters 4 and 5). In another example, the loading of therapeutic macromolecules into the internal network of a microgel can also be monitored by the mass gained by the carrier (Chapters 6 and 7). These tools have also enabled new synthetic efforts, where shell addition to core particles can be evaluated by mass changes in the structures directly (Chapter 7). Overall, these analytical techniques enhanced

quantitative characterization within the dissertation, and will enable the design of many multifunctional particle structures in the future.

2.6 References

1. Sun, S. F., *The Physical Chemistry of Macromolecules*. John Wiley & Sons, Inc: New York, 1994.

2. Hulst, H. C. v. d., *Light Scattering by Small Particles*. John Wiley & Sons, Inc.: New York, 1981.

3. Zhao, H. Y.; Brown, P. H.; Schuckt, P., On the Distribution of Protein Refractive Index Increments. *Biophys. J.* **2011,** *100* (9), 2309-2317.

4. Wyatt, P. J., Light-Scattering and the Absolute Characterization of Macromolecules. *Anal. Chim. Acta* **1993,** *272* (1), 1-40.

5. Andersson, M.; Wittgren, B.; Wahlund, K.-G., Accuracy in Multiangle Light Scattering Measurements for Molar Mass and Radius Estimations. Model Calculations and Experiments. *Anal. Chem.* **2003,** *75* (16), 4279-4291.

6. Zimm, B. H., The Scattering of Light and the Radial Distribution Function of High Polymer Solutions. *J. Chem. Phys.* **1948,** *16* (12), 1093-1099.

7. Zimm, B. H., Apparatus and Methods for Measurement and Interpretation of the Angular Variation of Light Scattering - Preliminary Results on Polystyrene Solutions. *J. Chem. Phys.* **1948,** *16* (12), 1099-1116.

8. Berry, G. C., Thermodynamic and Conformational Properties of Polystyrene .I. Light-Scattering Studies on Dilute Solutions of Linear Polystyrenes. *J. Chem. Phys.* **1966,** *44* (12), 4550-4564.

9. Debye, P., Molecular-Weight Determination by Light Scattering. *Journal of Physical and Colloid Chemistry* **1947,** *51* (1), 18-32.

10. Andersson, M.; Wittgren, B.; Wahlund, K. G., Ultrahigh molar mass component detected in ethylhydroxyethyl cellulose by asymmetrical flow field-flow fractionation coupled to multiangle light scattering. *Anal. Chem.* **2001,** *73* (20), 4852-4861.

11. Fraunhofer, W.; Winter, G.; Coester, C., Asymmetrical flow field-flow fractionation and multiangle light scattering for analysis of gelatin nanoparticle drug carrier systems. *Anal. Chem.* **2004,** *76* (7), 1909-1920.

12. Zillies, J. C.; Zwiorek, K.; Winter, G.; Coester, C., Method for quantifying the PEGylation of gelatin nanoparticle drug carrier systems using asymmetrical flow field-flow fractionation and refractive index detection. *Anal. Chem.* **2007,** *79* (12), 4574-4580.

13. Chuan, Y. P.; Fan, Y. Y.; Lua, L.; Middelberg, A. P. J., Quantitative analysis of virus-like particle size and distribution by field-flow Fractionation. *Biotechnol. Bioeng.* **2008,** *99* (6), 1425-1433.

14. Thielking, H.; Kulicke, W.-M., On-Line Coupling of Flow Field-Flow Fractionation and Multiangle Laser Light Scattering for the Characterization of Macromolecules in Aqueous Solution As Illustrated by Sulfonated Polystyrene Samples. *Anal. Chem.* **1996,** *68* (7), 1169-1173.

15. Blackburn, W. H.; Lyon, L. A., Size-controlled synthesis of monodisperse core/shell nanogels. *Colloid Polym. Sci.* **2008,** *286* (5), 563-569.

16. Wahlund, K. G.; Giddings, J. C., Properties of an asymmetrical flow field-flow fractionation channel having one permeable wall. *Anal. Chem.* **1987,** *59* (9), 1332-1339.

17. Litzén, A.; Wahlund, K.-G., Effects of temperature, carrier composition and sample load in asymmetrical flow field-flow fractionation. *J. Chromatogr. A* **1991,** *548*, 393-406.

18. Giddings, J. C., Field-flow fractionation - analysis of macromolecular, colloidal, and particulate materials. *Science* **1993,** *260* (5113), 1456-1465.

19. Litzen, A.; Wahlund, K. G., Zone Broadening and Dilution in Rectangular and Trapezoidal Asymmetrical Flow Field-Flow Fractionation Channels. *Anal. Chem.* **1991,** *63* (10), 1001-1007.

20. Caldwell, K. D.; Brimhall, S. L.; Gao, Y.; Giddings, J. C., Sample Overloading Effects in Polymer Characterization by Field-Flow Fractionation. *J. Appl. Polym. Sci.* **1988,** *36* (3), 703-719.

21. Litzen, A.; Wahlund, K. G., Effects of Temperature, Carrier Composition and Sample Load in Asymmetrical Flow Field-Flow Fractionation. *J. Chromatogr.* **1991,** *548* (1-2), 393-406.

22. Litzen, A., Separation Speed, Retention, and Dispersion in Asymmetrical Flow Field-Flow Fractionation as Functions of Channel Dimensions and Flow-Rates. *Anal. Chem.* **1993,** *65* (4), 461-470.

23. Kameyama, K.; Minton, A. P., Rapid quantitative characterization of protein interactions by composition gradient static light scattering. *Biophys. J.* **2006,** *90* (6), 2164-2169.

24. Fernandez, C.; Minton, A. P., Static Light Scattering From Concentrated Protein Solutions II: Experimental Test of Theory for Protein Mixtures and Weakly Self-Associating Proteins. *Biophys. J.* **2009,** *96* (5), 1992-1998.

25. Minton, A. P., Static light scattering from concentrated protein solutions, I: General theory for protein mixtures and application to self-associating proteins. *Biophys. J.* **2007,** *93* (4), 1321-1328.

CHAPTER 3

MULTIFUNCTIONAL NANOGELS FOR THERAPEUTIC SIRNA DELIVERY

Adapted from

Smith MH, Lyon LA. *Acc. Chem. Res.*, 2012 (ASAP) DOI: 10.1021/ar200216f

Blackburn WH*, Dickerson EB*, Smith MH*, McDonald JM, and Lyon LA. *Bioconjug. Chem.* 2009, 20, (5), 960–968
*equal contributing author

3.1 Introduction

Significant effort has been invested in the design of colloidal drug carriers in order to improve drug localization and bioavailability.[1-3] Ideally, an actively targeted particulate drug carrier will increase the therapeutic efficacy of a drug by delivery to the diseased site, while reducing drug-associated side effects. Attainment of this goal would greatly advance treatment of diseases (e.g. cancer) where the toxic effects of therapeutics administered systemically may outweigh their benefit. To date, many types of delivery vehicles have been explored for *in vitro* and *in vivo* drug delivery applications, including inorganic nanoparticles,[4-5] polyelectrolyte complexes,[6] liposomes,[7-8] block co-polymer micelles,[9-11] and polymeric nanoparticles.[12-15]

A particularly compelling phenomenon from the standpoint of cancer therapy is RNA interference (RNAi). RNAi is a relatively new approach to gene silencing, which has been demonstrated effective both *in vitro* and *in vivo*.[16-17] This technique employs small 21-25 nucleotide long double stranded small interfering RNAs (or siRNAs) to inhibit gene expression through degradation of a targeted mRNA.[18] Whereas the potential for therapeutic oncology applications exist where siRNA would be used to specifically

shut down genes necessary for tumor growth, the lack of efficient methods for *in vivo* siRNA delivery prevent widespread therapeutic use.[16-17] As described in Chapter 1, intravenous delivery of siRNA is challenging due to its polyanionic nature and high molecular weight (~13 kDa), preventing transport across the cell membrane.[16-17] Thus, effective siRNA carriers must enable efficient transport through the vasculature to the tumor, and then must additionally enable intracellular delivery of the cargo. A common method currently used for siRNA delivery *in vitro* employs cationic lipid-based carriers[16-17, 19] or polyelectrolytes.[6] These charged moieties form polyplexes with the siRNA, forming aggregates that can be taken up into the cells, thereby delivering the siRNA to the cytosol. However, these carriers can have notable drawbacks with respect to toxicity and difficulties in specific cell targeting,[16-17, 20] thereby giving rise to a need for alternative delivery methods. A number of new approaches have been reported that overcome some of the shortcomings of lipid-based approaches. For example, Schiffelers et al. used an RGD (Arg-Gly-Asp peptide ligand)-PEG-PEI complex to target siRNA to tumor neovasculature.[21] Song et al. presented the use of a protamine-antibody fusion protein using the Fab fragment of HIV-1 envelope antibody for siRNA delivery.[22] Another targeting motif has been the use of liposomes in the form of an immunoliposome complex reported by Pirollo et al.[23] A number of other similar approaches have been taken[6, 20, 24-29] and these siRNA carriers have enabled certain degrees of success. However, issues of toxicity, leakiness, and payload capacity still persist, especially in the context of *in vivo* gene silencing.[16-17]

Building upon many of the lessons learned from these approaches, we and others have developed drug delivery methods that employ the synthetic hydrogel nanoparticle (nanogel).[13, 15, 30-31] Nanogels possess a high degree of porosity, permitting a high payload capacity, and can also be selectively surface functionalized to enable tumor-specific targeting. Thus, we have developed straightforward, scalable syntheses of surface-functionalized, ~100-nm diameter, core/shell nanogels composed of poly(*N*-

isopropylmethacrylamide) (pNIPMAm),[32-33] an amphiphilic polymer that is hydrated at physiological temperature and is likely therefore to resist protein adsorption relative to more hydrophobic carriers. This polymer has also garnered interest due to its dramatic thermoresponsivity; it undergoes an entropically driven coil-to-globule (swollen-to-collapsed) transition at ~43 ºC, which may have utility for thermally-triggered delivery (Chapter 1).[32-33] However, in the present chapter, this thermoresponsivity is only used to enable the synthesis of monodispersed core/shell nanogels via precipitation polymerization, as we have discussed previously.[32, 34] The core/shell pNIPMAm nanogel construct used to encapsulate and deliver siRNA to ovarian cancer cells is illustrated in **Scheme 3.1**.

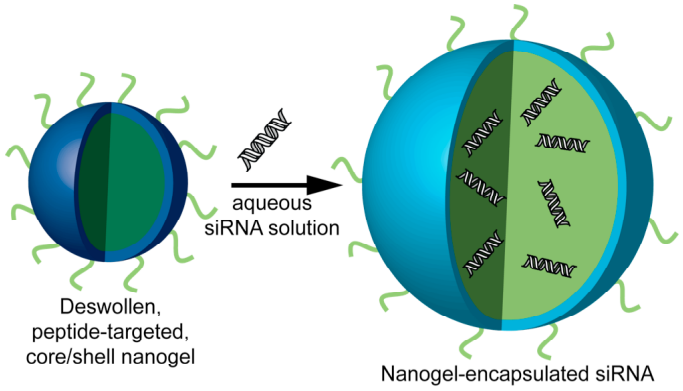

Scheme 3.1 Non-covalent encapsulation of siRNA in peptide-targeted core/shell nanogels.

A previously described 12 amino acid peptide (YSAYPDSVPMMS or YSA)[35] was coupled to surface of ~100-nm diameter core/shell nanogels to permit cell-specific targeting and subsequent delivery of high concentrations of siRNA to the target cells. The YSA peptide mimics the ligand ephrin-A1, which binds to the erythropoietin-producing hepatocellular (Eph) A2 receptor. In addition to specific expression in neovasculature,[36-37] EphA2 is highly expressed by a number of tumor cells including those derived from ovarian,[38-39] prostate,[40-41] breast,[42-43] and colon[44-45] cancers, making it an excellent target for tumor-specific delivery. This chapter demonstrates that pNIPMAm nanogels have a

high loading capacity for siRNA, and that these nanogels can be delivered to the cytoplasm of ovarian cancer cells via ligand-receptor binding mediated endocytosis. Importantly, overt cytotoxicity was not observed to arise from the nanocarrier, suggesting that this approach could be an efficacious one. In addition, delivery of siRNA to cells in culture can be performed in the presence of serum, suggesting that nanogels may be of particular advantage for *in vivo* delivery.

3.2 Experimental Section

3.2.1 Materials

All materials were purchased from Sigma-Aldrich (St Louis, MO) and used as received unless otherwise noted.

3.2.2 Nanogel Core Synthesis

Nanogel core particles were synthesized by free-radical precipitation polymerization, as previously reported.[32] The use of thermally phase separating polymers enables the use of precipitation polymerization for the synthesis of highly monodispersed nanogels.[32] The molar composition was 98% *N*-isopropylmethacrylamide (NIPMAm), 2% *N,N'*-methylenebis(acrylamide) (BIS), with a total monomer concentration of 140 mM. The solution also contained a small amount (~0.1 mM) of acrylamidofluorescein (AFA) to render the nanogels fluorescent for visualization via confocal microscopy.[30, 32] In a typical synthesis, 100 mL of a filtered, aqueous solution of NIPMAm, BIS, and sodium dodecyl sulfate (SDS, 8 mM total concentration) was added to the reaction flask, which was then heated to 70 ºC. The solution was purged with N_2 gas and stirred vigorously until the temperature remained stable. The AFA was added, and after 10 minutes the reaction was initiated by the addition of a 1 mL solution of 800 mM ammonium persulfate (APS) to make the final concentration of APS in the reaction ~8

mM. The solution turned turbid, indicating successful initiation. The reaction was allowed to continue for 4 h under an N_2 blanket.

3.2.3 Nanogel Shell Synthesis

The core nanogels described above were used as seeds for the addition of a hydrogel shell in a seeded precipitation polymerization scheme. The detailed procedure of the shell synthesis has been reported previously.[32] Briefly, 10 mL of the core nanogel solution and 0.0577 g SDS were first added to a three-neck round-bottom flask and heated under N_2 gas to 70 ºC. A 50 mM monomer solution with molar ratios of 97.5% NIPMAm, 2% BIS, and 0.5% aminopropylmethacrylate (APMA, Polysciences, Warrington, PA) was prepared in 39.5 mL of dH_2O. The solution was added to the three-neck round-bottom flask, and the temperature was stabilized at 70 ºC while continuously stirring. The reaction was initiated by a 0.5 mL aliquot of 0.05 M APS. The reaction proceeded for 4 h under N_2 gas. Following the synthesis, the solution was filtered through Whatman filter paper, and the nanogels were purified by centrifugation followed by resuspension in dH_2O.

3.2.4 Nanogel Characterization

Multiangle light scattering (MALS) (Wyatt Technology Corporation, Santa Barbara, CA) detection following asymmetrical flow field-flow fractionation (A4F) was used to determine the distribution of root-mean square radii (r_{rms}) for all nanogels (Chapter 2). For all separations, a cross-flow of 0.30 mL/min was used with a channel flow of 1.0 mL/min. The MALS detector is equipped with a Peltier device to maintain a flow cell temperature of 25 °C and collects scattered light from 16 different fixed angles to determine the r_{rms} of the nanogels. By measuring r_{rms} as a function of elution time, we constructed a chromatogram that permits the determination of the weight fraction of nanogels as a function of radius, thereby providing a sample polydispersity. ASTRA

5.1.5.0 software was used to determine r_{rms} values using the Debye fit method. The core/shell nanogels synthesized using the methods described above were determined to have r_{rms} values of ~54 nm with size polydispersities of <10%, as described previously.[32] Characterization of the refractive increment (*dn/dc*) of nanogels was performed to determine particle molecular weight by static light scattering. Differential refractive index analysis (dRI, OptiLab rEX, Wyatt Technologies, Inc.) was performed in batch mode. To ensure accurate data, the refractive index was calibrated prior to each measurement using sodium chloride concentrations ranging from 0.1 mg/mL to 15.0 mg/mL. All nanogel dilutions were prepared in dust-free vials, which were rinsed sequentially with deionized water, absolute ethanol, and HPLC-grade acetone. Nanogels were resuspended in distilled, deionized water over a concentration range from 2.5×10^{-6} g/ml to 3.75×10^{-4} g/mL. The use of MALS in conjunction with the rEX differential refractometer permitted the measurement of the M_w from the determined *dn/dc* values and the angle dependent light scattering data.

3.2.5 YSA synthesis

The YSA peptide (YSAYPDSVPMMSC) was synthesized using standard Fmoc chemistry as described previously.[46] Peptide synthesis was carried out by K.D. Clark, University of Georgia. Following synthesis, the peptide was cleaved from the resin and deprotected for 4 h in reagent K after air-drying. The peptide was purified using a series of 5 mL injections onto a preparatory HPLC column (10-m; particle size, 21.2 mm 25 cm, Jupiter C18; Phenomenex Inc., Torrance, CA) using HPLC-grade H_2O and a linear gradient of acetonitrile (0–70 min, 10–80%) at 5 mL per min. Both the acetonitrile and H_2O contained 0.05% trifluoroacetic acid. The desired peak was identified by matrix-assisted laser desorption ionization time-of-flight mass spectrometry, and the peaks from multiple runs were pooled, lyophilized, and stored at 4 ºC in solid form. A scrambled form (SCR) of the YSA peptide (DYPSMAMYSPSVC) was also synthesized via this

method for use as a control. On other occasions, the YSA and SCR peptides were purchased from GenScript Corp (Piscataway, NJ).

3.2.6 Peptide Conjugation

In this study we produced a maleimide-functionalized nanogel through the EDC coupling of ε-maleimidocaproic acid (EMCA) to the primary amines in the shell of the nanoparticle. As described in the nanogel shell synthesis, primary amines were introduced through the copolymerization of APMA (0.5% molar ratio). Given that APMA is efficiently incorporated at these low molar ratios, we can estimate the amine equivalents available for bioconjugation (~2.2×10^{-6} amines per 88.3 mg of lyophilized particles). From this estimate, peptide coupling was performed by introducing YSA peptide in a 1:1 molar ratio with amine (YSA molecular weight = 1450.66 g/mol). The YSA peptide was then conjugated to the nanogels via maleimide coupling to the cysteine residue on the C-terminal end of the peptides.

First, 88.3 mg of nanogels (~2.2×10^{-6} amine equivalents) was resuspended in 35.0 mL of pH 6.0 MES buffer and allowed to shake for 2 hours. A second solution was prepared where 4.4×10^{-6} moles (0.68 mg) of 1-ethyl-3-methyl-(3-dimethylaminopropyl) carbodiimide (EDC, Pierce, Rockford, IL), 4.4×10^{-6} moles (0.96 mg) *N*-hydroxysulfosuccinimide (NHSS) and 2.2×10^{-6} moles (0.46 mg) of EMCA were dissolved in 3.0 mL of pH 6.0 MES buffer. This solution was reacted for 30 min at room temperature to activate the EMCA acid groups, which permits amide coupling to take place between the EMCA acid groups and the amines on the nanogel surface. This activated EMCA solution was then added to the nanogel solution and reacted for 2 h on a shaker table. The nanogels were centrifuged 3 times to remove any unreacted material, with resuspension in pH 6.0 MES buffer following each centrifugation. Finally, 3.2 mg of the appropriate peptide was added to the activated nanogels and reacted overnight.

Peptide-functionalized nanogels were purified by centrifugation and resuspended in distilled, deionized water.

The number of bioconjugated YSA targeting peptides per particle was estimated by considering the number of primary amines available for conjugation and the number density of nanogels used during bioconjugation (as measured by static light scattering). Through differential refractometry, the nanogel refractive increment was determined to be 0.176 ± 0.002 mL/g. Measurement through MALS detection provided the molar mass of non-conjugated particles, $M_w = 2.19 \times 10^7$ g/mol (1º Debye fitting, 0.1% fit error). Thus, a total mass of 88.3 mg of lyophilized particles used during conjugation is equivalent to 2.43×10^{15} particles. Assuming a 50% peptide conjugation efficiency[47] and 2.2×10^{-6} amine equivalents available for bioconjugation, we conservatively estimate a peptide density of ~225 YSA peptides/particle.

3.2.7 *In vitro* siRNA Encapsulation and Release

Our group employs a "breathing-in" method for the encapsulation of various macromolecules within nanogels. In a typical method, lyophilized nanogels are resuspended in an aqueous solution containing the macromolecule to be loaded. Importantly, this is done using a loading solution volume that is almost completely imbibed by the swelling nanogels. In this fashion, the hydrogel network imbibes the payload with high efficiency and without relying on simple equilibrium partitioning to determine the maximum loading level. To determine the rate of siRNA release from nanogels loaded in this fashion, a mixture of oligonucleotide was prepared containing 0.250 mL of 20 μM siGLO red transfection indicator and 1.00 mL of 20 μM siGENOME Lamin A/C control siRNA (Dharmacon, USA). Particles were resuspended in this mixture at a concentration of 4 mg per 250 μL siRNA solution. This concentration of particles is near the solubility limit for the nanogels in PBS, ensuring a high degree of

solvent and solute uptake into the hydrogel network. The particles were allowed to resuspend for 12 hours at room temperature while shaking.

The encapsulation efficiency was determined via ultracentrifugation of the nanogel loading solution and measurement of supernatant siRNA concentration by UV-vis spectroscopy (Shimadzu UV-1601). The moles of siRNA in the loading solution ($m_{siRNA,\ Loading}$) and in the supernatant ($m_{siRNA,\ Supernatant}$) were determined via interpolation from a separately constructed standard curve of absorbance vs. concentration ($R^2 > 0.99$). The encapsulation efficiency (EE) of the system could then be calculated through analysis of the amount of siRNA in the loading solution and the remaining moles of siRNA in the supernatant after nanogel swelling was complete, as illustrated by Eq. 3.1 and in similar encapsulation experiments.[48]

$$EE = \frac{m_{\text{siRNA, Loading}} - m_{\text{siRNA, Supernatant}}}{m_{\text{siRNA, Loading}}} \times 100$$

Eq. 3.1

The release of solutes from nanogels was performed in 10% serum to simulate physiological conditions. Release experiments were performed by dispersing 200 μL of loaded nanogels in 2.20 mL of 0.01 M phosphate buffered saline containing 10% fetal bovine serum (equilibrated at 37 ºC) in 3.2 mL polycarbonate centrifuge tubes (Beckman Coulter, USA). The nanogel suspension was allowed to incubate at 37 ºC while shaking. At specific time points, the tubes were centrifuged for 90 min at 687 000 × g (at 37 ºC), and an aliquot of supernatant (0.75 mL) was removed for UV-vis analysis. This volume was replaced with fresh buffer. Upon centrifugation, the gel pellet had a homogenously distributed bright pink color, indicating significant retention of siRNA throughout the experiment. The cumulative siRNA released was calculated by calculating the total moles detected in the supernatant as a function of time, as described in Eq. 3.2.

$$\text{Cumulative siRNA Released} = \frac{m_{\text{TOTAL siRNA, Supernatant}}}{m_{\text{siRNA, Loading}}} \times 100$$

Eq. 3.2

All release studies were performed in triplicate for statistical analysis, using identical nanogel loading and release conditions.

3.2.8 ζ-potentiometry

Excluding the 0.5 mol% APMA copolymerized into the shell of our nanogel particles, the nanogels are composed of largely non-ionic monomers. To confirm their suspected electroneutrality, which should be critical for reducing non-specific cell and protein interactions, we measured the ζ-potential of both YSA-conjugated and non-conjugated core/shell nanogels (Zeta-Sizer Nano, Malvern, U.K.). All nanoparticles used in this investigation demonstrated ζ-potential values < +0.300 mV, suggesting that they are only weakly charged and should therefore not interact strongly with serum proteins or cell surfaces via Coulombic forces.

3.2.9 Cell Culture

Hey cells were provided by Gordon W. Mills, Department of Molecular Therapeutics, the University of Texas, M.D. Anderson Cancer Center. Hey cells were cultured in RPMI 1640 (Mediatech, Manassas, VA) supplemented with 10% v/v heat-inactivated fetal calf serum (Invitrogen), 2 mM L-glutamine (Mediatech), 10 mM HEPES buffer (Mediatech), penicillin (100 U/ml), and streptomycin (100 μg/mL). The BG-1 cell line was provided by Julie M. Hall and Kenneth S. Korach, Receptor Biology Section, Laboratory of Reproductive and Developmental Toxicology, National Institute of Environmental Health Sciences, NIH, Division of Intramural Research, Environmental Disease and Medicine Program, Research Triangle Park, NC. BG-1 cells were propagated

in DMEM:F12/50:50 (Mediatech) supplemented with 10% v/v heat-inactivated fetal calf serum, penicillin, and streptomycin.

3.2.10 siRNA Encapsulation for Cell Studies

Using the "breathing-in" method for encapsulation (as described above), dried nanogels were reswollen in the presence of the siRNA, thereby imbibing the solute within the hydrogel network. In a typical procedure for *in vitro* cell delivery, a 20 μM solution (250 μL) of a fluorescent siRNA transfection indicator, siGLO (Dharmacon), or EGFR siRNA (Dharmacon, Lafayette, CO) was prepared in phosphate buffered saline (PBS). Lyophilized nanogels were dissolved in the siRNA solution at a concentration of 4 mg in 250 μL and allowed to shake overnight at room temperature. Importantly, this nanogel concentration results in nearly all of the solvent being taken up by the nanogels. This volume-filling approach ensures a maximal uptake of siRNA within the nanogels. After shaking, the nanogels were centrifuged to remove any free siRNA and resuspended in PBS. A standard curve for increasing concentrations of siRNA was made by measuring the absorbance at 260 nm using a Shimadzu UV 1601 spectrophotometer. After siRNA was encapsulated in the nanogels, they were centrifuged, and the absorbance of the supernatant was measured to determine the amount of incorporated siRNA.

3.2.11 Cell Transfection Using Nanogels

Hey or BG-1 cells were plated onto an 8-well chamber slide (5×10^3 cells/well), and the cells allowed to adhere overnight at 37 ºC in a 5% CO_2 atmosphere. After washing the wells with PBS and replacing the media, siGLO-loaded/YSA-conjugated nanogels, unloaded YSA-conjugated nanogels, pNIPMAm nanogels, or siGLO only were added to wells. Cells were incubated in each case for 4 h. In experiments where preincubation of ephrin-A1 was used to initiate internalization and degradation of EphA2, ephrin-A1 was added to the media at a final concentration of the ligand of 2 μg/mL. After

incubation, the cells were washed with PBS, and the medium replaced. For fixation prior to confocal imaging, the cells were incubated with 2% (v/v) paraformaldehyde for 30 min.

3.2.12 Immunoblotting

Hey cells were plated into 6-well plates (5×10^5/ well) and allowed to adhere overnight at 37 ºC, 5% CO_2. The cells were lysed with 100 µL of lysis buffer (50 mM Tris-HCl, pH 7.5, 150 mM NaCl, 2 mM EDTA (Fisher), 2 mM EGTA (Fisher), 1 mM sodium orthovanadate, 2.5 mM sodium pyrophosphate, 1 mM β-gycerolphosphate, 1 mM phenylmethanesulfonyl fluoride, 10 µg/mL aprotinin, 10 µg/mL leupeptin, 1% Triton X-100, and 5% glycerol), and the cell lysates sonicated four times for five seconds each. The lysates were cleared by centrifugation at 11,000 × g rcf for 15 min at 4 ºC. Cell lysates were prepared for analysis by the addition of an equal volume of Laemmli 2X sample buffer. The samples were heated to 95 ºC for 5 min to denature the proteins. The proteins were separated on a 10% SDS-PAGE gel and transferred onto nitrocellulose. The blots were blocked with either 5% nonfat dry milk (NFDM) or 5% bovine serum albumin (BSA) in 10 mM Tris-buffered saline, pH 7.5 plus 1% Tween 20 (TBST, BioRad) for 1 hour at room temperature. The blots were probed with anti-EGFR antibody (Cell Signaling, Danvers, MA; cat. no. 4405) or with a b-actin antibody (Millipore, Billerica, MA; Mab1501) diluted in 5% NFDM or 5% BSA overnight, with shaking at 4 ºC. For EphA2 detection, the blots were probed with an anti-EphA2 polyclonal antibody (Santa Cruz Biotechnology, Santa Cruz, CA; sc-294). The blots were washed three times with TBST and probed with goat anti-rabbit IgG (Santa Cruz, sc-2004) or with goat anti-mouse IgG (Santa Cruz, sc-2005) linked to horseradish peroxidase (HRP). Bands were visualized on film (Pierce) using the ECL reagent, SuperSignal West Pico™ (Pierce).

3.2.13 Confocal Microscopy

A Zeiss LSM510 confocal microscope was used to take cell images. Cells were incubated with nanogels for 4 h. After 4 h, the cells were washed and then fixed on the slide. An Ar^+ laser was used to excite the AFA-labeled nanogels, whereas a HeNe laser was used to excite the fluorescently labeled siGLO. LSM510 software was used to view the images.

3.2.14 Flow Cytometry

Hey cells were plated at 2.5 x 10^5 cells/well in a 12-well, cell culture plate. Cells were allowed to adhere overnight in an incubator at 37 ºC in a 5% CO_2 atmosphere. Cells were washed, and fresh medium was added containing YSA-pNIPMAm or SCR-pNIPMAm nanogels at a concentration of 0.8 mg/mL and incubated for four hours. Following incubation, the cells were washed with PBS and removed from the plate by Trypsin-EDTA treatment. The cells were washed with PBS and fixed with 2% (v/v) paraformaldehyde. Cells were analyzed using a LSR Flow Cytometer (BD Biosciences). Data analysis was carried out using FlowJo software.

3.2.15 Toxicity Studies

Trypan blue exclusion assay. Hey cells were plated onto an 8-well chamber slide (1×10^4 cells/well) and allowed to adhere overnight at 37 ºC and 5% CO_2. The media was removed, the wells washed with PBS, and the medium replaced. PNIPMAm nanogels, YSA-conjugated nanogels, and SCR-conjugated nanogels were added to cells and incubated for 72 h. Untreated cells were used as controls. After 72 h, the cells washed with PBS, and a 1:1 solution of trypan blue was added to each well. After 1 min, the trypan blue was removed, the cells were washed with PBS, fixed with 2% (v/v) paraformaldehyde, and air dried. Each well was then viewed via bright field microscopy to determine the number of stained (dead) versus unstained cells. Five fields were viewed for each treatment.

Tox 8 assay. Hey cells were plated onto 96-well plates (1×10^4 cells/well) and allowed to adhere overnight at 37 ºC and 5% CO_2. The media was removed, and the cells were washed with PBS followed by replacement of the medium. Cells incubated with EGFR siRNA-loaded YSA-labeled nanogels, unloaded YSA-labeled pNIPMAm nanogels, unlabeled pNIPMAm, or YSA peptide alone were tested using this assay. The cells were incubated under all conditions for 4 h. The cells were then washed with PBS, the medium replaced, and the cells incubated for an additional 72 h in medium. The Tox 8 reagent (Sigma) was added to the cells according to the manufacturer's instructions. The absorbance at 600 nm was read after 1 hour, and the extent of cellular viability/proliferation determined.

3.3 Results and Discussion

The nanogels described in this chapter were developed around two main design criteria, as depicted in **Scheme 3.1**. For this application, both peptide-based targeting of ovarian cancer and efficient encapsulation and delivery of siRNA are required. The core/shell nanogels synthesized using the methods described above were determined to have r_{rms} values of ~54 nm with size polydispersities of < 10%, as described previously.[32] To determine the timescale for retention of siRNA within the pNIPMAm nanogels, we investigated siRNA leakage using simulated physiological conditions. As described above, nanogels were loaded using a model mixture of siRNA, containing both the siGLO red transfection indicator and the siGENOME Lamin control. The nanogel was observed to encapsulate the siRNA with high efficiency (93 ± 1%), which is equivalent to a loading level of 1.6 wt% or 16 μg siRNA/mg of nanogels.

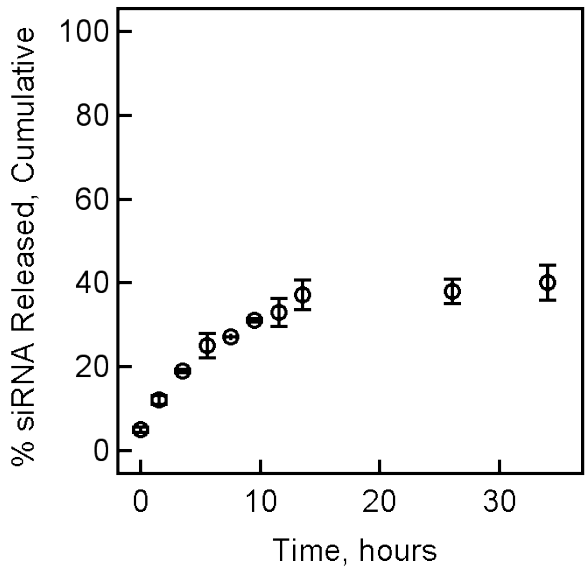

Figure 3.1 siRNA release profile from nanogels at 37 ºC in PBS containing 10% fetal bovine serum. The error bars represent ±one standard deviation about the mean value (n=3).

As shown in **Figure 3.1**, only ~33% of the siRNA is observed to leak from the nanogels within the first 12 hours (67% retained). This approximate level of retention persists out to 35 hours, suggesting very efficient entrapment of the siRNA within the nanogel network. Retention of this magnitude is promising for intravenous oligonucleotide delivery given previously determined timescales (~6 hours) for extravasation *via* the enhanced permeability and retention effect.[49]

To establish the efficacy of targeting *in vitro*, we determined the uptake of nanogels by two ovarian cancer cell lines, Hey and BG-1. We previously demonstrated high expression of EphA2 by Hey cells and low expression of the receptor by the BG-1 cell line.[50] Because of these differences in EphA2 expression, we expected to see higher levels of nanogel uptake via receptor-mediated endocytosis with Hey cells as compared to BG-1 cells. Furthermore, we expected that the degree of siRNA delivery to those cells would be dependent on the cell type and the presence of the peptide ligand. To load siRNA into the nanocarrier, lyophilized nanogels were loaded with siGLO (a fluorescently-labeled siRNA delivery tracker) by reswelling them in a concentrated

solution of the siRNA, as described above. To obtain a relative concentration of the siGLO taken up by the nanogels, absorbance measurements were compared to a standard curve of siGLO in solution (R^2>0.99). We determined in a series of three trials that 80-95% (by mass) of the siGLO was incorporated into the nanogels by this method, in agreement with the loading levels calculated in the release kinetics experiment described above.

Following loading with siGLO, nanogels were incubated with either Hey (high EphA2 expression) or BG-1 (low EphA2 expression) cells in order to compare the levels of targeted uptake by ovarian cancer cells. Uptake of the nanogels into the cells was followed using a fluorescent tag (AFA) incorporated into the nanogel core as well as by the fluorescence of the siGLO. In previous studies, we determined that high levels of nanogel uptake by cells occurred after four hours. As a result, cells were incubated for four hours with siGLO-loaded/YSA-conjugated nanogels to monitor specific targeting to EphA2. Unloaded YSA-conjugated nanogels, non-targeted pNIPMAm nanogels, and siGLO only were used as controls, with identical 4-hour incubation times. In all experiments described in this chapter, we maintained a constant nanogel/cell ratio of 1 mg nanogels/5×10^5 cells. For siRNA-loaded nanogels, this corresponds to 16.6 μg siRNA/5×10^5 cells. After incubation, the cells were washed, and the slides fixed for confocal microscopy imaging. **Figure 3.2** shows that Hey cells targeted with YSA-conjugated nanogels have high levels of nanogel uptake as indicated by the presence of green fluorescence.

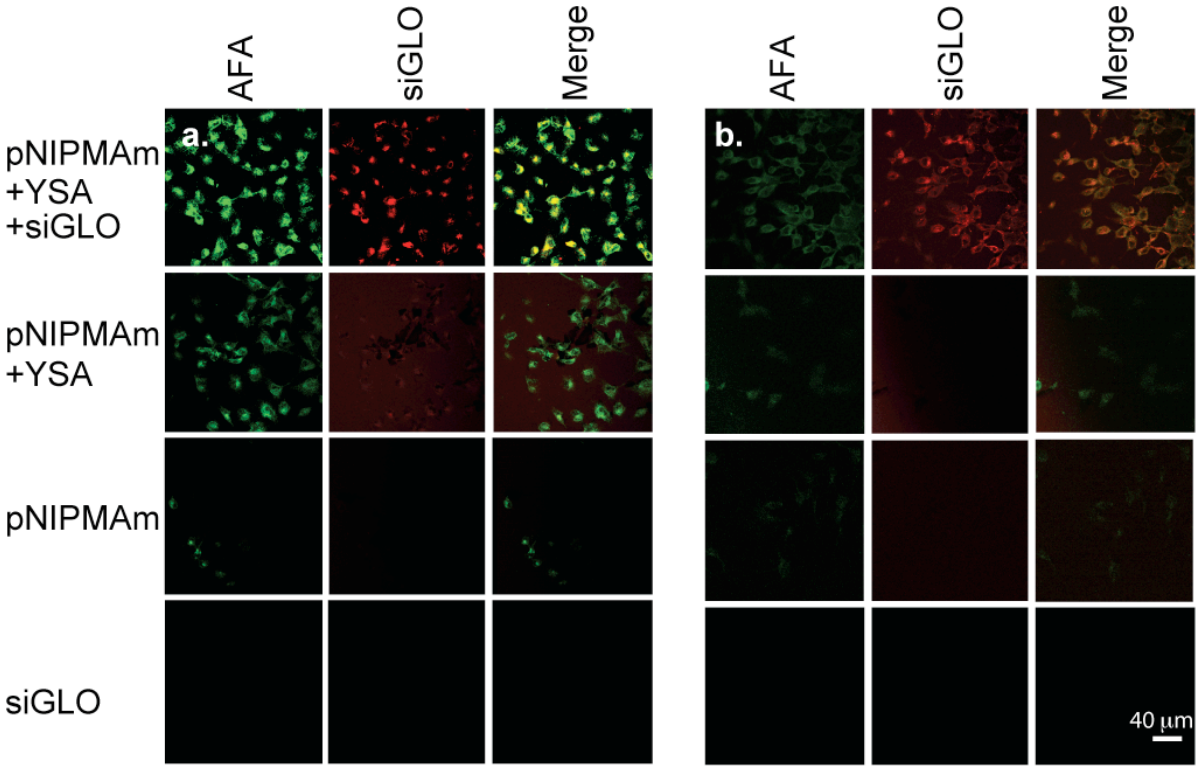

Figure 3.2 Confocal microscopy images of (a) Hey cells and (b) BG-1 cells following exposure to siGLO-loaded/YSA-conjugated pNIPAMAm nanogels, YSA-nanogels alone, unlabeled nanogels, and siGLO alone. The AFA and siGLO fluorescence channels are shown individually, along with a merge of the two channels. Scale bar = 40 µm.

At this time point, siGLO was retained at high levels within the internalized nanogels as indicated by the cell-localized red fluorescence. Merging of the two fluorescence channels showed strong overlap, further indicating delivery of the siGLO by the nanogels into the Hey cells. Hey cells incubated with YSA-targeted but unloaded nanogels showed strong green fluorescence, indicating cell uptake. A small amount of non-targeted uptake was observed for nanogels lacking the YSA peptide. Note that it was extremely difficult to find evidence of nonspecific uptake, and the fluorescence shown in the figure represents the appearance of the rare uptake event observed, and does not represent the overall fluorescence from the entire population of cells. When Hey cells were incubated with siGLO alone, no cell-localized red fluorescence was detected; this is

expected since RNA does not easily permeate the cell membrane in the absence of a carrier vehicle.[16-17]

Targeting experiments were also performed using low EphA2 expressing BG-1 cells (**Figure 3.2**). Decreased levels of green fluorescence were observed in BG-1 cells when compared to the fluorescence observed in the Hey cell cultures. The lower amount of nanogel uptake by the BG-1 cells was most likely due to the reduced EphA2 receptor expression; we have demonstrated a ~2.5-fold difference in EphA2 expression levels between these two cell lines. Control studies using non-targeted pNIPMAm nanogels or siGLO only showed no fluorescence in either the green or red fluorescent channels. These results indicate that the YSA peptide imparts targeting properties to the nanogels in the case of both the high (Hey) and low (BG-1) EphA2 expressing cells, and that the amount of nanogel uptake was dependent upon the level of EphA2 receptor expression. These results also indicate that nonspecific or nontargeted uptake of nanogels by cultured cells is low, and that the siRNA is unable to penetrate the cell membrane in the absence of a carrier vehicle. Together, these initial results illustrate the promise of the targeted nanogel construct for targeted delivery of oligonucleotide cargo.

To further establish the mechanism of nanogel targeting and uptake, we took advantage of the known receptor internalization properties of the EphA2 receptor. Specifically, it has been shown that binding of ephrin-A1, a ligand for EphA2, to EphA2 receptor causes internalization and degradation of the receptor-ligand complex.[51] Figure 3.3 shows the results of studies wherein this receptor recycling process was used to establish the nanogel target by preincubating Hey cells with ephrin-A1 before YSA-targeted nanogel incubation. We hypothesized that if uptake of nanogels is EphA2 receptor-mediated, YSA-targeted uptake after cell exposure to ephrin-A1 should be reduced, as the EphA2 receptor will be internalized and less available for binding to the nanogels. Hey cells were incubated overnight in an 8-well chamber slide. Two μg of ephrin-A1 were added, and the cells were incubated for 1 hour at 37 ºC. After ephrin-A1

incubation, siGLO-loaded/YSA-conjugated nanogels were added to both ephrin-A1 and control (PBS) treated wells. The cells were incubated for four hours, washed, and processed for imaging.

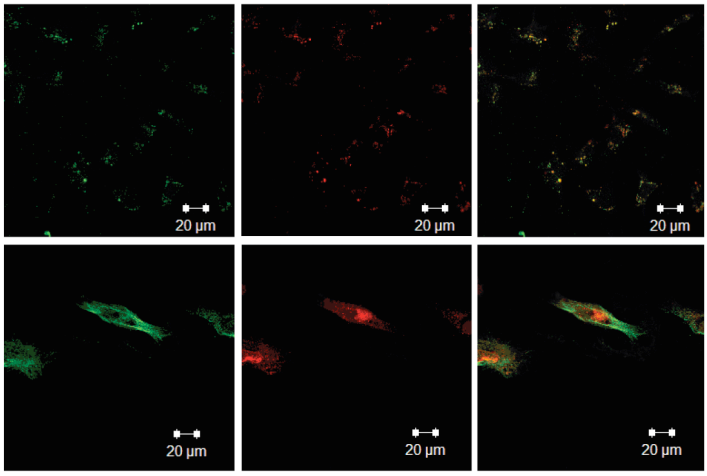

Figure 3.3 Confocal microscopy images of Hey cells (top) following exposure to siGLO-loaded/YSA-conjugated nanogels after 1 h ephrin incubation, and (bottom) following exposure to siGLO-loaded/YSA-conjugated nanogels alone. The fluorescence channels shown are as in Figure 3.2. Scale bar = 20 µm.

Figure 3.3 shows the nanogel uptake in Hey cells preincubated with ephrin-A1. Whereas these cells (top three panels) show some uptake of nanogels and encapsulated siGLO, the amount of uptake is greatly diminished compared with untreated cells (lower three panels). These results suggest that YSA-conjugated uptake by Hey cells is conducted to a large extent through EphA2, however, a small amount of uptake may occur through nonspecific mechanisms or via binding of YSA to other Eph receptors.[35] This is not surprising, given the fact that ephrin and various small molecule ephrin mimics display binding affinities for multiple receptors of the Eph family.[52-53] Flow cytometry was also used to establish the EphA2-associated binding of the peptide-targeted nanogels. In this case, a scrambled (SCR) peptide sequence (DYPSMAMYSPSVC) possessing the same amino acid composition of the YSA peptide was tethered to the nanogels. The resultant nanogels should therefore possess the same

physicochemical surface properties as the YSA-labeled nanogels, but should not specifically bind to the EphA2 receptor.

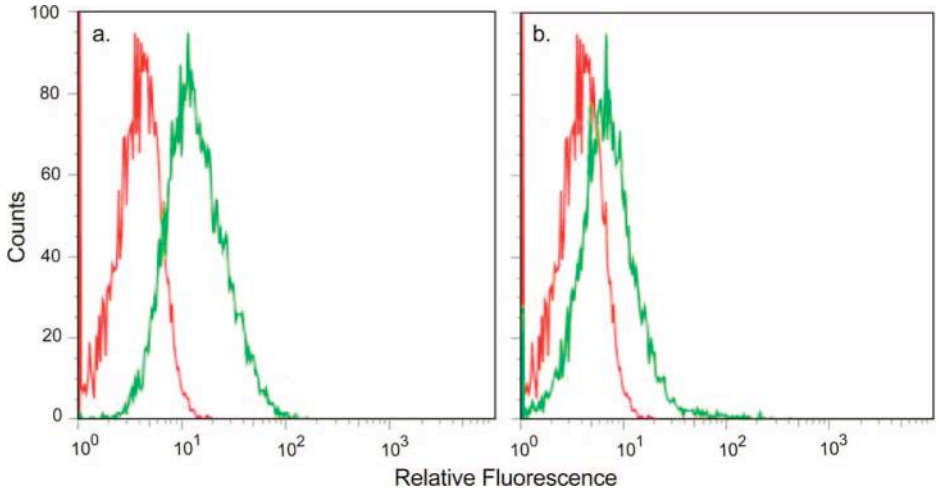

Figure 3.4 Flow cytometry data comparing (a) cell autofluorescence (red) vs. cells incubated with YSA-pNIPMAm nanogels (green) and (b) cell autofluorescence (red) vs. cells incubated with SCR-pNIPMAm nanogels (green). The differential uptake between the YSA- and SCR- labeled nanogels indicates the Eph2A receptor-specific binding and uptake pathway.

Figure 3.4 shows the results of these studies, where cells incubated with YSA-labeled nanogels display ~10-fold greater fluorescence relative to those incubated with SCR-labeled nanogels. Furthermore, the fluorescence signal associated with cells incubated with SCR-labeled nanogels is only slightly greater than the cell autofluorescence background signal.

The effect of nanogels on tumor cell toxicity and proliferation was examined using two cell viability assays. For the trypan blue exclusion assay, Hey cells were incubated with pNIPMAm nanogels, YSA-conjugated nanogels, or SCR-conjugated nanogels for 72 hours. The cells were then washed with PBS, and trypan blue was added to the cells. Five fields were observed via microscopy for each treatment group. Blue cells, indicating dead cells, were not observed in any of the fields examined for any of the treatment groups. To more precisely establish any negative effects associated with nanogel-based delivery, we used the Tox 8 viability proliferation assay. Hey cells were

incubated in 96-well plates overnight and nanogels delivered and removed via the usual method. In the gene silencing data shown below, we chose siRNA targeting epidermal growth factor receptor (EGFR); knockdown of this receptor is non-lethal, but has clinical relevance in the treatment of drug resistant ovarian carcinomas.[54] This siRNA was therefore used in these toxicity studies, as well. Again, we maintained a ratio of 1 mg nanogels/5 × 10^5 cells for all samples. For the EGFR siRNA-loaded nanogels, this corresponds to 16.6 μg siRNA/5 × 10^5 cells. Wells were washed with PBS, and 100 μL of cell culture medium was added to the wells. After 72 hours, Tox 8 was added to the cells according to the manufacturer's instructions, and the cell viability was determined spectrophotometrically.

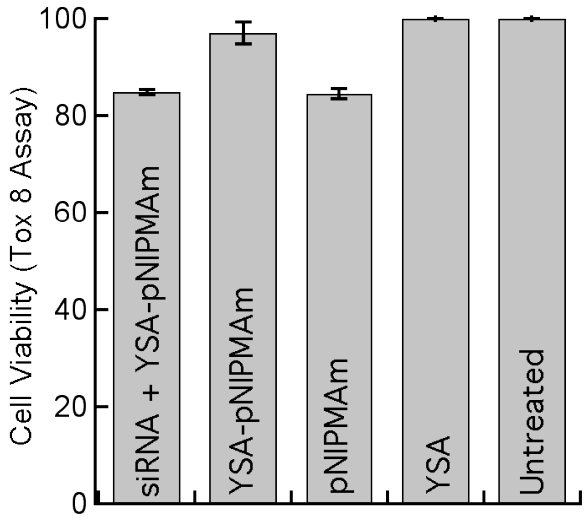

Figure 3.5. Cell viability as determined with a Tox 8 assay for untreated Hey cells and Hey cells following a four h incubation with EGFR siRNA-loaded YSA-labeled nanogels, YSA-labeled pNIPMAm nanogels, unlabeled pNIPMAm, or YSA peptide alone. Error bars represent ±one standard deviation about the average value (n = 3).

This analysis (**Figure 3.5**) revealed no significant difference for any treatment when compared with control (untreated) cells, although exposure to non-targeted nanogels and siRNA-containing nanogels showed slight decreases in viability; the origin of this effect is currently under investigation. These results indicate that treatment of Hey

cells with targeted nanogels does not greatly inhibit cell proliferation, indicating limited toxicity of the nanogels under these conditions.

These promising preliminary studies clearly illustrate the efficacy of peptide-targeted delivery of siRNA cargos via nanogel carriers. The lack of toxicity observed is of particular interest, given the high toxicity observed for some cationic lipid-based siRNA targeting methods, which limits the maximum doses that can be delivered, and also compromises the potential for *in vivo* delivery. In the present studies, a ratio of 16 μg siRNA or 1 mg nanogels/5×10^5 cells was used throughout without significant toxicity being observed. These concentrations are somewhat higher than those suggested for common commercial regents such as RNAiFect (Qiagen) or DharmaFECT (Dharmacon), suggesting that the nanogel approach is capable of delivering siRNA amounts at or above those achievable by optimized commercial reagents. Another complicating factor in current methodologies is the frequent need for cellular delivery under serum free conditions; serum lipids and proteins compromise the stability of many liposomal formulations making their efficacy significantly lower. In the studies described herein, we have illustrated that delivery of siGLO is excellent in serum-containing medium, further establishing the promise of this construct.

As a final preliminary test of the efficacy of the approach, we performed a limited investigation of siRNA-based silencing. Clearly, any delivery approach must deliver *functional* siRNA to the cell interior in order for it to be truly useful. If the nanogel carrier were unable to protect the cargo against degradation in the endosomal or lysosomal compartments, or if the nanogels were unable to escape from endosomes in order to deliver the siRNA to the cytosol, the amount of RNAi would be very low. Thus, we have undertaken a preliminary study of gene silencing to illustrate a minimal requirement for siRNA delivery: the functional silencing of a target mRNA.

As described above, we chose siRNA targeting EGFR; knockdown of this receptor is non-lethal, but has clinical relevance in the treatment of drug resistant ovarian

carcinomas.[54] To determine if we could effectively knockdown EGFR *in vitro*, EGFR siRNA was encapsulated at a concentration of 16.6 μg of EGFR siRNA/mg of nanogels, using the loading technique described above. Nanogels were then added to Hey cells (1 mg of nanogels or 16.6 μg siRNA/5 × 10^5 cells) and incubated at 37 ºC for four hours. The unincorporated nanogels were then removed by washing the cells, and the medium was replaced. Controls included cells incubated with siRNA-loaded but non-targeted pNIPMAm nanogels, unloaded YSA-targeted nanogels, pNIPMAm nanogels, and untreated cells. All cells were harvested at 48 hours and assayed for EGFR expression by immunoblotting, as described in the Experimental Section.

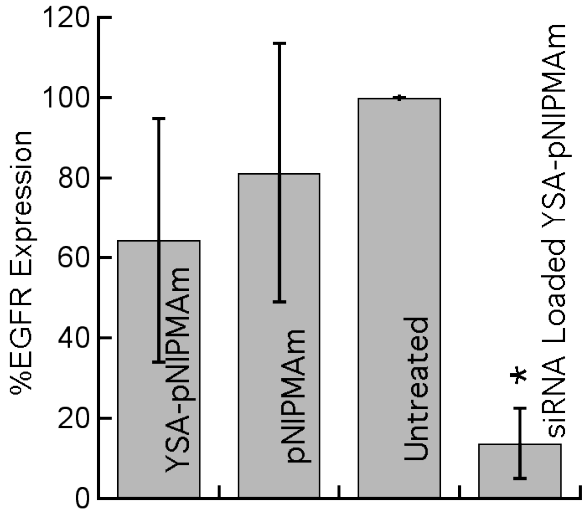

Figure 3.6. EGFR expression, as determined by immunoblot, in Hey cells following a four h incubation with either unloaded YSA-nanogels, unloaded non-targeted nanogels, or siRNA loaded YSA-nanogels. Untreated cells were set at 100% expression. All cells were harvested 48 h after removal of the nanogels. Error bars represent ±one standard deviation about the average value (n = 3, *p<0.01 relative to untreated sample).

Figure 3.6. shows the results of this experiment; a significant reduction in EGFR expression is observed under these conditions relative to all controls ($p<0.01$ relative to untreated sample by paired t-test, n=3). A small, statistically insignificant decrease in EGFR expression was noted in the unloaded, YSA-targeted nanogel control ($p>0.1$). If this observation is indeed a real one, it may be due to cross talk between the EGFR and

the EphA2 receptors, as described by Larsen and colleagues.[55] In addition, a small decrease in EGFR expression was observed when cells were incubated with pNIPMAm nanogels alone, although the difference is not statistically significant ($p>0.3$) in light of the large observed variability in expression.

These preliminary results illustrate that the targeted nanogels are capable of functional delivery of siRNA to ovarian carcinomas without overt toxic effects, and that the subsequently internalized siRNA is available for gene silencing. Whereas this preliminary demonstration is relatively focused in scope, it clearly shows the promise of the construct.

3.4 Conclusions

Peptide-labeled nanogels with a high loading capacity for siRNA have been developed and can be effectively targeted to ovarian carcinomas by receptor-peptide binding. The encapsulated siRNA is transported into the cell interior, where it is available for gene silencing, as illustrated in this case by EGFR knockdown. Since the locus of siRNA-mediated gene silencing is the cytosol, the results are suggestive of the surprising conclusion that endosomal uptake of the nanogels is followed by endosomal escape, resulting in efficient transport/release of the siRNA to the cytosol. Whereas we do not currently know the exact mechanism by which endosomal escape occurs. It is plausible that the nanogels respond to endosomal changes in osmotic pressure and ionic strength by undergoing a volume change. This phenomenon, called osmotic swelling/deswelling[56] is fundamental to the phase behavior of gel networks and may serendipitously be responsible for the excellent delivery properties described above. In addition to the gene-silencing efficacy, the nanocarriers are demonstrated to be non-toxic under the conditions investigated and are effective even when delivered in serum-containing medium. As a result of these studies, we are currently investigating the fundamental mechanisms of nanogel endosomal release. Additionally, the gene silencing results are being validated in

a broader study of RNAi with plans to extend their use to *in vivo* delivery and silencing in animal models.

3.5 Researcher Contributions

Multiple researchers contributed to this work. The original conception of the study occurred prior to my entry into the research program by Dr. Erin B. Dickerson, Dr. William H. Blackburn, Dr. John F. McDonald, and Dr. L. Andrew Lyon. Dr. Blackburn, Dr. Dickerson, and myself designed and executed the experiments. After the graduation of Dr. Blackburn, I synthesized and characterized all nanogels used in these experiments. All authors contributed to and approved the final manuscript.

3.6 References

1. Saad, M.; Garbuzenko, O. B.; Ber, E.; Chandna, P.; Khandare, J. J.; Pozharov, V. P.; Minko, T., Receptor targeted polymers, dendrimers, liposomes: Which nanocarrier is the most efficient for tumor-specific treatment and imaging? *J. Control. Release* **2008,** *130* (2), 107-114.

2. LaVan, D. A.; McGuire, T.; Langer, R., Small-scale systems for in vivo drug delivery. *Nat. Biotechnol.* **2003,** *21* (10), 1184-1191.

3. Moses, M. A.; Brem, H.; Langer, R., Advancing the field of drug delivery: Taking aim at cancer. *Cancer Cell* **2003,** *4* (5), 337-341.

4. Derfus, A. M.; Chen, A. A.; Min, D. H.; Ruoslahti, E.; Bhatia, S. N., Targeted quantum dot conjugates for siRNA delivery. *Bioconjug. Chem.* **2007,** *18* (5), 1391-6.

5. Lee, S. H.; Bae, K. H.; Kim, S. H.; Lee, K. R.; Park, T. G., Amine-functionalized gold nanoparticles as non-cytotoxic and efficient intracellular siRNA delivery carriers. *Int. J. Pharm.* **2008,** *364* (1), 94-101.

6. Kim, S.; Jeong, J. H.; Lee, S. H.; Kim, S.; Park, T. G., LHRH Receptor-Mediated Delivery of siRNA Using Polyelectrolyte Complex Micelles Self-Assembled from siRNA-PEG-LHRH Conjugate and PEI. *Bioconjug. Chem.* **2008,** *19*, 2156-2162.

7. Eavarone, D. A.; Yu, X.; Bellamkonda, R. V., Targeted drug delivery to C6 glioma by transferrin-coupled liposomes. *J. Biomed. Mater.* **2000,** *51* (1), 10-14.

8. Lee, R. J.; Low, P. S., Delivery of liposomes into cultured KB cells via folate receptor-mediated endocytosis. *J. Biol. Chem.* **1994,** *269* (5), 3198-204.

9. van Nostrum, C. F., Polymeric micelles to deliver photosensitizers for photodynamic therapy. *Adv. Drug Delivery Rev.* **2004,** *56* (1), 9-16.

10. Zhang, K.; Fang, H.; Wang, Z.; Taylor, J. S.; Wooley, K. L., Cationic shell-crosslinked knedel-like nanoparticles for highly efficient gene and oligonucleotide transfection of mammalian cells. *Biomaterials* **2008**.

11. Sun, T. M.; Du, J. Z.; Yan, L. F.; Mao, H. Q.; Wang, J., Self-assembled biodegradable micellar nanoparticles of amphiphilic and cationic block copolymer for siRNA delivery. *Biomaterials* **2008,** *29* (32), 4348-55.

12. Mao, H. Q.; Leong, K. W., Design of polyphosphoester-DNA nanoparticles for non-viral gene delivery. *Adv. Genet.* **2005,** *53*, 275-306.

13. Vinogradov, S. V., Colloidal microgels in drug delivery applications. *Curr. Pharm. Des.* **2006,** *12* (36), 4703-4712.

14. Cheng, J.; Teply Benjamin, A.; Sherifi, I.; Sung, J.; Luther, G.; Gu Frank, X.; Levy-Nissenbaum, E.; Radovic-Moreno Aleksandar, F.; Langer, R.; Farokhzad Omid, C., Formulation of functionalized PLGA-PEG nanoparticles for in vivo targeted drug delivery. *Biomaterials* **2007,** *28* (5), 869-76.

15. Das, M.; Mardyani, S.; Chan, W. C. W.; Kumacheva, E., Biofunctionalized pH-responsive microgels for cancer cell targeting: Rational design. *Adv. Mater. (Weinheim, Ger.)* **2006,** *18* (1), 80-83.

16. Akhtar, S.; Benter, I. F., Nonviral Delivery of synthetic siRNAs in vivo. *J. Clin. Invest.* **2007,** *117*, 3623-3632.

17. Sepp-Lorenzino, L.; Ruddy, M., Challenges and opportunities for local and systemic delivery of siRNA and antisense oligonucleotides. In *Clin. Pharmacol. Ther.*, 2008; Vol. 84, pp 628-32.

18. Martinez, J.; Patkaniowska, A.; Urlaub, H.; Luhrmann, R.; Tuschl, T., Single-stranded antisense siRNAs guide target RNA cleavage in RNAi. *Cell* **2002,** *110* (5), 563-74.

19. Spagnou, S.; Miller, A. D.; Keller, M., Lipidic carriers of siRNA: Differences in the formulation, cellular uptake, and delivery with plasmid DNA. *Biochemistry (Mosc.)* **2004,** *43*, 13348-13356.

20. Jeong, J. H.; Mok, H.; Oh, Y. K.; Park, T. G., siRNA Conjugate Delivery Systems. *Bioconjug. Chem.* **2008,** *DOI 10.1021/bc800278e*, published online 2008/12/05.

21. Schiffelers, R. M.; Ansari, A.; Xu, J.; Zhou, Q.; Tang, Q. Q.; Storm, G.; Molema, G.; Lu, P. Y.; Scaria, P. V.; Woodle, M. C., Cancer siRNA therapy by tumor selective delivery with ligand-targeted sterically stabilized nanoparticle. *Nucleic Acids Res.* **2004,** *32* (19).

22. Song, E.; Zhu, P.; Lee, S.-K.; Chowdhury, D.; Kussman, S.; Dykxhoorn, D. M.; Feng, Y.; Palliser, D.; Weiner, D. B.; Shankar, P.; Marasco, W. A.; Lieberman, J., Antibody mediated in vivo delivery of small interfering RNAs via cell-surface receptors. *Nat. Biotechnol.* **2005,** *23* (6), 709-717.

23. Pirollo, K. F.; Rait, A.; Zhou, Q.; Hwang, S. H.; Dagata, J. A.; Zon, G.; Hogrefe, R. I.; Palchik, G.; Chang, E. H., Materializing the Potential of Small Interfering RNA via a Tumor-Targeting Nanodelivery System. *Cancer Res.* **2007,** *67* (7), 2938-2943.

24. Mok, H.; Park, T. G., Self-crosslinked and reducible fusogenic peptides for intracellular delivery of siRNA. *Biopolymers* **2008,** *89* (10), 881-8.

25. Juliano, R. L., Peptide-oligonucleotide conjugates for the delivery of antisense and siRNA. *Curr. Opin. Mol. Ther.* **2005,** *7* (2), 132-136.

26. Kang, H. M.; DeLong, R.; Fisher, M. H.; Juliano, R. L., Tat-conjugated PAMAM dendrimers as delivery agents for antisense and siRNA oligonucleotides. *Pharm. Res.* **2005,** *22* (12), 2099-2106.

27. Simeoni, F.; Morris, M. C.; Heitz, F.; Divita, G., Insight into the mechanism of the peptide-based gene delivery system MPG: implications for delivery of siRNA into mammalian cells. *Nucleic Acids Res.* **2003,** *31* (11), 2717-2724.

28. Zatsepin, T. S.; Turner, J. J.; Oretskaya, T. S.; Gait, M. J., Conjugates of oligonucleotides and analogues with cell penetrating peptides as gene silencing agents. *Curr. Pharm. Des.* **2005,** *11* (28), 3639-3654.

29. Zhang, C. L.; Tang, N.; Liu, X. J.; Liang, W.; Xu, W.; Torchilin, V. P., siRNA-containing liposomes modified with polyarginine effectively silence the targeted gene. *J. Control. Release* **2006,** *112* (2), 229-239.

30. Nayak, S.; Lee, H.; Chmielewski, J.; Lyon, L. A., Folate-Mediated Cell Targeting and Cytotoxicity Using Thermoresponsive Microgels. *J. Am. Chem. Soc.* **2004,** *126* (33), 10258-10259.

31. Shin, Y.; Chang, J. H.; Liu, J.; Williford, R.; Shin, Y. K.; Exarhos, G. J., Hybrid nanogels for sustainable positive thermosensitive drug release. *J. Control. Release* **2001,** *73* (1), 1-6.

32. Blackburn, W. H.; Lyon, L. A., Size-controlled synthesis of monodisperse core/shell nanogels. *Colloid Polym. Sci.* **2008,** *286* (5), 563-569.

33. Berndt, I.; Popescu, C.; Wortmann, F.-J.; Richtering, W., Mechanics versus thermodynamics: swelling in multiple-temperature-sensitive core-shell microgels. *Angew. Chem., Int. Ed.* **2006,** *45* (7), 1081-1085.

34. Jones, C. D.; Lyon, L. A., Synthesis and Characterization of Multiresponsive Core-Shell Microgels. *Macromolecules* **2000,** *33*, 8301-8306.

35. Koolpe, M.; Dail, M.; Pasquale, E. B., An ephrin mimetic peptide that selectively targets the EphA2 receptor. *J. Biol. Chem.* **2002,** *277* (49), 46974-9.

36. Lin, Y. G.; Han, L. Y.; Kamat, A. A.; Merritt, W. M.; Landen, C. N.; Deavers, M. T.; Fletcher, M. S.; Urbauer, D. L.; Kinch, M. S.; Sood, A. K., EphA2 overexpression is associated with angiogenesis in ovarian cancer. *Cancer* **2007,** *109* (2), 332-40.

37. Brantley-Sieders, D. M.; Fang, W. B.; Hicks, D. J.; Zhuang, G.; Shyr, Y.; Chen, J., Impaired tumor microenvironment in EphA2-deficient mice inhibits tumor angiogenesis and metastatic progression. *FASEB J.* **2005,** *19* (13), 1884-6.

38. Han, L.; Dong, Z.; Qiao, Y.; Kristensen, G. B.; Holm, R.; Nesland, J. M.; Suo, Z., The clinical significance of EphA2 and Ephrin A-1 in epithelial ovarian carcinomas. *Gynecol. Oncol.* **2005,** *99* (2), 278-86.

39. Thaker, P. H.; Deavers, M.; Celestino, J.; Thornton, A.; Fletcher, M. S.; Landen, C. N.; Kinch, M. S.; Kiener, P. A.; Sood, A. K., EphA2 expression is associated with aggressive features in ovarian carcinoma. *Clin. Cancer Res.* **2004,** *10* (15), 5145-50.

40. Walker-Daniels, J.; Coffman, K.; Azimi, M.; Rhim, J. S.; Bostwick, D. G.; Snyder, P.; Kerns, B. J.; Waters, D. J.; Kinch, M. S., Overexpression of the EphA2 tyrosine kinase in prostate cancer. *Prostate* **1999,** *41* (4), 275-80.

41. Zeng, G.; Hu, Z.; Kinch, M. S.; Pan, C. X.; Flockhart, D. A.; Kao, C.; Gardner, T. A.; Zhang, S.; Li, L.; Baldridge, L. A.; Koch, M. O.; Ulbright, T. M.; Eble, J. N.; Cheng, L., High-level expression of EphA2 receptor tyrosine kinase in prostatic intraepithelial neoplasia. *Am. J. Pathol.* **2003,** *163* (6), 2271-6.

42. Ogawa, K.; Pasqualini, R.; Lindberg, R. A.; Kain, R.; Freeman, A. L.; Pasquale, E. B., The ephrin-A1 ligand and its receptor, EphA2, are expressed during tumor neovascularization. *Oncogene* **2000,** *19* (52), 6043-52.

43. Zelinski, D. P.; Zantek, N. D.; Stewart, J. C.; Irizarry, A. R.; Kinch, M. S., EphA2 overexpression causes tumorigenesis of mammary epithelial cells. *Cancer Res.* **2001,** *61* (5), 2301-6.

44. Kataoka, H.; Igarashi, H.; Kanamori, M.; Ihara, M.; Wang, J. D.; Wang, Y. J.; Li, Z. Y.; Shimamura, T.; Kobayashi, T.; Maruyama, K.; Nakamura, T.; Arai, H.; Kajimura, M.; Hanai, H.; Tanaka, M.; Sugimura, H., Correlation of EPHA2 overexpression with high microvessel count in human primary colorectal cancer. *Cancer Sci.* **2004,** *95* (2), 136-41.

45. Saito, T.; Masuda, N.; Miyazaki, T.; Kanoh, K.; Suzuki, H.; Shimura, T.; Asao, T.; Kuwano, H., Expression of EphA2 and E-cadherin in colorectal cancer: correlation with cancer metastasis. *Oncol. Rep.* **2004,** *11* (3), 605-11.

46. Clark, K. D.; Volkman, B. F.; Thoetkiattikul, H.; King, D.; Hayakawa, Y.; Strand, M. R., Alanine-scanning mutagenesis of plasmatocyte spreading peptide identifies critical residues for biological activity. *J. Biol. Chem.* **2001,** *276* (21), 18491-6.

47. Hermanson, G. T., *Bioconjugate Techniques*. 1st ed.; Academic Press: San Diego, 1996; Vol. 1, p 786.

48. Betancourt, T.; Shah, K.; Brannon-Peppas, L., Rhodamine-loaded poly(lactic-co-glycolic acid) nanoparticles for investigation of in vitro interactions with breast cancer cells. *J. Mater. Sci.: Mater. Med.* **2009,** *20* (1), 387-395.

49. Maeda, H., The enhanced permeability and retention (EPR) effect in tumor vasculature: The key role of tumor-selective macromolecular drug targeting. *Adv. Enzyme Regul.* **2001,** *41*, 189-207.

50. Scarberry, K. E.; Dickerson, E. B.; McDonald, J. F.; Zhang, Z. J., Magnetic nanoparticle-peptide conjugates for in vitro and in vivo targeting and extraction of cancer cells. *J. Am. Chem. Soc.* **2008,** *130* (31), 10258-10262.

51. Miao, H.; Burnett, E.; Kinch, M.; Simon, E.; Wang, B., Activation of EphA2 kinase suppresses integrin function and causes focal-adhesion-kinase dephosphorylation. *Nat. Cell Biol.* **2000,** *2* (2), 62-9.

52. Noberini, R.; Koolpe, M.; Peddibhotla, S.; Dahl, R.; Su, Y.; Cosford, N. D.; Roth, G. P.; Pasquale, E. B., Small molecules can selectively inhibit ephrin binding to the EphA4 and EphA2 receptors. *J. Biol. Chem.* **2008,** *283* (43), 29461-72.

53. Surawska, H.; Ma, P. C.; Salgia, R., The role of ephrins and Eph receptors in cancer. *Cytokine Growth Factor Rev.* **2004,** *15* (6), 419-33.

54. Thaker, P. H.; Yazici, S.; Nilsson, M. B.; Yokoi, K.; Tsan, R. Z.; He, J.; Kim, S. J.; Fidler, I. J.; Sood, A. K., Antivascular therapy for orthotopic human ovarian carcinoma through blockade of the vascular endothelial growth factor and epidermal growth factor receptors. *Clin. Cancer Res.* **2005,** *11* (13), 4923-33.

55. Larsen, A. B.; Pedersen, M. W.; Stockhausen, M. T.; Grandal, M. V.; van Deurs, B.; Poulsen, H. S., Activation of the EGFR gene target EphA2 inhibits epidermal growth factor-induced cancer cell motility. *Mol. Cancer Res.* **2007,** *5* (3), 283-93.

56. Saunders, B. R.; Vincent, B., Osmotic deswelling of microgel particles in the presence of free polymer. *Prog. Colloid Polym. Sci.* **1997,** *105* (Trends in Colloid and Interface Science XI), 11-15.

CHAPTER 4

THE EROSION OF HYDROLYTICALLY-DEGRADABLE NANOGELS VIA MULTIANGLE LIGHT SCATTERING COUPLED TO ASYMMETRICAL FLOW FIELD-FLOW FRACTIONATION

Adapted from

Smith MH, South AB, Gaulding JC, Lyon LA. *Anal. Chem.,* 2010, 82, (2), 523–530.

4.1. Introduction

Nanogels were described in previous chapters as a unique class of drug delivery vehicles that may be applicable as injectable formulations. For example, nanogels are well-hydrated,[1] have demonstrated non-fouling characteristics in serum,[2-3] and are capable of encapsulating, retaining, and releasing macromolecules from their porous polymer network.[4-8] By assisting in the intravenous transport, accumulation, and uptake by malignant cells, the therapeutic efficacy of drugs may be improved. Furthermore, the toxic side-effects commonly observed in most chemotherapy treatments may be reduced or eliminated by avoiding accumulation in healthy tissues.

Chapter 3 discussed the efficient and functional delivery of macromolecular therapeutics (small interfering RNA, siRNA) to ovarian cancer cells.[9] Nanogels composed of poly(*N*-isopropylmethacrylamide) (pNIPMAm) were demonstrated in that work to be non-toxic and able to efficiently encapsulate, retain and deliver functional siRNA upon uptake by cancer cells. However, bioaccumulation and nonspecific organ filtration is a concern for colloids designed for intravenous delivery. Degradation into lower molecular weight components may improve clearance by renal filtration, and

reduce undesired accumulation within the patient. Renal clearance is considered the most efficient route of nanoparticle excretion, in comparison to liver sequestration and subsequent reticuloendothelial macrophage uptake and hepatobiliary excretion into the intestine.[10] In addition to clearance, erosion behavior may modulate the release of encapsulated drugs through network decomposition.[11]

The design of erodible, responsive nanogels is a challenging task, wherein stimulus-sensitivity and degradability are sought simultaneously in the same particle architecture. Although a variety of erodible polymer colloids have been investigated, including lactic and glycolic-acid based polymers,[12-13] poly(cyanoacrylate) (PCA),[14] poly(ε-caprolactone) (PCL),[15] and poly(alkylcyanoacrylate) (PACA),[16] we and others have found cross-link scission to be a successful strategy for making erodible poly(alkylacrylamide) nanogels.[17-18] We hypothesized that incorporation of a degradable cross-linker, such as *N,O*-(dimethacryloyl)hydroxylamine (DMHA), would result in degradable nanogels *via* cross-link cleavage. The DMHA cross-linker has been successfully applied in multiple hydrogel biomaterials, including degradable embryonic stem-cell supports,[19] *in vitro* and *in vivo* drug release devices,[20-21] and polymer scaffolds in spinal cord regeneration.[22] Incorporation of DMHA is an attractive approach since the cross-linker is stable in acidic environments (pH < 5), is easy to synthesize, decomposes under physiological conditions, and has low *in vivo* toxicity.[22]

Polymer degradation is likely to induce changes in colloidal properties. Thus, methods to monitor particle behavior during the erosion process are critical in the design of injectable nanogels. These measurements must be made in complex mixtures (e.g. in the presence of degradation products or in the presence of serum components) while assessing multiple colloidal properties (size, molar mass, number density) in solution. To accomplish these goals, we have developed methods using asymmetrical flow field-flow fractionation separation (A4F), coupled with multiangle light scattering detection and differential refractometry (A4F/MALS/dRI). A4F is a one-phase, non-destructive

separation technique that permits the separation of a wide range of polymer sizes and molar masses.[23-25] The method is particularly enabling when coupled on-line to characterization tools such as MALS and dRI, which allows the determination of the M_w, the r_{rms}, and the distribution of these values within the sample without the need to calibrate against standards (a detailed description of A4F/MALS is provided in Chapter 2). Together, these coupled methods permit the separation of complex colloid/polymer mixtures, followed by direct determination of particle size, molar mass, and when further combined with additional tools such as dynamic light scattering, morphological characterization.

As described in Chapter 2, A4F/MALS has been a particularly enabling technique in the measurement of r_{rms} distributions for hydrogel nanoparticles (nanogels).[26] This stationary phase-free system allows rapid separations without the application of destructive shear forces observed in more traditional chromatographic systems. Through a separation technique like A4F, light scattering analysis on complex samples may be performed since impurities may be separated, thereby providing interpretable MALS data. Additionally, eluting particles may be recovered in a fractionated manner for subsequent analysis. In this investigation, we demonstrate an A4F/MALS/dRI method to monitor the erosion of pNIPMAm-DMHA nanogels, where multiple colloidal properties can be monitored throughout the degradation reaction, providing insight into the erosion process.

4.2 Experimental Section

4.2.1 Materials

All reagents were purchased from Sigma-Aldrich (St Louis, MO) and used as received, unless otherwise noted. The monomer *N*-isopropylmethacrylamide (NIPMAm) was twice recrystallized from hexanes (VWR international, West Chester, PA) and dried

in vacuo prior to use. Reagents sodium dodecyl sulfate (SDS) and ammonium persulfate (APS) were all used as received. Water used in all reactions, particle purifications, and buffer preparations was purified to a resistance of 18 MΩ (Barnstead E-Pure system), and filtered through a 0.2 μm filter to remove particulate matter.

4.2.2 Nanogel Synthesis

The synthesis of hydrolytically degradable cross-linker was performed as described previously.[21] In brief, DMHA was produced through the reaction of 0.145 moles (10.1 g) of hydroxylamine hydrochloride with 0.243 moles (25.4 g) of methacryloyl chloride in 50 mL of pyridine at 45 °C. After stirring at ambient temperature for 2 hours, the mixture was diluted in 100 mL of chloroform and 21 mL of concentrated hydrochloric acid. The organic layer was separated, washed four times with distilled, deionized water, and dried over $MgSO_4$.[21] The product identity was confirmed by ^1H NMR and elemental analysis.

The synthesis of pNIPMAm-DMHA nanogels was performed by precipitation polymerization. As described in Chapter 1, this synthetic method is an effective means for producing a variety of micro- and nanogel structures.[26-28] The molar composition of reagents was 98% NIPMAm and 2% DMHA, with a total monomer concentration of 140 mM in a 50.0 mL total synthesis volume. First, 0.873 g of NIPMAm was dissolved in 48.0 mL of distilled, deionized water. A mass of 115 mg of SDS was added, resulting in a final SDS concentration of 8 mM. This solution was added to a three-neck round-bottom flask, and allowed to equilibrate to 70 °C while purging with N_2 for an hour. Prior to initiation, the DMHA cross-linker was dissolved in DMSO at a concentration of 0.140 M. A 1.0 mL aliquot of the DMHA solution was delivered to the flask by pipette, and allowed to equilibrate for 10 minutes. The polymerization was initiated by delivering a 1.0 mL aliquot of 0.800 M APS solution by pipette. The reaction was allowed to proceed for 7 hours under an N_2 blanket while continuously stirring. Once cooled, the solution

was vacuum filtered, followed by repeated ultracentrifugation and resuspension in H_2O. Water was removed from the purified product by lyophilization at -42 °C under 40×10^{-3} mbar for 72 hours. The freeze-dried product was a hygroscopic white powder.

4.2.3 Instruments

The r_h of nanogels were measured using DLS. DLS experiments were performed at a 90° scattering angle using a Dynapro DLS (Wyatt Technology Corporation, Santa Barbara, CA). Typical particle concentrations used were ~0.01 wt%. The VPTT of degradable nanogels was assessed from turbidity curves collected on a steady-state fluorescence spectrophotometer (Photon Technology International), equipped with a Model 814 PMT photon-counting detector.

A4F was performed using the Eclipse 1 Separation System (Wyatt Technology Corporation, Santa Barbara, CA). The eluent for all studies was composed of distilled and deionized water with 200 ppm NaN_3 (Ionic strength = 3 mM). The Agilent 1100 Series Isocratic pump (Agilent Technologies) was used for eluent flow, whereas the Eclipse software Version 2.5.3 (Wyatt Technologies) was used for flow control. An Agilent 1100 Series Vacuum degasser (Agilent Technologies, Santa Clara, CA) was equipped between the eluent reservoir and the pump system and an FP Vericel 0.45 μm membrane filter (Gelman Sciences, Ann Arbor, MI) was equipped after the eluent pump system to ensure a dust-free carrier. Similar to other A4F instruments, the channel employed here was trapezoidal in shape.[29] The channel had a total length of 26.5 cm, whereas the channel breadth at the inlet and outlet was 1.5 and 0.5 cm, respectively. The accumulation wall of the channel was equipped with a 10 kDa MWCO regenerated cellulose membrane (Microdyn-Nadir, Germany) with a 350 μm channel spacer. Detection was performed on-line using MALS and dRI detectors.

The MALS photometer was a DAWN-EOS (Wyatt Technology Corporation, Santa Barbara, CA). The DAWN-EOS contains a GaAs laser (λ = 685 nm). The dRI was

a deflection-based Optilab rEX (Wyatt Technology Corporation, Santa Barbara, CA) refractive index detector, operating with an LED light source (λ = 690 nm). Data collection from both detectors and subsequent light scattering analysis was performed using the Astra software Version 5.3.4.14 (Wyatt Technology Corporation, Santa Barbara, CA). Accurate measurement of nanogel M_w required characterization of the *dn/dc*. Differential refractive index analysis was performed in batch mode using the Optilab rEX system. A series of pNIPMAm-DMHA nanogel dilutions were prepared in dust-free vials, which were rinsed sequentially with distilled deionized water, absolute ethanol, and HPLC-grade acetone. Nanogels were resuspended in the separation eluent over a concentration range from 2.5×10^{-6} g/mL to 3.75×10^{-4} g/mL.

Off-line light scattering measurements were performed using the NanoSight LM20 particle tracking analysis system (Nanosight, Ltd., Amesbury, U.K.). The LM20 is a laser light scattering instrument, which allows the direct visualization of nanoparticle scattering by microscopy.[30-31] The LM20 employs a single-mode laser diode (<20 mW, λ = 635 nm) situated to launch a focused beam through a 500 μL sample chamber, with a cell depth of 0.9 mm. The light scattering of particles moving in the laser path was visualized using the LM20 CCD camera through a view window above the sample chamber. Particle motion was recorded for a suitable period of time (i.e. 90 seconds) at a rate of 30 frames per second. Video images of particle movements under Brownian motion were analyzed using the Nanosight NTA Software Version 2.0 (Nanosight, Ltd., Amesbury, U.K.). Individual particle trajectories were interpreted by the software, allowing the determination of particle diffusion coefficients. Nanogel r_h values were determined using the Stokes-Einstein equation.

4.2.4 Nanogel Turbidity

The VPTT of degradable nanogels was assessed from turbidity curves collected on a steady-state fluorescence spectrophotometer, as described in the *Section 4.2.3*. All

turbidity measurements were performed at a particle concentration of 0.016 mg/mL in pH 3.0 formate buffer. Scattering was measured at 600 nm and a temperature ramp was typically set from 25 °C to a maximum of 50 °C for all measurements. A ramp rate of 0.25 °C/min was used, collecting data every 0.1 °C with an integration time of 1 s per data point.

4.2.5 A4F Procedure

Nanogels were separated via A4F in a two-stage separation scheme at ambient laboratory temperature (22 °C). Through this method, particle size and molar mass-distributions were monitored without extensive scattering interference from degradation products. The stages served to first purify and equilibrate nanogels within the eluent, with the particles being later eluted for subsequent characterization. Sample injection was performed in Focus mode for 1 min using a sample injection flow rate of 0.2 mL/min (injection loop volume = 100 µL). The flow direction is reversed during Focus mode, which serves to concentrate the sample towards a narrow region near the injection point. A bypass flow of 1.0 ml/min was administered through the on-line detectors (MALS, dRI) downstream. Following sample focusing, the flow direction was shifted towards the detectors at a flow rate of 1.0 mL/min with a cross flow of 1.0 mL/min. In this first stage, eluent flow is permitted (containing low molar mass degradation products) while nanogel retention was observed. This stage was maintained for 25 minutes to allow nanogel equilibration in the eluent. Nanogels were subsequently eluted in the second stage for detection, using a reduced cross-flow of 0.25 mL/min with a channel flow of 1.0 mL/min. Detected sample peaks were recovered from A4F into dust-free glass vials for off-line light scattering characterization with the LM20 particle tracking system. The A4F channel and injection loop were flushed extensively (2.0 mL/min flow rate for 2 h) between runs to prevent sample artifacts.

4.2.6 Degradation Study Procedure

To study the degradation process, 4 mg of dry nanogel powder was resuspended in pH or temperature-controlled buffers. In an investigation of the degradation pH-dependence, nanogels were resuspended (0.20 mg/mL particle concentration) in either pH 3.4 formate, pH 5.4 2-(*N*-morpholino)ethanesulfonic acid (MES), pH 7.4 phosphate, or pH 8.4 4-(2-hydroxyethyl)piperazine-1-ethanesulfonic acid (HEPES) buffer (all buffers were prepared with a buffer concentration of 0.02 M and ionic strength values < 0.05 M). Prior to nanogel resuspension, all buffers were equilibrated to 37 °C. Resuspended nanogels were maintained at this temperature while continuously shaking. At predetermined time intervals, a 1.0 mL aliquot of the solution was removed and analyzed directly via A4F/MALS. Prior to analysis, all aliquots were allowed to equilibrate to ambient laboratory temperature (22 °C) while shaking. In an investigation of the temperature dependence of degradation, nanogels were resuspended in pH 7.4 phosphate buffer and allowed to equilibrate at 4 °C, 22 °C, 37 °C and 50 °C while continuously shaking. Similar to the pH experiments, 1.0 mL of particles were removed at predetermined time intervals, equilibrated to 22 °C, and analyzed by A4F/MALS.

4.3 Results and Discussion

Macroscopic hydrogels cross-linked with DMHA have been investigated by others as copolymers with *N*-(2-hydroxylpropyl)methacrylamide (HPMA).[21] Polymers containing DMHA demonstrated degradation *in vitro* and *in vivo*, depending on the pH of the microenvironment and other factors. Specifically, these hydrogels degraded more rapidly at pH > 5, with little erosion being observed at lower pH. Additionally, when lower DMHA concentrations were used in synthesis, the erosion rate was shown to increase. In the pursuit of a degradable nanogel construct, we considered this a promising cross-linker due to its ease of copolymerization with acrylamide-based polymers, its

stability under the acidic conditions commonly observed in persulfate-initiated precipitation polymerization, and its degradation under physiologic conditions.

A precipitation polymerization method was developed for production of pNIPMAm-DMHA nanogels, as described in the *Section 4.2.* Through DLS, the average r_h of pNIPMAm-DMHA particles was determined to be 66.4 ± 0.5 nm. The dimensions of purified pNIPMAm-DMHA nanogels were further investigated by A4F/MALS analysis. Through this method, the r_{rms} of particles were determined to be 40 ± 0.4 nm. Polydispersity values determined by both methods were low (P_d < 15%).

The combination of data from DLS and MALS enabled the characterization of nanoparticle topology. As reviewed in Chapter 2, the r_{rms} (also referred to as the gravimetric radius, r_g) is a particle dimension, weighted by the mass distribution about the center of particle mass. When this value is compared to the hydrodynamic radius, structure-sensitive information is obtained.[32] Specifically, nanoparticles that occupy a similar volume in solution may differ drastically in the value of a dimensionless parameter $\rho = r_{rms}/r_h$. Using this ratio, the phase behavior of pNIPAm above and below the LCST has been monitored in terms of chain topology.[33] For chains below the LCST, ρ = ~1.4. This value of ρ is representative of slightly branched or linear chains in solution. However, after undergoing chain collapse at elevated temperature (T > LCST), ρ decreased sharply from 1.4 to 0.54. This value of ρ is indicative of the surface of the globule having a lower density than the center.[33] In contrast, nanogel spheres in the swollen state typically have ρ values of ~0.6-0.85.[34] The pNIPMAm-DMHA nanogels under study here were found to have a ρ value of 0.60 at 20 °C.

4.3.1 Stimuli-Responsivity

To verify conservation of temperature responsivity for pNIPMAm-DMHA nanogels, the VPTT value was measured from turbidity curves collected on a steady-state fluorescence spectrophotometer, as described in the *Section 4.2*. When the temperature-

dependent scattering intensity from a dispersion of pNIPMAm-DMHA particles was measured pH 3.4, a sharp increase in scattering intensity was observed as the solution temperature was raised above 43 ºC.

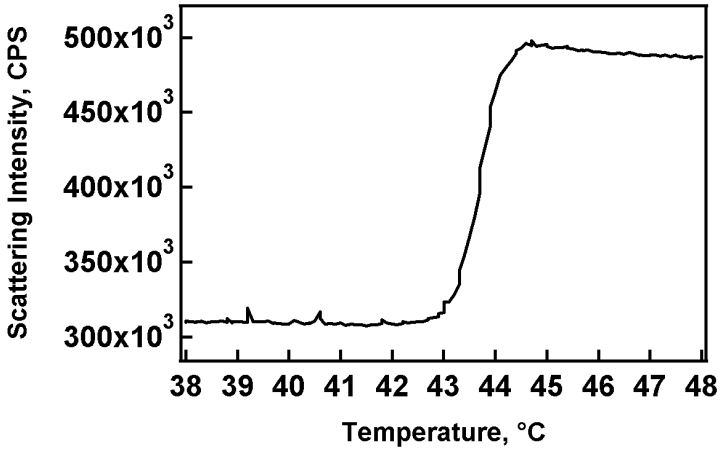

Figure 4.1 Solutions of nanogels display temperature-dependent deswelling. Temperature-dependant turbidity measurements were obtained for pNIPMAm-DMHA degradable nanogels in pH 3.4 buffer.

This scattering intensity increase reflects a change in the hydration state of the polymer. Elevated temperatures above the LCST caused expulsion of solvent from the polymer network, resulting in a deswollen, hydrophobic particle state.[35-37] Particle size above and below the LCST was determined by DLS. At temperatures above the polymer LCST (T > 44 ºC for pNIPMAm), the particle size significantly decreased as the particles assumed a deswollen state (r_h of 45 ± 0.4 nm at 45 °C, pH 3.4).[37] As described earlier, particles equilibrated below this temperature were in a solvent-swollen state, showing a larger hydrodynamic size (r_h of 66.4 ± 0.5 nm at 22 °C, pH 3.4). This VPTT value is in agreement with previously synthesized pNIPMAm-based nanogels,[26] and demonstrates conservation of stimuli-responsive behavior upon DMHA incorporation.

4.3.2 pH-Dependent Erosion

The pH-dependent erosion behavior of nanogels was observed through the A4F/MALS method, monitoring scattering intensity and the angular dependence of scattering as a function of time. Through this approach, the average r_{rms} of particles was determined using the Debye extrapolation method for the construction of the Debye plot.[38] Specifically, the r_{rms} was determined from the slope of the linear fit of the Debye plot. Since the concentration of polymer is constant throughout these experiments, the intensity of scattered light is directly proportional to polymer molar mass. However, initial experiments to monitor erosion were challenging, as angular-dependent fitting of the light scattering is error-prone in the presence of degradation products. To resolve these issues, we employed A4F separation technique to first purify and subsequently elute particles for size distributions and scattering intensity detection. Furthermore, this two-stage separation method was employed to minimized the effects of variable carrier composition on nanogel fractionation, where slight variance in sample pH and osmotic strength may adversely affect polymer elution by altering the eluent environment.[39] As described in the *Section 4.2.*, the first stage of the A4F procedure retained nanogels for 25 minutes at a cross-flow of 1.0 mL/min prior to elution. Equilibration of samples to the eluent environment was evident since t_R values and peak symmetry did not change for nanogels at early time-points (prior to erosion, $t < 1$ hr). This result suggests that nanogels were equilibrated to the carrier composition, and that differences in buffering (pH, osmotic strength) did not significantly affect separations.

To initiate the erosion, pNIPMAm-DMHA nanogels were resuspended in pH-controlled buffers, with pH values ranging from 5.4 – 8.4. Nanogel suspensions displayed dramatic changes in scattering intensity over time when equilibrated at elevated pH. This behavior was observed visually, where samples would become significantly less turbid with reaction time. To more quantitatively investigate the erosion, solutions were monitored by A4F/MALS immediately upon particle resuspension and equilibration. A4F fractograms are shown in Figure 4.2.

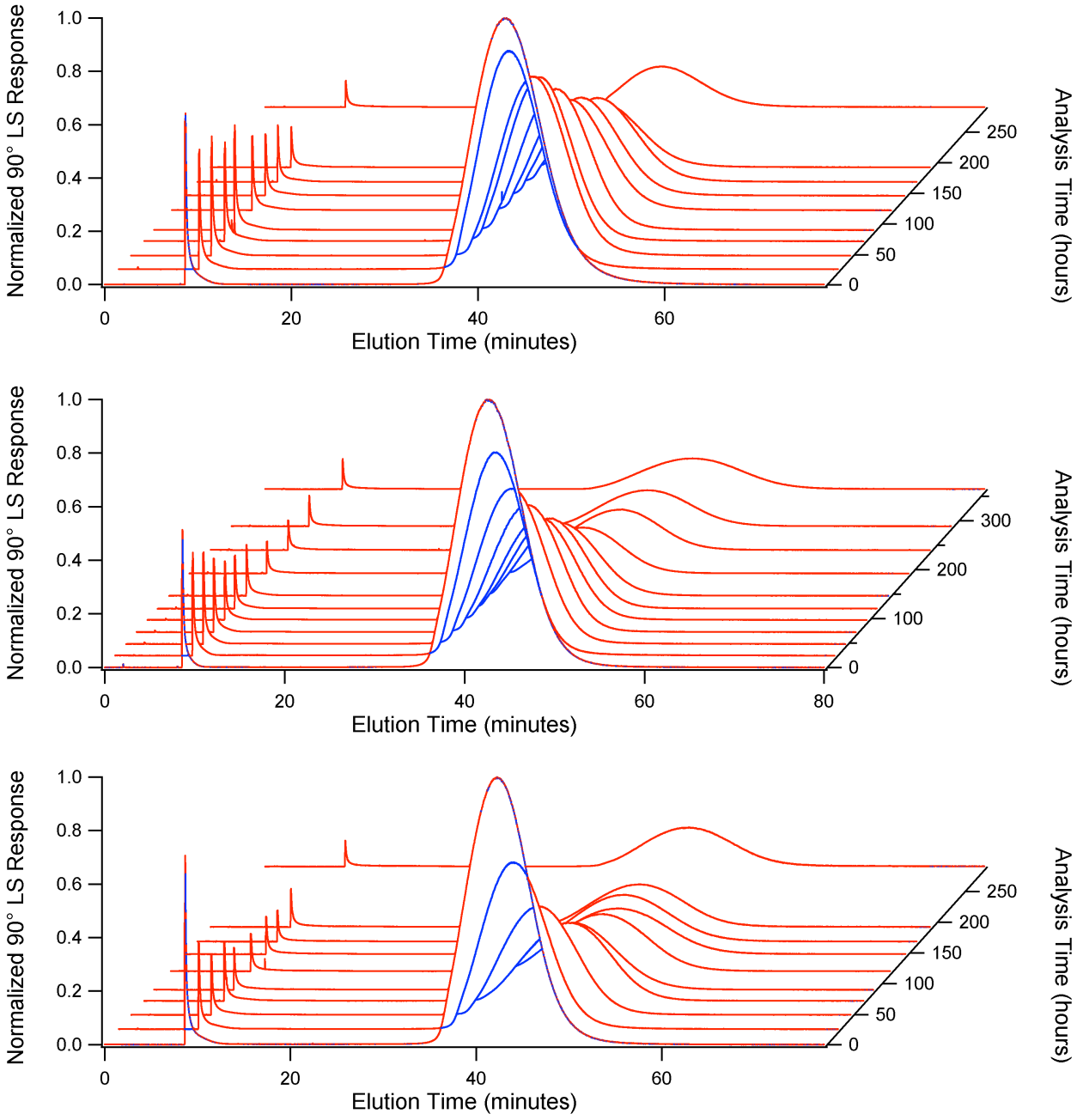

Figure 4.2 A4F fractograms for pH-induced erosion at 37 °C, with light scattering detection at 90°. pH values include pH 5.4 (top), pH 7.4 (middle), and pH 8.4 (bottom).

Typical A4F fractogram peak heights observed throughout the experiments are summarized in **Figure 4.3**, where a decrease in the scattering intensity is evident when the pNIPMAm-DMHA nanogels were incubated at 37 °C and at pH values greater than 3.4.

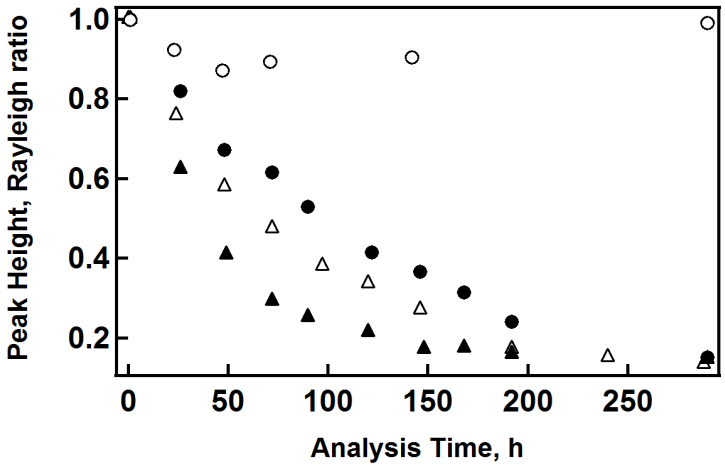

Figure 4.3 Particle erosion results in decreased scattering intensities. Microgels were incubated (37 °C) at pH 3.4 (open circles), pH 5.4 (filled circles), pH 7.4 (open triangles), and pH 8.4 (filled triangles) and the maximum scattering intensity was observed at a scattering angle of 90° as a function of reaction time.

The decrease in the scattered light intensity is primarily indicative of a decrease in the average particle molar mass, but may also be a result of particle number density loss via erosion. Scission of the DMHA cross-linker was expected to induce changes in nanogel dimensions, as the cross-linker content influences polymer chain density within the nanogel and the equilibrium swelling capacity.[40] Using the angular dependence of light scattering, particle r_{rms} values were monitored over the course of the degradation reaction.

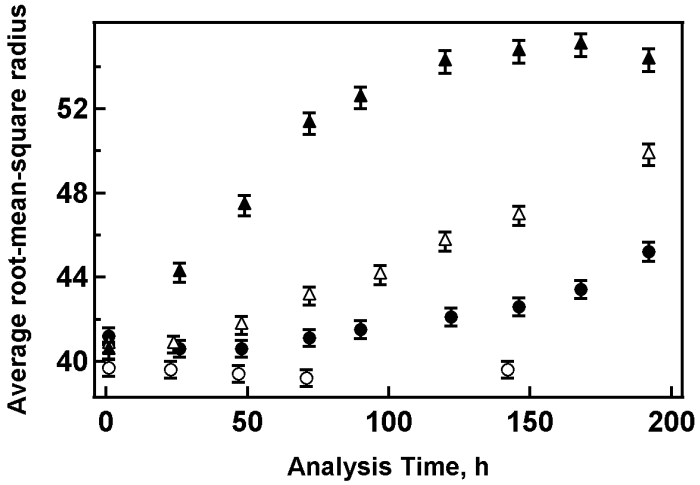

Figure 4.4 DMHA scission results in particle swelling. All r_{rms} data were weight-averaged across all slices, where the size is reported versus reaction time at pH 3.4 (open circles), 5.4 (filled circles), 7.4 (open triangles), and 8.4 (filled triangles). All reactions occurred at 37 °C. Error bars represent the error of the Debye plot polynomial fit of the scattering data, reported across all slices and detectors.

As shown in **Figure 4.4**, the r_{rms} of particles increased as a function of incubation time at pH ≥ 5.4. In contrast, particles incubated under more acidic conditions did not display time-dependent changes in swelling. The stability in size and scattering intensity observed for particles at pH 3.4 suggests limited cross-link scission, whereas higher pH values significantly affect the nanogel structure as a function of time.

4.3.3 Temperature-Dependent Erosion

Whereas pH-dependent hydrolytic erosion was an expected characteristic for this cross-linker,[19-22, 41] we also found temperature-dependent behavior for the scattering and swelling. The temperature effects were characterized through the A4F/MALS method, assessing size and scattering for particles incubated at several temperatures. Similar to the pH-studies, nanogels were analyzed at predetermined time intervals for scattering intensities and the r_{rms} throughout the reaction.

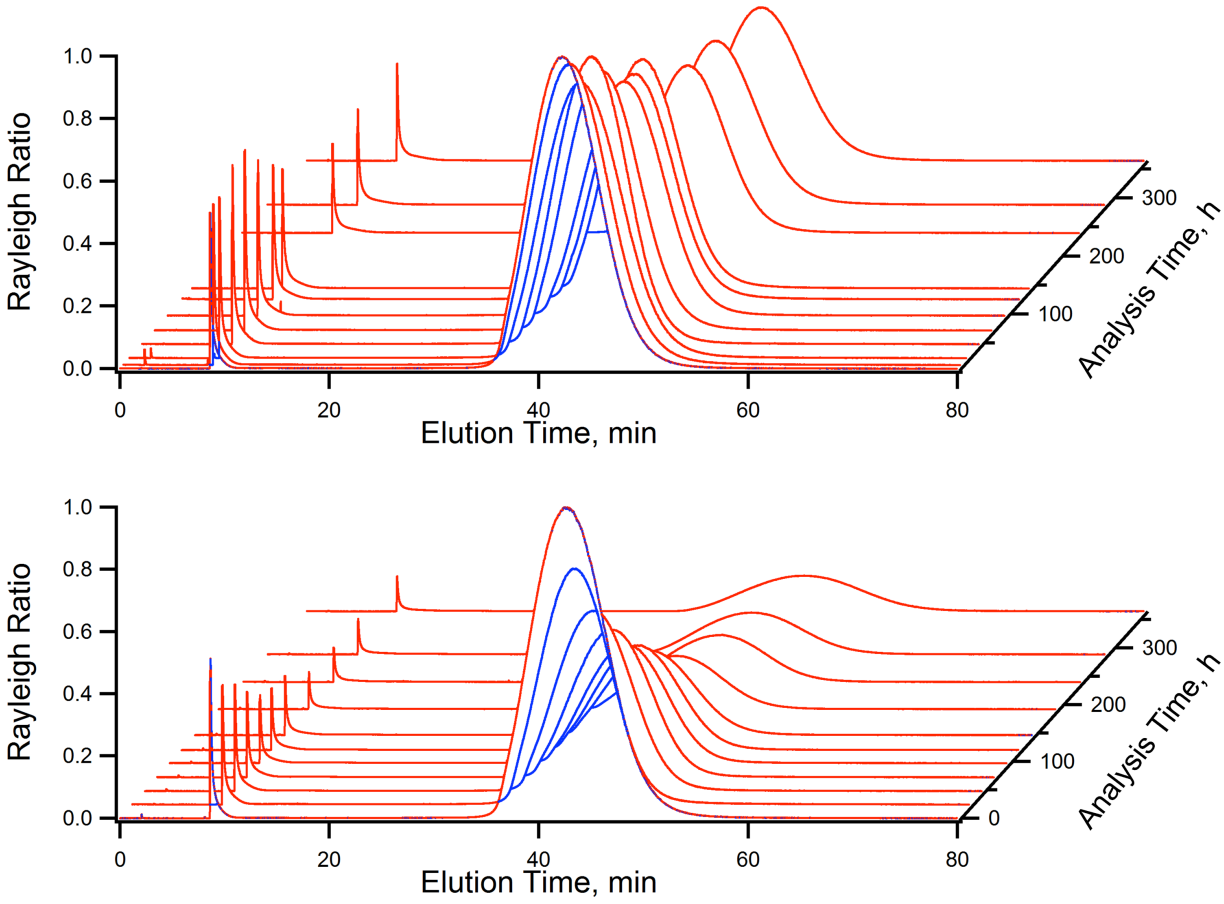

Figure 4.5 Nanogel erosion rates are temperature dependent. Asymmetrical flow FFF elution profiles for temperature-induced erosion experiments at pH 7.4, with light scattering detection at an angle of 90°. Data were collected at (top) 22 °C and (bottom) 37 °C.

Figure 4.5 shows a series of A4F fractograms, with light scattering detection at 90°. As shown in **Figure 4.5** (top), the scattering intensity of particle elutions remained stable when nanogels were maintained at room temperature (22 °C). However, when incubated at elevated temperatures, the particles showed significant decay in scattering, as observed in **Figure 4.5** (bottom). Whereas particles at 22 °C showed minimal erosion, there was no observable difference in scattering intensity or size for nanogels maintained under refrigeration (4 °C, data not shown). Nanogel swelling and scattering decay progressed in a similar fashion as observed in the pH-dependent erosion experiments.

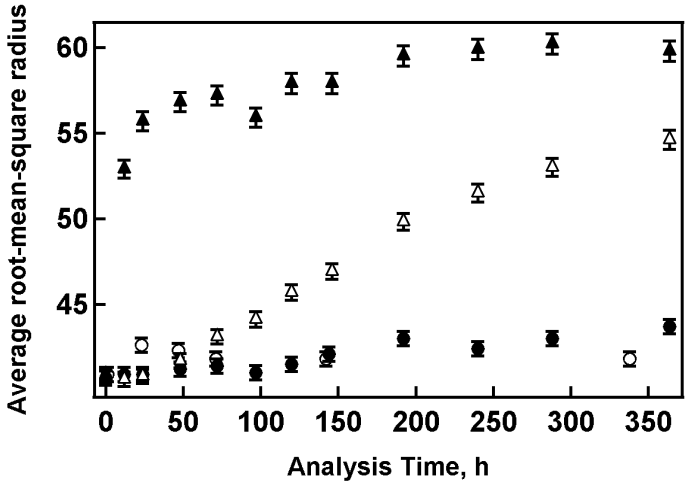

Figure 4.6 Erosion-induced particle swelling is temperature dependent. Nanogel weight-average r_{rms} values were determined by MALS as a function of time and temperature at 4 °C (open circles), 22 °C (filled circles), 37 °C (open triangles), and 50 °C (filled triangles) at pH 7.4. Error bars represent the error of the Debye plot polynomial fit of the scattering data, reported across all slices and detectors.

As shown in **Figure 4.6**, the nanogels expanded in size after incubation at elevated temperatures (e.g. 37-50 °C). This phenomenon was absent for particles maintained at lower temperatures (e.g. 4 °C), where the particles maintained their original r_{rms} values.

4.3.4 Characterization of Nanogel Molar Mass and Number Sensitivity

The decrease in scattering signal and enhanced swelling observed in **Figures 4.2-4.6** are indicative of nanogel erosion. We hypothesized that cross-link scission caused mass loss in the particle along with swelling due to a decrease in network connectivity. Additional experiments were performed using A4F/MALS/dRI, where on-line refractometry permitted the measurement of nanogel concentration in eluting fractions, and thus the derivation of M_w.[38] Dry pNIPMAm-DMHA nanogels were resuspended under erosion-inducing conditions (pH 8.4, 37 °C) and analyzed at predetermined time intervals by A4F/MALS/dRI. The scattering intensity of the eluting nanogels decreased

throughout erosion reaction, in agreement with pH and temperature-dependent erosion experiments.

The observed decay in scattering provided qualitative evidence of mass loss in the nanogel construct, as described above. Cross-linker scission likely permitted polymer dissociation from the nanogels, since cross-linking agents are what impart dimensional stability to these constructs below the VPTT.[1] Thus, it is likely that polymer loss occurred upon DMHA hydrolysis, resulting in a decrease in nanogel molar mass. Using A4F/MALS/dRI, the weight-average molar mass of nanogels was monitored for each eluting fraction.

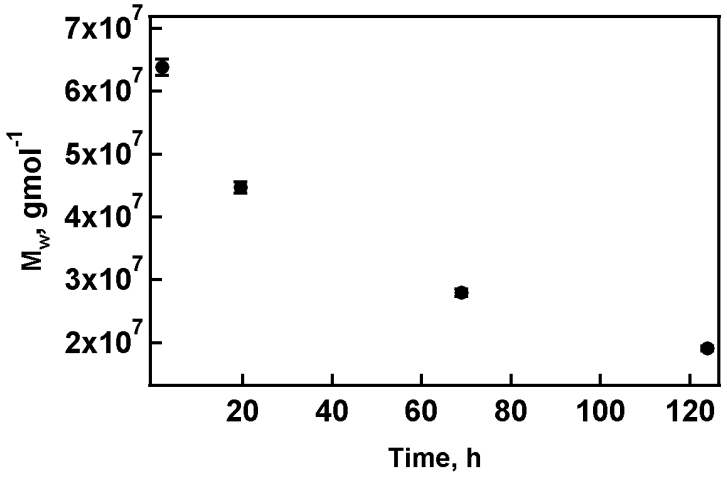

Figure 4.7. Nanogel weight-averaged molar mass (M_w) decay for particles incubated in erosion-inducing buffers (pH 8.4, 37 °C incubation), as measured through the A4F/MALS/dRI method. Particle M_w were determined through a Debye plot of light scattering data. Error bars represent the error of the Debye plot polynomial fitting, reported across all slices and detectors.

As shown in **Figure 4.7**, the molar mass of pNIPMAm-DMHA nanogels indeed decreased substantially during the erosion process. However, after 120 hours of incubation a significant portion of nanogel mass remained (~1.9 x 10^7 g/mol).

An attractive feature of the A4F/MALS/dRI method is the ability to recover eluted fractions for subsequent analysis. Using off-line particle tracking analysis via the NanoSight LM20, the r_h of fractionated particles was determined. The LM20 is capable

of tracking nanogel particles at very low concentrations (~0.008 mg/mL for particle fractions), which is below the concentration threshold for conventional DLS analysis of this nanoparticle type. Through characterization of r_h and r_{rms} for each particle fraction, nanoparticle mass distribution (ρ) was monitored throughout erosion.

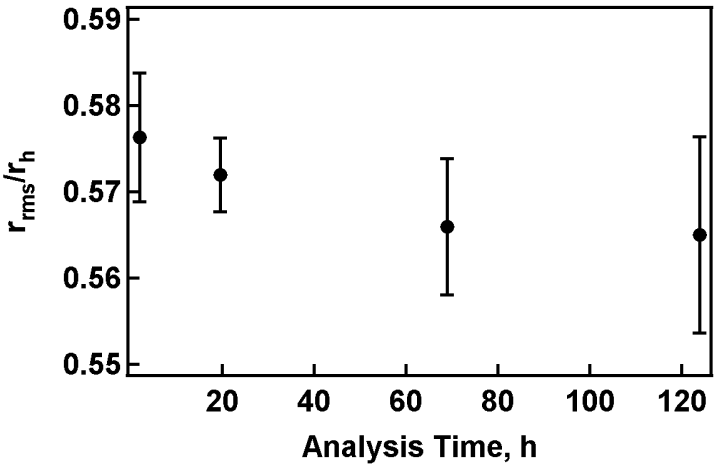

Figure 4.8 The stability of r_{rms}/r_h throughout the erosion reaction, measured via A4F/MALS/dRI with subsequent particle tracking analysis off-line. Error bars represent the absolute uncertainty of all measurements (N=4).

From these analyses, we found that the pNIPMAm-DMHA nanogels do not demonstrate a statistically significant change in r_{rms}/r_h throughout the reaction (Figure 4.8). Since the topology or mass distribution remains relatively stable throughout erosion, it is evident that the degradation-induced swelling observed occurs homogeneously throughout the particle.

The abundance of particles available for tracking greatly decreased throughout erosion. Using the LM20 particle tracking system, the average observed number density of particles in the elution fractions were estimated (Figure 4.9).

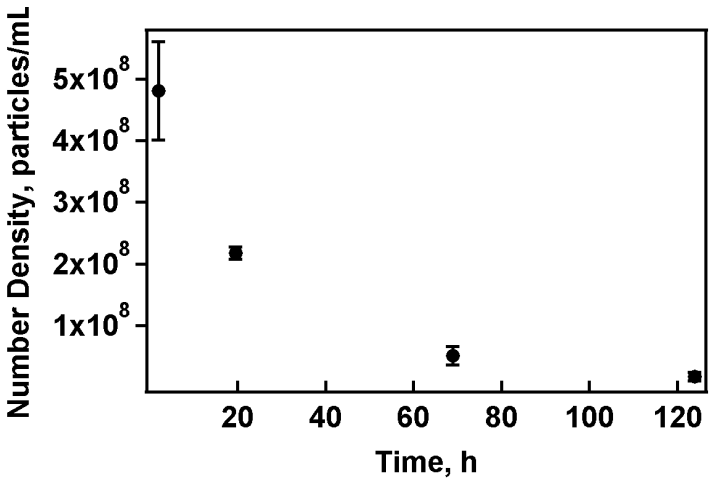

Figure 4.9. Decrease in nanogel number density as a function of erosion time at pH 8.4 and 37 °C from particle tracking analysis. Error bars represent the absolute uncertainty of multiple measurements (N=5).

It is important to note that this number density value represents the remnant particles detectable by the particle tracking system, and is not necessarily representative of the absolute number density of particles remaining. Nanogels were undetectable by particle tracking after ~128 hours of incubation in erosion-inducing conditions (pH 8.4, 37 °C). However, from MALS analysis it is clear that a significant portion of particles remained after extensive erosion times, as shown in **Figure 4.2** and **Figure 4.5**.

From the data presented above**,** we have found that pNIPMAm-DMHA nanogels undergo erosion at neutral pH and elevated temperatures. Originally we anticipated that cross-link scission would result in complete dissolution of polymer from the nanogel network. Without cross-linking agents in the network, the particles would lose dimensional stability and dissociate completely into linear chains. In this scheme, nanogels would not be detectable after DMHA hydrolysis. However, a detectable population of particles remains despite extensive erosion times (2 months in erosion-inducing buffers). This population of particles was undetectable by our dRI configuration and nanoparticle tracking system, which makes molar mass and r_h determination not possible. However, A4F/MALS analysis was an effective means for characterizing the

size and scattering profile of the remaining nanogels. After 4 weeks of erosion (pH 8.4, 37 °C), a stable population of highly swollen (r_{rms} = 55-60 nm) particles of very low scattering intensity (< 10% of the original *R(θ)* value) was present, as evident by peak intensity at θ = 90°.

The presence of an intact polymer network with dimensional stability suggests that cross-linking remains in the nanogels, despite hydrolysis of DMHA. We attribute the presence of stable nanoparticles (despite cross-link scission) to the self-cross-linking of pNIPMAm chains via a chain transfer reaction. This phenomenon has been observed for similarly structured pNIPAm chains, where particles are formed in precipitation polymerization despite a lack of added cross-linking agents.[42] The pNIPMAm chains may undergo a similar reaction, involving free radical formation on the tertiary radical of the pendent isopropyl group on the side chain. A result of chain transfer is the formation of intrinsic cross-links in the polymer network, which would prevent complete polymer dissociation upon scission of DMHA. However, additional experiments were performed to validate these claims (Chapter 5), where complete particle dissolution was found for pNIPMAm microgels cross-linked with a another chemically-labile cross-linker (1,2-dihydroxylethylene)bisacrylamide (DHEA). This result may indicate that self-cross-linking is not a significant factor for those structures. Instead, remaining cross-linking in the particle may be due to incomplete scission of DMHA or chain entanglement that prevents complete dissolution for those networks. Additional experiments are necessary to verify this discrepancy.

4.4 Conclusions

This chapter described the synthesis of hydrolytically degradable, thermoresponsive nanogels via persulfate-intitiated precipitation polymerization. Those particles were produced through the copolymerization of NIPMAm and DMHA, yielding

monodisperse, thermoresponsive nanogels of appropriate size for intravenous drug delivery applications. To fully characterize nanogel erosion, AF4/MALS was used to monitor pNIPMAm-DMHA nanogel behavior in various media. Through A4F, particles were separated from degradation products to improve detection by light scattering. Nanogels showed pH and temperature dependence to erosion, where particles degraded faster at neutral to basic pH and at elevated temperatures. Under these conditions, DMHA scission was evident from an increase in particle swelling, and a decrease in scattering intensity for eluting peaks. The loss in light scattering is indicative of mass loss within the nanogel construct, which is an attractive feature from the standpoint for intravenous drug delivery and renal clearance. By adding on-line differential refractometry detection and off-line particle tracking analysis to our method, nanogel size (r_h and r_{rms}), molar mass, and number densities were monitored for sample fractions. Using this technique, the loss of molar mass for nanogels maintained in erosion-inducing buffers was confirmed. Using the ratio of r_{rms}/r_h (ρ), the topology of nanogels was found to remain stable throughout degradation. The ρ value is indicative of the distribution of polymer mass throughout the nanogel architecture, which was conserved despite scission of DMHA and polymer dissociation from the nanogels.

The presence of remaining nanogels despite extensive erosion was a surprising result. After erosion, a highly swollen fraction of particles persisted whose low scattering profile suggests a decreased M_w. We attributed the presence of remaining particles to possible self-cross-linking behavior of the pNIPMAm chains; this phenomenon was further investigated in Chapter 5. The analytical method described in this chapter was a highly versatile and powerful means to assess the size, molar mass, topology, and number density of degradable nanogels during the erosion process. We anticipate that this technique should find applicability in the characterization of other degradable particle constructs, and will enable the future development of improved architectures for drug delivery.

4.5 References

1. Nayak, S.; Lyon, L. A., Soft nanotechnology with soft nanoparticles. *Angew. Chem., Int. Ed.* **2005,** *44* (47), 7686-7708.

2. Gan, D. J.; Lyon, L. A., Synthesis and protein adsorption resistance of PEG-modified poly(N-isopropylacrylamide) core/shell microgels. *Macromolecules* **2002,** *35* (26), 9634-9639.

3. Nolan, C. M.; Reyes, C. D.; Debord, J. D.; Garcia, A. J.; Lyon, L. A., Phase Transition Behavior, Protein Adsorption, and Cell Adhesion Resistance of Poly(ethylene glycol) Cross-Linked Microgel Particles. *Biomacromolecules* **2005,** *6* (4), 2032-2039.

4. Eichenbaum, G. M.; Kiser, P. F.; Dobrynin, A. V.; Simon, S. A.; Needham, D., Investigation of the swelling response and loading of ionic microgels with drugs and proteins: The dependence on cross-link density. *Macromolecules* **1999,** *32* (15), 4867-4878.

5. Missirlis, D.; Kawamura, R.; Tirelli, N.; Hubbell, J. A., Doxorubicin encapsulation and diffusional release from stable, polymeric, hydrogel nanoparticles. *Eur. J. Pharm. Sci.* **2006,** *29* (2), 120-129.

6. Goh, S. L.; Murthy, N.; Xu, M.; Frechet, J. M. J., Cross-Linked Microparticles as Carriers for the Delivery of Plasmid DNA for Vaccine Development. *Bioconjug. Chem.* **2004,** *15* (3), 467-474.

7. Lee, H.; Mok, H.; Lee, S.; Oh, Y.-K.; Park, T. G., Target-specific intracellular delivery of siRNA using degradable hyaluronic acid nanogels. *J. Control. Release* **2007,** *119* (2), 245-252.

8. Ayame, H.; Morimoto, N.; Akiyoshi, K., Self-Assembled Cationic Nanogels for Intracellular Protein Delivery. *Bioconjug. Chem.* **2008,** *19* (4), 882-890.

9. Blackburn, W. H.; Dickerson, E. B.; Smith, M. H.; McDonald, J. F.; Lyon, L. A., Peptide-Functionalized Nanogels for Targeted siRNA Delivery. *Bioconjug. Chem.* **2009,** *20* (5), 960-968.

10. Ogawara, K.; Yoshida, M.; Furumoto, K.; Takakura, Y.; Hashida, M.; Higaki, K.; Kimura, T., Uptake by hepatocytes and biliary excretion of intravenously administered polystyrene microspheres in rats. *J. Drug Target.* **1999,** *7* (3), 213-+.

11. Cohen, S.; Yoshioka, T.; Lucarelli, M.; Hwang, L. H.; Langer, R., Controlled delivery systems for proteins based on poly(lactic glycolic acid) microspheres. *Pharm. Res.* **1991,** *8* (6), 713-720.

12. Wang, Y. M.; Sato, H.; Adachi, I.; Horikoshi, I., Preparation and characterization of poly(lactic-co-glycolic acid) microspheres for targeted delivery of a novel anticancer agent, Taxol. *Chem. Pharm. Bull.* **1996,** *44* (10), 1935-1940.

13. Anderson, J. M.; Shive, M. S., Biodegradation and biocompatibility of PLA and PLGA microspheres. *Adv. Drug Delivery Rev.* **1997,** *28* (1), 5-24.

14. Lenaerts, V.; Couvreur, P.; Christiaens-Leyh, D.; Joiris, E.; Roland, M.; Rollman, B.; Speiser, P., Degradation of poly (isobutyl cyanoacrylate) nanoparticles. *Biomaterials* **1984,** *5* (2), 65-68.

15. Chawla, J. S.; Amiji, M. M., Biodegradable poly(epsilon-caprolactone) nanoparticles for tumor-targeted delivery of tamoxifen. *Int. J. Pharm.* **2002,** *249* (1-2), 127-138.

16. Vauthier, C.; Dubernet, C.; Fattal, E.; Pinto-Alphandary, H.; Couvreur, P., Poly(alkylcyanoacrylates) as biodegradable materials for biomedical applications. *Adv. Drug Delivery Rev.* **2003,** *55* (4), 519-548.

17. Satish Nayak, D. G. Michael J. S. L. A. L., Hollow Thermoresponsive Microgels. *Small* **2005,** *1* (4), 416-421.

18. Hennink, W. E.; van Nostrum, C. F., Novel crosslinking methods to design hydrogels. *Adv. Drug Delivery Rev.* **2002,** *54* (1), 13-36.

19. Horak, D.; Kroupava, J.; Slouf, M.; Dvorak, P., Poly(2-hydroxyethyl methacrylate)-based slabs as a mouse embryonic stem cell support. *Biomaterials* **2004,** *25* (22), 5249-5260.

20. Seymour, L. W.; Miyamoto, Y.; Maeda, H.; Brereton, M.; Strohalm, J.; Ulbrich, K.; Duncan, R., Influence of molecular-weight on passive tumor accumulation of a soluble macromolecular drug carrier. *Eur. J. Cancer* **1995,** *31A* (5), 766-770.

21. Ulbrich, K.; Subr, V.; Seymour, L. W.; Duncan, R., Novel biodegradable hydrogels prepared using the divinylic cross-linking agent n,o-dimethacryloylhydroxylamine .1. synthesis and characterization of rates of gel degradation, and rate of release of model-drugs, invitro and invivo. *J. Control. Release* **1993**, 181-190.

22. Pradny, M.; Michalek, J.; Lesny, P.; Hejcl, A.; Vacik, J.; Slouf, M.; Sykova, E., Macroporous hydrogels based on 2-hydroxyethyl methacrylate. Part 5: Hydrolytically degradable materials. *J. Mater. Sci.: Mater. Med.* **2006,** (17), 1357-1364.

23. Wahlund, K. G.; Giddings, J. C., Properties of an asymmetrical flow field-flow fractionation channel having one permeable wall. *Anal. Chem.* **1987,** *59* (9), 1332-1339.

24. Andersson, M.; Wittgren, B.; Wahlund, K. G., Ultrahigh molar mass component detected in ethylhydroxyethyl cellulose by asymmetrical flow field-flow fractionation coupled to multiangle light scattering. *Anal. Chem.* **2001,** *73* (20), 4852-4861.

25. Wittgren, B.; Wahlund, K. G., Fast molecular mass and size characterization of polysaccharides using asymmetrical flow field-flow fractionation-multiangle light scattering. *J. Chromatogr. A* **1997,** *760* (2), 205-218.

26. Blackburn, W. H.; Lyon, L. A., Size-controlled synthesis of monodisperse core/shell nanogels. *Colloid Polym. Sci.* **2008,** *286* (5), 563-569.

27. Meng, Z. Y.; Smith, M. H.; Lyon, L. A., Temperature-programmed synthesis of micron-sized multi-responsive microgels. *Colloid Polym. Sci.* **2009,** *287* (3), 277-285.

28. Pich, A.; Berger, S.; Ornatsky, O.; Baranov, V.; Winnik, M. A., The influence of PEG macromonomers on the size and properties of thermosensitive aqueous microgels. *Colloid Polym. Sci.* **2009,** *287* (3), 269-275.

29. Litzen, A.; Wahlund, K. G., Zone broadening and dilution in rectangular and trapezoidal asymmetrical flow field-flow fractionation channels. *Anal. Chem.* **2002,** *63* (10), 1001-1007.

30. Sorrell, C. D.; Lyon, L. A., Deformation controlled assembly of binary microgel thin films. *Langmuir* **2008,** *24* (14), 7216-7222.

31. Zhunuspayev, D. E.; Mun, G. A.; Hole, P.; Khutoryanskiy, V. V., Solvent Effects on the Formation of Nanoparticles and Multilayered Coatings Based on Hydrogen-Bonded Interpolymer Complexes of Poly(acrylic acid) with Homo- and Copolymers of N-Vinyl Pyrrolidone. *Langmuir* **2008,** *24* (23), 13742-13747.

32. Burchard, W.; Schmidt, M.; Stockmayer, W. H., Information on polydispersity and branching from combined quasi-elastic and integrated scattering. *Macromolecules* **1980,** *13* (5), 1265-1272.

33. Wang, X.; Wu, C., Light-Scattering Study of Coil-to-Globule Transition of a Poly(N-isopropylacrylamide) Chain in Deuterated Water. *Macromolecules* **1999,** *32* (13), 4299-4301.

34. Lise, A.; Xiaohu, X.; Rex, P. H.; Jianzhong, W.; Zhibing, H., Volume transition and internal structures of small poly(N-isopropylacrylamide) microgels. *Journal of Polymer Science Part B: Polymer Physics* **2005,** *43* (7), 849-860.

35. Djokpe, E.; Vogt, W., N-isopropylacrylamide and N-isopropylmethacrylamide: Cloud points of mixtures and copolymers. *Macromol. Chem. Phys.* **2001,** *202* (5), 750-757.

36. Katsumoto, Y.; Tanaka, T.; Sato, H.; Ozaki, Y., Conformational change of poly(N-isopropylacrylamide) during the coil-globule transition investigated by attenuated

total reflection/infrared spectroscopy and density functional theory calculation. *J. Phys. Chem. A* **2002,** *106* (14), 3429-3435.

37. Tang, Y. C.; Ding, Y. W.; Zhang, G. Z., Role of methyl in the phase transition of poly(N-isopropylmethacrylamide). *J. Phys. Chem. B* **2008,** *112* (29), 8447-8451.

38. Wyatt, P. J., Light-scattering and the absolute characterization of macromolecules. *Anal. Chim. Acta* **1993,** *272* (1), 1-40.

39. Litzén, A.; Wahlund, K.-G., Effects of temperature, carrier composition and sample load in asymmetrical flow field-flow fractionation. *J. Chromatogr. A* **1991,** *548*, 393-406.

40. Senff, H.; Richtering, W., Influence of cross-link density on rheological properties of temperature-sensitive microgel suspensions. *Colloid Polym. Sci.* **2000,** *278* (9), 830-840.

41. Ulbrich, K.; Subr, V.; Podperova, P.; Buresova, M., Synthesis of novel hydrolytically degradable hydrogels for controlled drug-release. *J. Control. Release* **1995,** *34* (2), 155-165.

42. Gao, J.; Frisken, B. J., Cross-Linker-Free N-Isopropylacrylamide Gel Nanospheres. *Langmuir* **2003,** *19* (13), 5212-5216.

CHAPTER 5

NETWORK DECONSTRUCTION REVEALS NETWORK STRUCTURE IN RESPONSIVE MICROGELS

Adapted from

Smith MH, Herman ES, Lyon LA. *J. Phys. Chem. B*, 2011, 115 (14) 3761-3764.

5.1 Introduction

Responsive hydrogel particles (microgels) are a versatile class of materials with potential utility in the encapsulation and delivery of therapeutic compounds.[1-5] As a result of their proposed use *in vivo*, microgels possessing degradable properties have gained significant attention in recent years.[5-6] By enabling polymer decomposition into low molar mass components, the clearance of the vehicles may be facilitated, whereas erosion might also be used to modulate drug release from the polymer matrix.

Although microgel drug delivery systems are gaining increased visibility, several hurdles remain before they can be discussed as competent delivery vehicles for clinical applications. In the context of degradable microgels, assessment of erosion rate, erosion mechanism, and products of the degradation reaction are essential for a complete understanding of the carrier's behavior. As seen with other erodible polymers, these characteristics are likely to influence polymer network diffusivity and drug release rates,[7] and the stability of particles in biological media (as a result of size and topological changes).[8-9] In an ongoing effort to investigate microgel erosion dynamics, we and others have employed a variety of techniques including atomic force microscopy (AFM),[10-11] multiangle light scattering (MALS),[10, 12] and other optical methods.[13-15]

In this chapter it is shown how the characterization of microgel network structure can be facilitated by the detailed observation of that network's deconstruction. To illustrate the approach, we employed microgel particles composed of two different thermoresponsive polymers: poly(*N*-isopropylacrylamide) (pNIPAm) and poly(*N*-isopropylmethacrylamide) (pNIPMAm).[16-17] Microgel erosion was enabled through copolymerization with a chemically labile cross-linker,[18] (1,2-dihydroxylethylene)-bisacrylamide (DHEA), via precipitation polymerization. The DHEA cross-linker contains a vicinal diol that is rapidly cleaved in the presence of periodate, resulting in destruction of the polymer network.[14] Using MALS in conjunction with a controlled reagent delivery and mixing device (**Scheme 2.6**), we measured the real-time changes in microgel solution-average r_{rms} and M_w during erosion, thereby revealing distinct differences in network erosion rates and pathways between the two microgel types.

5.2 Experimental Section

5.2.1 Materials

All reagents were purchased from Sigma-Aldrich (St Louis, MO) and used as received, unless otherwise noted. The monomers *N*-isopropylacrylamide (NIPAm) and *N*-isopropylmethacrylamide (NIPMAm) was recrystallized from hexanes (VWR international, West Chester, PA) and dried in vacuo prior to use. Reagents *N,N'*-methylenebisacrylamide (BIS), sodium dodecyl sulfate (SDS), ammonium persulfate (APS), sodium periodate ($NaIO_4$), and (1,2-dihydroxylethylene)bisacrylamide (DHEA) were all used as received. Water used in all reactions and particle purifications was purified to a resistance of 18 MΩ (Barnstead E-Pure system), and filtered through a 0.2 μm filter to remove particulate matter.

5.2.2 Microgel Synthesis

The synthesis of pNIPAm-DHEA and pNIPMAm-DMHA microgels was performed via surfactant-stabilized precipitation polymerization, using a modified approach to what has been previously published.[14] The molar composition of reagents was 90% monomer (NIPAm or NIPMAm) and 10% DHEA, with a total monomer concentration of 70 mM and 140 mM for the pNIPAm and pNIPMAm syntheses, respectively. The total synthesis volume was 50.0 mL. The reactions were performed by separately dissolving NIPAm or NIPMAm monomer (0.387 g or 0.801 g) in 49.0 mL of distilled, deionized water. A mass of 0.070 g DHEA was dissolved in the NIPAm solution, whereas 0.140 g DHEA was dissolved in the NIPMAm solution. A mass 0.029 g SDS was added to both solutions, forming a final synthesis concentration of 2 mM. Each solution was filtered through a 0.2 μm Acrodisc syringe filter and subsequently added to 100 mL three-neck round-bottom flasks. Once equilibrated at 70 °C, the reaction mixtures were purged with N_2 for an hour while stirring (400 RPM). The polymerizations were initiated by delivering a 1.0 mL aliquot of 0.200 M APS solution by pipette. All reactions were allowed to proceed for 24 hours under an N_2 blanket while continuously stirring. Once cooled, both solutions were filtered through 0.8 μm Acrodisc syringe filters and purified via repeated ultracentrifugation and resuspension in distilled, deionized water.

5.2.3 Instruments

Particle *Mw* and *dn/dc* values were determined in batch mode using the Calypso syringe pump system (Wyatt Technology Corporation, Santa Barbara, CA). As discussed in Chapter 2, the Calypso hardware consists of a computer-controlled triplet syringe pump and a multichannel degasser, equipped with in-line filters, mixers and valves to allow rapid and automated batch measurements. A diagram of the specific instrument configuration is shown in **Scheme 2.6**.

Multiangle light scattering was performed using the DAWN-EOS (Wyatt Technology Corporation, Santa Barbara, CA) equipped with a temperature-regulated K5 flow cell with a GaAs laser light source (λ = 685 nm). Data collection and subsequent light scattering analysis was performed using the Astra software Version 5.3.4.14 (Wyatt Technology Corporation, Santa Barbara, CA). Accurate measurements of microgel molar mass required characterization of the particle refractive increment (*dn/dc*). Differential refractive index analysis was performed via composition-gradient static light scattering using the Calypso and Optilab rEX system, equipped with an LED light source (λ = 690 nm). The hydrodynamic radii (r_h) of nanogels were measured via dynamic light scattering (DLS). DLS experiments were performed at a 90° scattering angle using a Protein Solutions DLS (Wyatt Technology Corporation, Santa Barbara, CA).

5.2.4 Light Scattering Validation

The principles employed in MALS measurements have been described in Chapter 2 and in detail elsewhere.[19] To ensure accuracy in angular-dependent fitting with our instrument configuration, polystyrene microparticle standards (Duke Scientific, Palo Alto, CA) of varying radii (0.326 μm, 0.200 μm, 0.102 μm, and 0.0478 μm) were first characterized using the Debye method to construct the Debye plot. Polystyrene standards were diluted to a concentration of 5 x 10^{-4} wt% solids in filtered (0.1 μm Anodisc) distilled, deionized water containing 3 mM NaN_3 and 3 mM SDS. A typical characterization experiment was conducted as follows. A baseline scattering signal was established by loading syringe 1 with particle-free solvent (containing 3 mM NaN_3) from reservoir 1 (the instrument configuration is shown schematically in **Scheme 2.5**). Following baseline measurement, particles were introduced into the flow system through syringe 2, drawing particle samples from reservoir 2. Using the Calypso software, a programmed concentration gradient of polystyrene was established through modification of the flow rates of each syringe. Data analysis was performed at stopped-flow at each

concentration. This method enabled the rapid optimization of sample concentration to give adequate signal for MALS detection (typically 2.5 x 10^{-4} wt% polystyrene). All mathematical transformations and data fitting were performed using the Astra software Version 5.3.4.14 (Wyatt Technology Corporation, Santa Barbara, CA).

A series of standard microspheres were characterized via MALS. Polystyrene spheres of radii 0.326 μm, 0.200 μm, 0.102 μm, and 0.0478 μm were analyzed using the Debye method to solve the Debye plot, where various fit degrees were compared for accuracy. The topology may be inferred through the ratio of the r_{rms} (which is the particle dimension, weighted by the mass distribution about the center of particle mass) and the r_h (which is a measure of the diffusion coefficient of the particle, or its volume of occupancy). The ratio is represented by dimensionless parameter $\rho = r_{rms} / r_h$. Accuracy in fitting was assessed assuming a smooth sphere topology for polystyrene particles (ρ = 0.77), which has been demonstrated elsewhere.[20] Fit accuracy was thus assessed from the measured r_{rms} and a theoretical value for r_{rms} assuming a homogeneous topology for the standard. The 0.0478 μm and 0.102 μm spheres required first order and second order fitting, respectively. In contrast, fourth-order and fifth-order fitting was required for the 0.200 μm and 0.326 μm spheres

5.2.5 Microgel Characterization and In Situ Erosion

Microgel samples were prepared in 0.1 μm filtered 3 mM NaN_3 media at a concentration of 4.8 x 10^{-3} mg/mL or 6.0 x 10^{-4} mg/mL for pNIPAm-DHEA and pNIPMAm-DHEA particles, respectively. Particles composed of pNIPMAm-BIS were characterized in identical media at a polymer concentration optimized for light scattering signal (~0.2-1.0 μg/mL for 2-8% BIS particles). Characterization experiments were performed similarly to what was described for polystyrene standards. A baseline scattering signal was established by loading pump 1 with particle-free media from reservoir 1. Microgel samples were loaded from reservoir 2 into syringe pump 2.

Particles were diluted to 50% stock concentration in situ through the use of pump 1 (loaded with particle-free media containing 3 mM NaN_3). Particle size and molar mass were characterized at stopped-flow using the Astra software. For erosion experiments, baseline measurements were instead made in a mixture of particle-free media (syringe 1) and $NaIO_4$ stock solutions (200 mM, 20 mM, 2 mM, and 0.2 mM) loaded from reservoir 3 into syringe 3. All periodate samples were prepared in 3 mM NaN_3 media and pre-filtered through a 0.1 μm Anodisc filter. Following baseline measurement, particles were diluted to 50% stock concentration in situ through the use of syringe 3 (containing the sodium periodate stock). The erosion of microgels was monitored via MALS in situ using the Astra software.

The hydrodynamic radii of pNIPAm-DHEA and pNIPMAm-DHEA microgels were determined by DLS. Particles were characterized at a concentration of 0.01 wt% in distilled, deionized water containing 3 mM NaN_3. All microgel samples were allowed to equilibrate thermally for 30 min before measurement at 25 ºC. Sizing measurements represent an average value of 20 measurements, with a 10 s integration time each, performed in triplicate analysis. All correlogram analyses were performed using the Dynamic v.5.25.44 software (Wyatt Technology Corporation, Santa Barbara, CA). The r_h of particles were determined from their respective diffusion coefficients according to the Stokes-Einstein relation.

5.3 Results and Discussion

The distinct structural features of both microgel types are graphically depicted in **Scheme 5.1**. Although the microgels had comparable r_{rms} values, the different hydrodynamic radii (r_h) suggest mass distribution differences between the spheres.

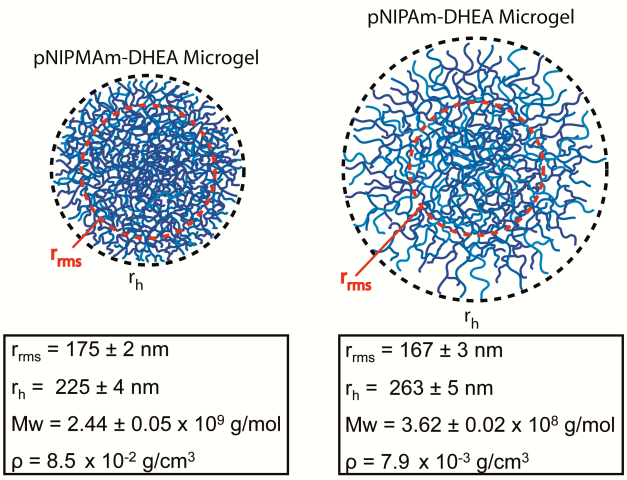

Scheme 5.1. Molar mass, density, and proposed microgel topology from light scattering characterization. Topological differences were observed for the spheres with comparable r_{rms} but with divergent r_h values.

The mass distribution may be inferred from the ratio of the r_{rms} (the particle dimension weighted by the mass distribution about the center of mass) and the r_h (inferred from the particle diffusion coefficient) determined through DLS.[21] As shown in **Scheme 5.1** this ratio for the pNIPAm-DHEA microgels is $r_{rms}/r_h = 0.63$, which indicates a radially inhomogeneous mass distribution as observed previously for other microgel chemistries.[22] In contrast, the calculated ratio for pNIPMAm-DHEA microgels ($r_{rms}/r_h = 0.78$) is indicative of a smooth sphere with an even distribution of mass throughout the particle. Particles composed of pNIPMAm are also significantly denser than pNIPAm spheres, suggesting enhanced cross-linker incorporation.

Microgel erosion was monitored in real-time via MALS in the presence of excess periodate. In a typical erosion experiment, microgels and sodium periodate were pumped and mixed into the MALS flow cell with constant monitoring of the *Mw* and r_{rms} values. Constant *Mw* values were observed under flow conditions as the reactants were repeatedly replenished in the MALS flow cell. A sharp decay in the measured *Mw* values was then observed when the flow was stopped (t = 0 min). The molar mass for both the pNIPMAm and pNIPAm microgels reached equilibrium after ~80 min under the given

experimental conditions. The measured molar mass of the scattering species at that time point was approximately 2-3 orders of magnitude smaller than that of the original microgels (**Figure 5.1-5.2**).

The architectural differences between the microgels resulted in distinct erosion profiles. Simultaneous monitoring of the particle sizes revealed that the r_{rms} of the pNIPMAm microgels increased by ~15% to ~185 nm early in the erosion, with a subsequent decay to slightly smaller spheres and eventually into linear or branched chains with poorly defined angular scattering functions (**Figure 5.1** and **Figure 5.2**).

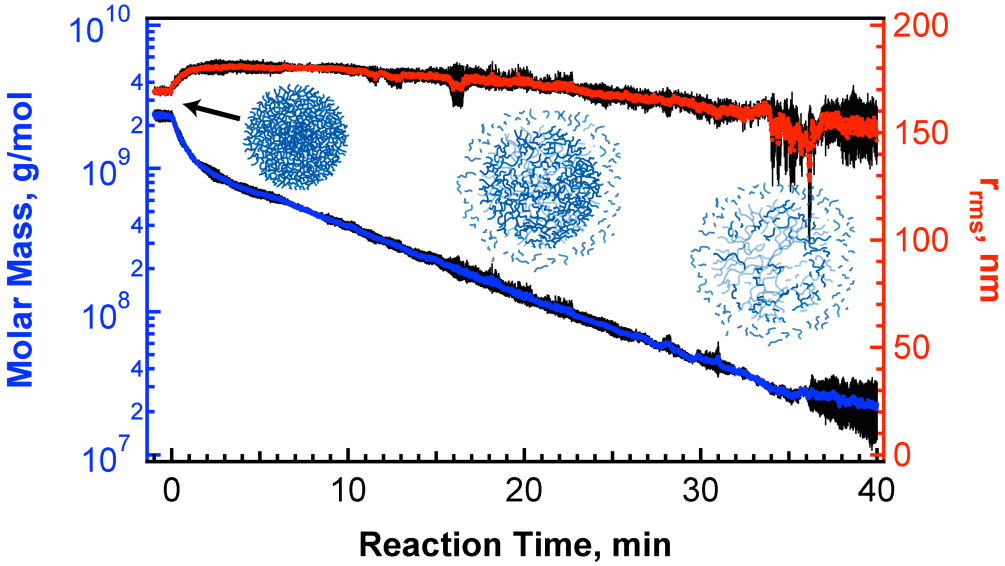

Figure 5.1. Erosion of pNIPMAm-DHEA microgels results in changes in particle molar mass (blue) and r_{rms} (red). The erosion process is schematically represented at different time points (blue spheres). Reactions were monitored at 25 ºC in the presence of excess periodate (100 mM). Error bars (black) represent one standard deviation about the mean of measurements performed in triplicate.

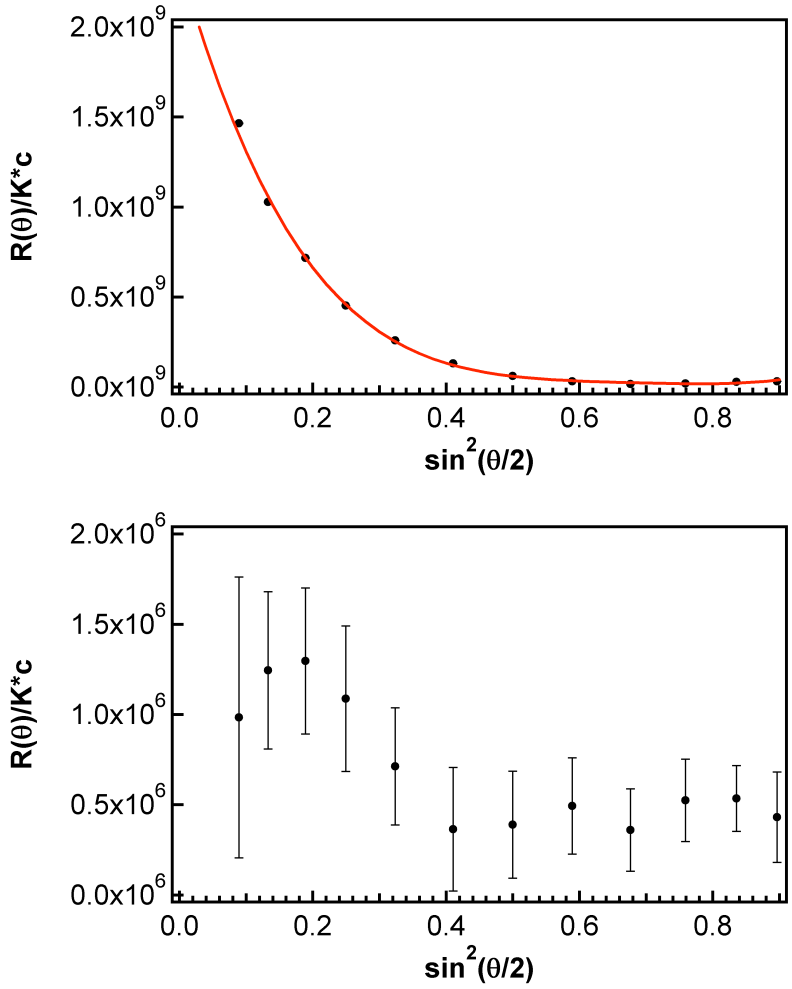

Figure 5.2. Debye plots for pNIPMAm microgels before (top) and after (bottom, t = 80 min) erosion. Angle-dependent scattering for pNIPMAm microgel spheres was lost in the presence of excess periodate. Polynomial fitting of the microgel scattering function (red trace) is represented before erosion, where isotropic scattering was observed after polymer decomposition (bottom). Erosion resulted in low molar mass isotropic scatters (~1.0 x 10^6 g/mol).

This erosion pathway is expected in cases where the network is very homogenous in density and uniform in connectivity. Cross-linker degradation results in a decrease in network connectivity, allowing the network to swell. As the network connectivity continues to decrease, the microgel eventually dissolves into a collection of branched oligomers with low scattering cross-sections (**Figure 5.2**, bottom).

Very different erosion behavior was observed in the case of pNIPAm-DHEA microgels (**Figure 5.3)**.

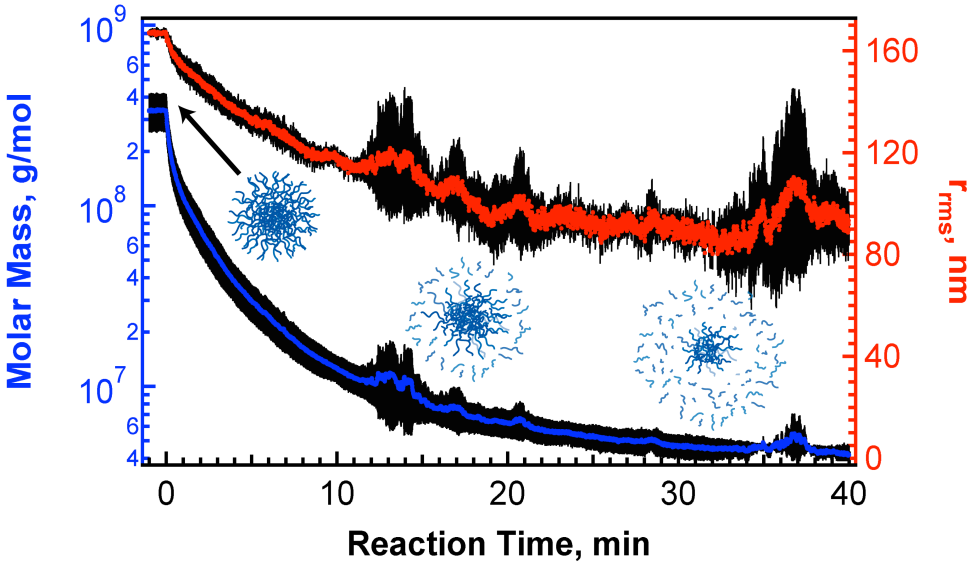

Figure 5.3. Erosion of pNIPAm-DHEA microgels results in the decay of particle molar mass (blue) and r_{rms} (red). The erosion process is schematically represented at different time points (blue spheres). Reactions were monitored at 25 ºC in the presence of excess periodate (100 mM). Error bars (black) represent one standard deviation about the mean of measurements performed in triplicate.

As described above, the combined MALS and DLS data were suggestive of a radial distribution of polymer mass within the microgels, with the greatest polymer connectivity being present in the particle interior. This structure suggests that fewer cleavage events would be required to liberate polymer chains near the sphere periphery relative to the particle core. Thus, mass loss is favored from the exterior of the network, eventually proceeding towards the interior. As shown in **Figure 5.3**, pNIPAm-DHEA spheres demonstrated non-linear molar mass decay throughout erosion. In contrast to the swelling and network extension observed for pNIPMAm spheres, pNIPAm particles instead showed an immediate decrease in their r_{rms} upon erosion, which is associated with mass loss proceeding from the exterior of the particle toward the interior. In other words, the erosion proceeded from regions of low connectivity (the particle periphery) to regions of high connectivity (a highly cross-linked core). However, unlike pNIPMAm spheres the

pNIPAm microgels did not completely dissolve, even after ~80 min of incubation with periodate. Erosion products at that time point continued to display angle-dependent scattering, which is strongly indicative of the presence of remnant spheres following DHEA degradation (**Figure 5.4**).

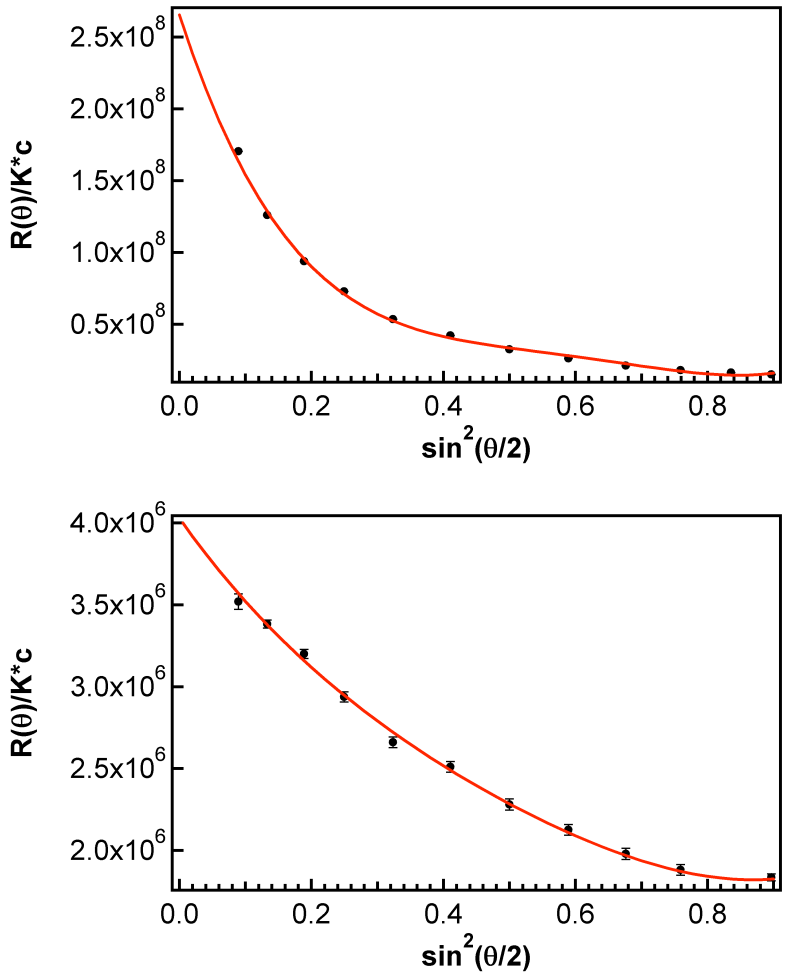

Figure 5.4. Debye plots for pNIPAm microgels before (top) and after (bottom, t = 80 min) erosion. Remaining angle-dependent scattering for pNIPAm microgel spheres suggests colloidal stability despite DHEA degradation. Polynomial fitting of the microgel scattering function (red trace) is represented before and after erosion. Erosion resulted in low molar mass spheres (~4.0 x 10^6 g/mol, bottom).

This dimensional stability is likely imparted by non-degradable cross-linking sites arising from self-cross-linking that occurs during precipitation polymerization.[11, 23] NIPAm is prone to chain transfer reactions via the hydrogen atom on the tert-C of the polymer main

chain, forming non-degradable connectivity (cross-links) in the network. Chain transfer on the main chain is preferred over the hydrogen on the pendent isopropyl group. Thus, microgels composed of pNIPMAm (lacking the tert-C on the main chain) would not be expected to show significant self-cross-linking, a hypothesis that is supported by the complete dissolution of the pNIPMAm spheres in the presence of periodate. Erosion products from pNIPMAm experiments showed loss of angle-dependent scattering, suggesting complete polymer dissolution and destruction of the particle (**Figure 5.2**).

The kinetics of microgel network deconstruction provided additional insight into network structure. The pNIPMAm microgels showed an exponential decrease in *Mw* during erosion, as indicated by the linearity in the *Mw* decay when plotted on a logarithmic scale (**Figure 5.1**). This exponential decay is characteristic for bulk eroding polymers, where the erosion rate generally decreases as polymer is depleted from the particle structure.[7] Decay constant values, λ, for microgel erosion were determined through nonlinear least squares fitting of the exponential decay function, where $Mw(t) = Mw_0 e^{-\lambda t}$. As the concentration of periodate was decreased, the value of λ decreased in a linear fashion (**Figure 5.5**). In contrast, pNIPAm microgels (having an inhomogeneous mass distribution throughout the structure) showed very different kinetic behavior. For these polymers, mass loss proceeds from the exterior regions first (containing less connectivity) towards the interior (containing enhanced connectivity). As a result, the kinetics of molar mass loss decelerates during the erosion reaction (**Figure 5.3**), where reaction velocities are highest early in the reaction, as the peripheral, low-connectivity chains are lost from the structure.

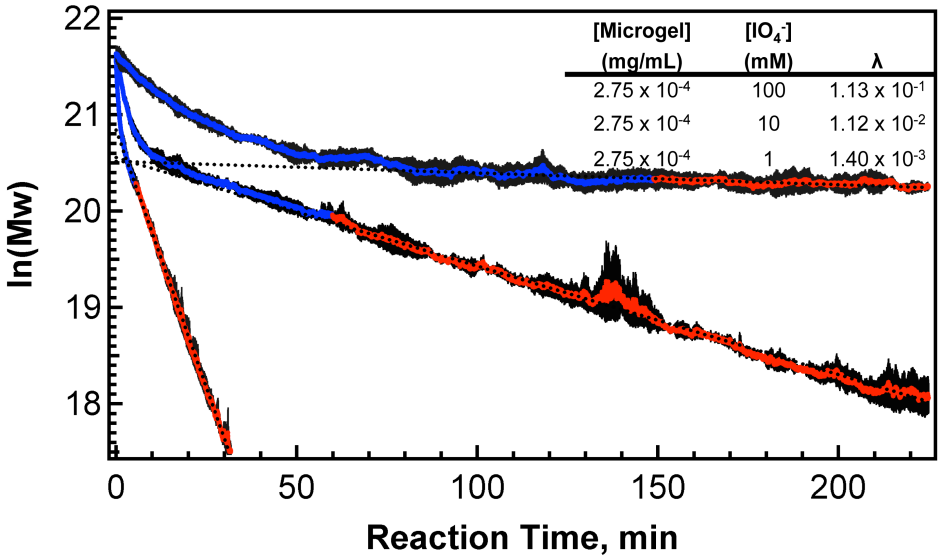

Figure 5.5. First-order erosion kinetics were observed for pNIPMAm spheres throughout the majority of the erosion reaction. Regions showing exponential molar mass decay (red) were fit via nonlinear least squares fitting of the exponential function (dotted blue lines). The decay constant, λ, scaled linearly with periodate concentration.

A direct relationship between the microgel structural composition and the erosion behavior was observed in this Chapter. These divergent structures were likely caused by several factors, including monomer reactivity and cross-linker incorporation differences during polymerization. Heterogeneities in microgel structures are often caused by mismatched reactivity ratios for monomer and cross-linker (r_1 and r_2, respectively) during precipitation polymerization, where the reactivity ratio is a measure of the propensity of a monomer to propagate by reacting with itself or a different monomer in the synthetic mixture. For instance, microgels cross-linked with *N,N'*-methylenebis(acrylamide) (BIS) typically show a radial distribution of cross-links within the particle, with the highest cross-linker concentrations residing at the microgel interior.[21, 24] This uneven incorporation of BIS has been attributed to a high reactivity ratio for the cross-linker relative to the monomer (e.g. acrylamide $r_1 = 0.57$, BIS $r_2 = 3.36$).[25] The divergent microgel structures used in this study were also likely caused by differential incorporation of DHEA in microgels composed of NIPAm relative to those composed of

NIPMAm. This differential incorporation likely arises from a combination of two factors. First, NIPAm has been reported to undergo polymerization faster than NIPMAm, which would result in differential reaction rates between the different monomers and the cross-linker.[26] Secondly, DHEA is a more hydrophilic molecule than BIS, which would result in poorer incorporation of DHEA-rich polymer segments into the hydrophobic polymer globules during particle growth; this effect has been observed for a number of other co-polymer microgels synthesized by precipitation polymerization.[26-27] We have previously found, for example, that DHEA tends to be inefficiently incorporated into pNIPAm microgels during precipitation polymerization as compared with BIS, resulting in a more loosely cross-linked network in the case of DHEA.[14]

Thus, the heterogeneous mass distribution found for pNIPAm-DHEA microgels may be attributed to preferential incorporation of the NIPAm monomer over DHEA during synthesis due to both the rapid homopropagation of NIPAm and the higher solubility of any DHEA rich-segments. As discussed previously, there are additional features of pNIPAm polymerization that can contribute to microgel heterogeneity (i.e. self-cross-linking), which might serve to exacerbate the observed structural differences. As shown **Scheme 5.1**, pNIPAm microgels were of significantly lower density than pNIPMAm spheres, suggesting a lower overall cross-linking density. This result, combined with the presence of remnant spheres following erosion, suggests that self-cross-linking contributes a significant fraction of cross-linking sites throughout the structure. In contrast, spheres composed of pNIPMAm showed significantly greater density and a smooth sphere topology. This was likely the result of even incorporation of reactants during synthesis, as NIPMAm reacts more slowly, which would permit a more statistically random incorporation of the DHEA cross-linker. The more random co-polymers will also be less likely to suffer from poor incorporation due to solubility issues, as described previously for polyelectrolyte copolymer microgel synthesis.[27]

5.4 Conclusions

In summary, analysis of microgel network deconstruction using the in situ monitoring method revealed critical physicochemical differences between the particles. Although the two microgels were produced under similar synthetic conditions and were of comparable dimensions (i.e. their r_{rms} values), their reaction kinetics and the products of erosion were very different. Importantly, the presence of intrinsic self-cross-linking sites within pNIPAm-DHEA microgels limited the dissolution of the network. This result suggests that the formation of completely degradable pNIPAm microgels may require alternative synthetic strategies that limit parasitic chain transfer. The investigation described in this chapter was informative as we pursue the synthesis and application of thermoresponsive and degradable hydrogel particles, enabling a detailed assessment of microgel erosion. We anticipate that similar methods will assist in the study of other micro/nanoparticles, where rapid response events may enable specific biomedical applications.

5.5 References

1. Raemdonck, K.; Demeester, J.; De Smedt, S., Advanced nanogel engineering for drug delivery. *Soft Matter* **2009,** *5* (4), 707-715.

2. Nayak, S.; Lyon, L. A., Soft Nanotechnology with Soft Nanoparticles. *Angew. Chem., Int. Ed.* **2005,** *44* (47), 7686-7708.

3. Oh, J. K.; Drumright, R.; Siegwart, D. J.; Matyjaszewski, K., The development of microgels/nanogels for drug delivery applications. *Prog. Polym. Sci.* **2008,** *33* (4), 448-477.

4. Dickerson, E.; Blackburn, W.; Smith, M.; Kapa, L.; Lyon, L. A.; McDonald, J., Chemosensitization of cancer cells by siRNA using targeted nanogel delivery. *BMC Cancer* **2010,** *10* (1), 10.

5. Murthy, N.; Xu, M.; Schuck, S.; Kunisawa, J.; Shastri, N.; Fréchet, J. M. J., A macromolecular delivery vehicle for protein-based vaccines: Acid-degradable protein-loaded microgels. *Proc. Natl. Acad. Sci. U. S. A.* **2003,** *100* (9), 4995-5000.

6. De Geest, B.; Déjugnat, C.; Sukhorukov, G.; Braeckmans, K.; De Smedt, S.; Demeester, J., Self-Rupturing Microcapsules. *Adv. Mater. (Weinheim, Ger.)* **2005,** *17* (19), 2357-2361.

7. Tamada, J. A.; Langer, R., Erosion kinetics of hydrolytically degradable polymers. *Proc. Natl. Acad. Sci. U. S. A.* **1993,** *90* (2), 552-556.

8. Cedervall, T.; Lynch, I.; Lindman, S.; Berggård, T.; Thulin, E.; Nilsson, H.; Dawson, K. A.; Linse, S., Understanding the nanoparticle–protein corona using methods to quantify exchange rates and affinities of proteins for nanoparticles. *Proc. Natl. Acad. Sci. U. S. A.* **2007,** *104* (7), 2050-2055.

9. Lundqvist, M.; Stigler, J.; Elia, G.; Lynch, I.; Cedervall, T.; Dawson, K. A., Nanoparticle size and surface properties determine the protein corona with possible implications for biological impacts. *Proc. Natl. Acad. Sci. U. S. A.* **2008,** *105* (38), 14265-14270.

10. Huang, X.; Misra, G. P.; Vaish, A.; Flanagan, J. M.; Sutermaster, B.; Lowe, T. L., Novel Nanogels with Both Thermoresponsive and Hydrolytically Degradable Properties. *Macromolecules* **2008,** *41* (22), 8339-8345.

11. South, A. B.; Lyon, L. A., Direct Observation of Microgel Erosion via in-Liquid Atomic Force Microscopy. *Chem. Mater.* **2010,** *22* (10), 3300-3306.

12. Smith, M. H.; South, A. B.; Gaulding, J. C.; Lyon, L. A., Monitoring the Erosion of Hydrolytically-Degradable Nanogels via Multiangle Light Scattering Coupled to Asymmetrical Flow Field-Flow Fractionation. *Anal. Chem.* **2009,** *82* (2), 523-530.

13. Goh, S. L.; Murthy, N.; Xu, M.; Fréchet, J. M. J., Cross-Linked Microparticles as Carriers for the Delivery of Plasmid DNA for Vaccine Development. *Bioconjug. Chem.* **2004,** *15* (3), 467-474.

14. Nayak, S.; Gan, D.; Serpe, M.; Lyon, L., Hollow Thermoresponsive Microgels. *Small* **2005,** *1* (4), 416-421.

15. Singh, N.; Lyon, L. A., Au Nanoparticle Templated Synthesis of pNIPAm Nanogels. *Chem. Mater.* **2007,** *19* (4), 719-726.

16. Schild, H. G., Poly(N-isopropylacrylamide): experiment, theory and application. *Prog. Polym. Sci.* **1992,** *17* (2), 163-249.

17. Tang, Y.; Ding, Y.; Zhang, G., Role of Methyl in the Phase Transition of Poly(N-isopropylmethacrylamide). *J. Phys. Chem. B* **2008,** *112* (29), 8447-8451.

18. Metz, N.; Theato, P., Synthesis and Characterization of Base Labile Poly(N-isopropylacrylamide) Networks Utilizing a Reactive Cross-Linker. *Macromolecules* **2008,** *42* (1), 37-39.

19. Andersson, M.; Wittgren, B.; Wahlund, K.-G., Accuracy in Multiangle Light Scattering Measurements for Molar Mass and Radius Estimations. Model Calculations and Experiments. *Anal. Chem.* **2003,** *75* (16), 4279-4291.

20. Thielking, H.; Roessner, D.; Kulicke, W.-M., Online Coupling of Flow Field-Flow Fractionation and Multiangle Laser Light Scattering for the Characterization of Polystyrene Particles. *Anal. Chem.* **1995,** *67* (18), 3229-3233.

21. Stieger, M.; Richtering, W.; Pedersen, J. S.; Lindner, P., Small-angle neutron scattering study of structural changes in temperature sensitive microgel colloids. *J. Chem. Phys.* **2004,** *120* (13), 6197-6206.

22. Saunders, B. R., On the Structure of Poly(N-isopropylacrylamide) Microgel Particles. *Langmuir* **2004,** *20* (10), 3925-3932.

23. Gao, J.; Frisken, B. J., Cross-Linker-Free N-Isopropylacrylamide Gel Nanospheres. *Langmuir* **2003,** *19* (13), 5212-5216.

24. Wu, X.; Pelton, R. H.; Hamielec, A. E.; Woods, D. R.; McPhee, W., The kinetics of poly(<i>N</i>-isopropylacrylamide) microgel latex formation. *Colloid & Polymer Science* **1994,** *272* (4), 467-477.

25. Baselga, J.; Llorente, M. A.; Nieto, J. L.; Hernández-Fuentes, I.; Piérola, I. F., Polyacrylamide networks. sequence distribution of crosslinker. *Eur. Polym. J.* **1988,** *24* (2), 161-165.

26. Duracher, D.; Elaïssari, A.; Pichot, C., Preparation of poly(N-isopropylmethacrylamide) latexes kinetic studies and characterization. *Journal of Polymer Science Part A: Polymer Chemistry* **1999,** *37* (12), 1823-1837.

27. Hu, X. B.; Tong, Z.; Lyon, L. A., Synthesis and physicochemical properties of cationic microgels based on poly(N-isopropylmethacrylamide). *Colloid Polym. Sci.* **2011,** *289* (3), 333-339.

CHAPTER 6

TUNABLE ENCAPSULATION OF PROTEINS WITHIN CHARGED MICROGELS

Adapted from

Smith, MH; Lyon, LA. *Macromolecules* 2011, 44, (20), 8154-8160.

6.1 Introduction

Effective delivery systems are greatly needed for therapeutic proteins, which are characterized by several undesirable physicochemical properties that limit their widespread medical use. For example, the bioavailability of proteins is generally poor since they are unable to cross many biological membranes. Unlike more stable compounds, protein drugs are highly susceptible to loss of their pharmacologically-active structure (e.g. by proteolysis, oxidation, deamidation), decreasing their therapeutic activity.[1] Proteins are also sensitive to their local environment, being prone to aggregation, adsorption, or denaturation.[2] To overcome the shortcomings of protein drugs, hydrogel particles (e.g. micro- or nanogels) may be used to encapsulate, protect, and subsequently release the agents at disease sites.[3-4] Hydrogels are composed of loosely cross-linked hydrophilic polymers, yielding a low-density structure that can be used to encapsulate proteins. Importantly, using microgels and nanogels scales the favorable encapsulation properties down to the sub-cellular level, suggesting the potential for cellular targeting of therapeutics (the physicochemical properties of nanogels and microgels are discussed in more detail in Chapter 1).

Several researchers have examined the encapsulation of therapeutic peptides and proteins within hydrogels.[1, 5-12] In previous studies, protein loading was shown to depend on the physicochemical properties of the gel (e.g. cross-link density, charge, hydrophilicity) and the strength of protein-polymer interactions within the polymer network. However, the majority of reports have focused on encapsulation within gels of macroscopic dimensions. Whereas macroscopic gels show promise for certain delivery routes (e.g. implantable drug depots, topical application, oral administration), the smaller dimensions of colloidal particles enables access to regions of the body inaccessible to their larger counterparts. For example, we and others are pursuing microgels and nanogels as drug delivery vehicles for siRNA and therapeutic proteins (Chapter 3).[9, 13-16] In work described in this Chapter, the loading of cationic proteins within anionic microgels (<0.7 μm in diameter) was systematically investigated, assessing the relationships between microgel charge and binding stoichiometry. Encapsulation was measured by monitoring the changes in microgel molar mass and radius upon protein loading via MALS.

6.2 Experimental Section

6.2.1 Materials

All reagents were purchased from Sigma-Aldrich (St Louis, MO) and used as received, unless otherwise noted. The monomer *N*-isopropylacrylamide (NIPAm) was recrystallized from hexanes (VWR international, West Chester, PA) and dried in vacuo prior to use. Reagents *N,N'*-methylenebisacrylamide (BIS), sodium dodecyl sulfate (SDS), and ammonium persulfate (APS) were all used as received. Water used in all reactions and particle purifications was purified to a resistance of 18 MΩ (Barnstead E-Pure system), and filtered through a 0.2-μm filter to remove particulate matter.

6.2.2 Microgel Synthesis

Particle syntheses were performed via surfactant-stabilized precipitation polymerization, using a modified approach to that previously reported.[17] The total monomer concentration of all reactions was maintained at 100 mM with a total reaction volume of 100 mL. A series of microgels were synthesized with varying AAc content (30%, 20%, 10%, and 0% of the total monomer concentration) with identical BIS content (2%). The concentrations of NIPAm monomer were adjusted accordingly to achieve the desired total monomer content. Reactions were performed by first dissolving NIPAm, AAc, and BIS in distilled, deionized water. A small amount of SDS was added to each suspension to yield a total surfactant concentration of 1 mM. Monomer solutions were filtered through 0.2 μm Acrodisc syringe filters and subsequently added to 200 mL three-neck round-bottom flasks. Once equilibrated at 70 °C, the reaction mixtures were purged with N_2 for 1 hr while stirring (400 RPM). The polymerizations were initiated by delivering a 1.0 mL aliquot of 0.100 M APS solution by pipette. All reactions were allowed to proceed for 24 hours under an N_2 blanket while continuously stirring. Once cooled, reaction products were filtered through 0.8 μm Acrodisc syringe filters and purified via repeated ultracentrifugation and resuspension in distilled, deionized water.

6.2.3 Microgel Characterization

The *Mw* and *dn/dc* values of all microgels were determined via the Calypso syringe pump system (Wyatt Technology Corporation, Santa Barbara, CA), equipped with MALS and dRI detection. A diagram of the instrument configuration and the principle employed to characterize the *Mw* and r_{rms} of particles is described in Chapter 2. Multiangle light scattering was performed using the DAWN-EOS (Wyatt Technology Corporation, Santa Barbara, CA) equipped with a temperature-regulated K5 flow cell with a GaAs laser light source (λ = 685 nm). Data collection and subsequent light scattering analysis was performed using the Astra software Version 5.3.4.14 (Wyatt Technology Corporation, Santa Barbara, CA). Accurate measurements of microgel molar

mass require the characterization of the *dn/dc*. Differential refractive index analysis was performed via composition-gradient static light scattering using the Calypso and Optilab rEX system, equipped with an LED light source (λ = 690 nm). The diffusion coefficient values of particles were measured via DLS. DLS experiments were performed at a 90° scattering angle using a Protein Solutions DLS (Wyatt Technology Corporation, Santa Barbara, CA). The r_h values were calculated from measured diffusion coefficients through the Stokes-Einstein relation ($r_h = kT / 6\pi\eta D$), where D is the diffusion coefficient, k is Boltzmann's constant, η and T are the solution viscosity and temperature, respectively. Microgel electrophoretic mobility values (v_E) were determined using a Malvern Zetasizer Nano. The ζ-potential (ζ) values were derived from the Smoluchowski relation ($\zeta = v_E \eta / \varepsilon_0 \varepsilon$), where η is the solution viscosity, ε_0 is the relative dielectric constant, and ε is the electrical permittivity). It should be noted, however, that the ζ-potential is only applicable to microgels in a semi-quantitative manner, since no well-defined slipping plane exists between the microgel surface and the medium. Additionally, most of the charges in the microgels are buried, and contribute only fractionally to the calculated ζ-potential.

6.2.4 Protein Binding Analysis

Protein loading was quantified in this work via MALS. MALS is frequently employed to measure the root-mean-square radius (r_{rms}) and weight-average molar mass (*Mw*) of polymers. The principles employed in MALS measurements have been described in detail in Chapter 2 and elsewhere.[18] For accurate measurement of *Mw*, the differential refractive index increment (*dn/dc*) was measured for all microgels in pH 7 phosphate buffer. The *dn/dc* value is an important factor in accurate molar mass determination, being a component of the optical constant *K* in Eq. 1, and is dependent on

solvent conditions. Thus, the *dn/dc* values of microgels were determined in several different ionic strength environments and in the presence of cytochrome c.

For estimations of protein loading via light scattering, the overall change in *Mw* must be approximated for microgels in the presence or absence of protein. However, it is important to note that changes in particle swelling from loading introduces error into the approximation of M_w, where an increase in polymer segment density causes an increase in the intensity of scattering and thus the calculated change in molar mass. In order to compensate for this error, one may simply account for the overall change in particle volume in the loaded and unloaded states to more accurately estimate an overall change in M_w from binding via Equation 6.1.

$$dMw = \left(M_{loaded} - Mw_{unloaded}\right)\left(1 - \frac{V_{loaded}}{V_0}\right)$$

Eq. 6.1.

where V_0 is the volume of the microgel in the absence of protein and V_{loaded} is the volume of the microgel in the presence of the macromolecule. The validity of this approach was investigated in this work by comparing the measured loading via light scattering with offline methods (i.e traditional centrifugation/supernatant assay methods) and by comparing the measured values with reported loading capacities for similar hydrogels in the literature (described below in the Discussion section).

Solutions of microgels were prepared by diluting a purified stock of particles to a concentration of 1.50 μg/mL, 0.86 μg/mL, 0.663 μg/mL, or 1.82 μg/mL for 30 mol%, 20 mol%, 10 mol% and 0 mol% AAc microgels, respectively in pH 7.0 phosphate (10 mM, ionic strength = 20 mM). All buffers were filtered through 0.1 μm syringe filters prior to use. In a typical measurement, a baseline was first measured by delivering buffer alone through syringe S1 of the delivery system (from reservoir R1) (**Scheme 2.6**). Microgel solutions (loaded in reservoir R2) were subsequently introduced using the computer-controlled tri-syringe dispenser. The Calypso software enables programmable control

over reactant concentrations through the volume and rate of syringe flow. For reported microgel *Mw* and r_{rms} values in this work, particles were diluted to 50% concentration by dispensing and mixing the microgel solutions (S2) with buffer (S1). Scattering data was collected at 15 angles (0.5 s collection interval) and the resultant scattering curves were interpreted using the ASTRA software.

Measurement of microgel-protein interactions at a single concentration of cyt c was performed by dissolving the protein to a concentration of 48 μM in pH 7.0 phosphate buffer (10 mM, ionic strength = 20 mM). Protein solutions were filtered through 0.1 μM syringe filters to remove any particulate matter. The final concentration of protein stock was verified through differential refractometry. A baseline scattering signal was first measured by delivering cyt c (loaded in syringe S3) with buffer (loaded in syringe S1), resulting in 50% dilution ([cyt c] = 24 μM). After baseline measurement, the previously described microgel stock solutions (loaded in syringe S2) were administered with cytochrome c (syringe S3), diluting both reactants to 50% stock concentration. The *Mw* and r_{rms} of each particle type was measured at equilibrium via MALS, subtracting the baseline light scattering contribution from the protein alone. In an investigation of the effect of ionic strength on binding, the buffer used in microgel and protein stock preparation was replaced with pH 7.0 phosphate (10 mM) with varying salinity (ionic strength range of 20 – 150 mM).

Traditional centrifugation/supernatant assay methods were used to validate the light scattering approach for binding measurements. Solutions were prepared at 24 μm cyt c and varying 30 mol% AAc microgel concentrations (3.7×10^{-4} – 1.7×10^{-5} g/mL polymer) in pH 7.0 phosphate buffer (10 mM, ionic strength = 20 mM). Microgels were sedimented at 50,000 RPM (RCF = 136,000 x g) for 15 min using an Optilab Preparative Ultracentrifuge (Beckman Coulter, USA). Supernatant solutions were collected and assayed for protein concentration via standard curve using a UV-1601 spectophotometer (Shimadzu Corporation, Kyoto, Japan). Protein concentrations in the supernatant were

used to calculate the mass of bound cyt c per gram of polymer, enabling estimation of the polyelectrolyte capacity for the microgel (PC = g protein/ 1 g polymer). It is important to note that the polymer concentrations used in this assay are much greater than those employed in light scattering analysis. Thus, the *PC* value for microgels was estimated using the concentration series to extrapolate the *PC* value to lower polymer concentrations (~0.7 μg/mL).

6.2.5 Microgel Size Analysis

Investigations of microgel r_h by DLS were performed offline at particle concentrations of 0.04 mg/mL, 0.04 mg/mL, 0.01 mg/mL, and 0.005 mg/mL for 30 mol%, 20 mol%, 10 mol %, and 0 mol% AAc microgels, respectively. Samples were prepared by diluting a concentrated, purified stock of particles to the indicated concentration in pH 7.0 phosphate buffer. Microgel r_h was measured at 25 ºC using the Dynapro DLS. The ζ-potential of microgels was measured at the same stock concentrations and in identical buffers. In an investigation of microgel binding, 30 mol% AAc microgels were diluted in a concentrated protein stock ([cyt c] = 24 μM). The diffusion coefficients for the microgels at varying ionic strength were measured, enabling calculation of particle r_h in response to protein binding.

6.2.6 Titrations

Potentiometric titrations were performed to measure acid incorporation into microgels using a Corning pH Meter 430 (Corning Incorporated, NY). Microgels were diluted to a total concentration of 1 mg/mL and a volume of 20.00 mL in distilled, deionized water. Samples were titrated with 0.11 M NaOH under an N_2 purge while stirring at 22 ºC. Measurements of solution pH were made after 300 s equilibration after each addition of titrant.

6.3 Results and Discussion

To systematically investigate the role of hydrogel charge in protein encapsulation, a series of poly(*N*-isopropylacrylamide-*co*-acrylic acid) microgels was synthesized, loosely cross-linked with *N,N'*-methylenebisacrylamide (BIS, 2 mol%). Acrylic acid (AAc) was chosen as a comonomer since it incorporates quantitatively into pNIPAm microgels during precipitation polymerization, as reported previously.[19] In order to tune the acid content, microgels were synthesized by varying the mol% AAc added during precipitation polymerization. The set of synthesized microgel particles had similar weight-average molar mass (M_w) values, densities (ρ), and topological features (**Table 6.1**).

Table 6.1. Physical properties of microgels synthesized via precipitation polymerization.[1]

AAc Content (mol%)	r_h, DLS (nm)	r_{rms}, MALS (nm)	M_w (g/mol)	ρ (g/mL)	ζ-potential (mV)
30	358 ± 3	230.5 ± 0.5	$2.60 \pm 0.02 \times 10^{9}$	$2.26 \pm 0.01 \times 10^{-2}$	-32.9 ± 0.8
20	327 ± 4	187.5 ± 0.2	$1.62 \pm 0.01 \times 10^{9}$	$1.89 \pm 0.01 \times 10^{-2}$	-26.6 ± 0.5
10	229 ± 4	138.0 ± 0.3	$9.41 \pm 0.01 \times 10^{8}$	$3.10 \pm 0.01 \times 10^{-2}$	-16.4 ± 0.7
0	121 ± 1	76 ± 2	$2.91 \pm 0.01 \times 10^{8}$	$6.4 \pm 0.1 \times 10^{-2}$	-0.7 ± 0.7

[1]Error represents ± one standard deviation of measurements in replicate (n = 4).

The mass distribution within the spheres may be inferred through the ratio of the r_{rms} and the r_h values.[20] Ratios observed in this work ($r_{rms}/r_h < 0.7$) are indicative of a radially heterogeneous network topology. Heterogeneity in the microgel structure is imparted through non-uniform cross-linker incorporation during precipitation polymerization; particles prepared in this fashion typically have greater cross-linking within their interior than the periphery.[21] Additionally, the microgels have a low density, a common characteristic for superabsorbent hydrogels. The density was calculated from the mass of a single microgel per the measured volume (from DLS analysis). Acid incorporation was quantified via potentiometric titration and was found to scale

quantitatively with the moles of AAc included in synthesis for 30 mol% (2.9 x 10^{-3} mol COOH/g polymer), 20 mol% (1.9 x 10^{-3} mol COOH/g polymer), and 10 mol% AAc (1.1 x 10^{-3} mol COOH/g polymer) particles (**Figure 6.1**).

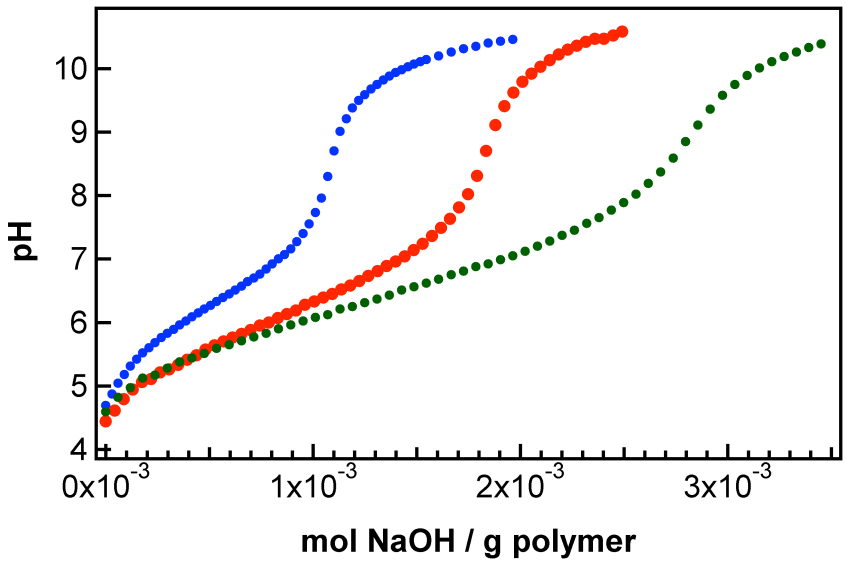

Figure 6.1. Potentiometric titrations of microgels for the measurement of total acid content. Particles were synthesized to contain 30 mol% (green), 20 mol% (red), and 10 mol%(blue) AAc comonomer.

The ζ-potential for all spheres was measured to determine the influence of the AAc content on particle ionization at neutral pH. The magnitude of ζ-potential was found to increase with increasing amounts of AAc included during synthesis, as reported in **Table 6.1**.

Protein binding was measured for the charged microgels in the presence of cytochrome c (cyt c). The structure and charge distribution of cyt c have been explored in-depth,[22] whereas the binding characteristics of the protein to macroscopic hydrogels has also been reported.[6-7] The protein is a small, highly water soluble, heme protein with a hydrodynamic diameter of 3.5 nm (1.75 nm r_h, by DLS).[22] The heme ligand is located in a lysine-rich region of the protein, imparting a positive charge to the macromolecule at pH 7.[23] It has been hypothesized that this front face electrostatically guides the

cytochrome complex towards negatively charged proteins and lipids *in vivo*. The protein has a net charge of +9.3 (pI = 10.1, Mw = 12,327 Da) at neutral pH.[23]

MALS was employed to quantitatively determine the relative cyt c binding to microgels of varying AAc content. The *Mw* values of dilute microgels in buffer alone (0.332 – 0.910 µg/mL) were compared to the *Mw* measured in the presence of 24 µM cyt c (~300 µg/mL) (**Figure 6.2**).

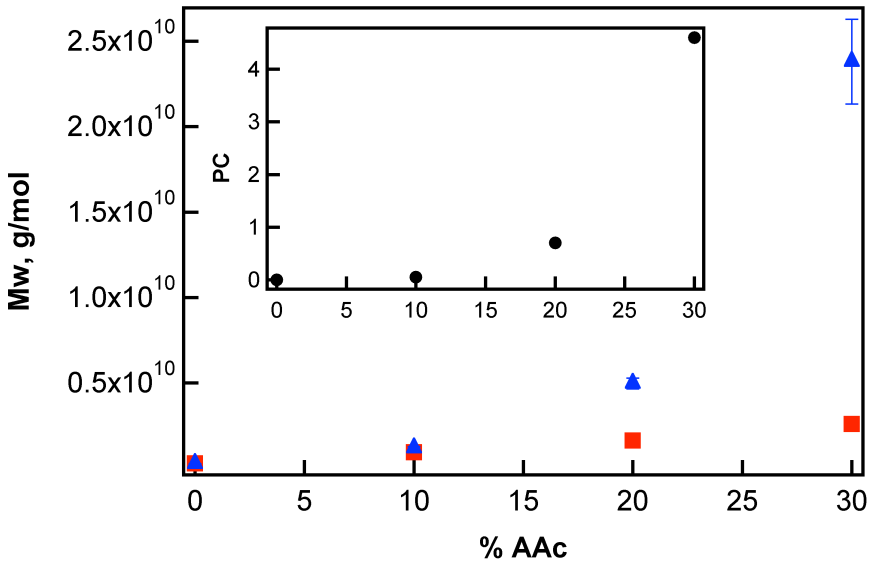

Figure 6.2. The AAc content of microgels influences binding to cyt c, resulting in an increase in apparent microgel *Mw* in the presence (blue, 24 µM protein) versus absence (red) of cyt c. Inset: calculated polyelectrolyte capacity (PC) for microgels. Error bars represent one standard deviation about the mean of measurements performed in triplicate.

An increase in M_w was observed for microgels containing AAc in the presence of cyt c (**Figure 6.2**). Notably, the M_w of 30 mol% AAc microgels increased by approximately an order of magnitude, indicating a large amount of cyt c loading within the hydrogel network. The loading results in a significant change in shape of the Debye plot, which suggests a change in particle swelling through loading (**Figure 6.3**).

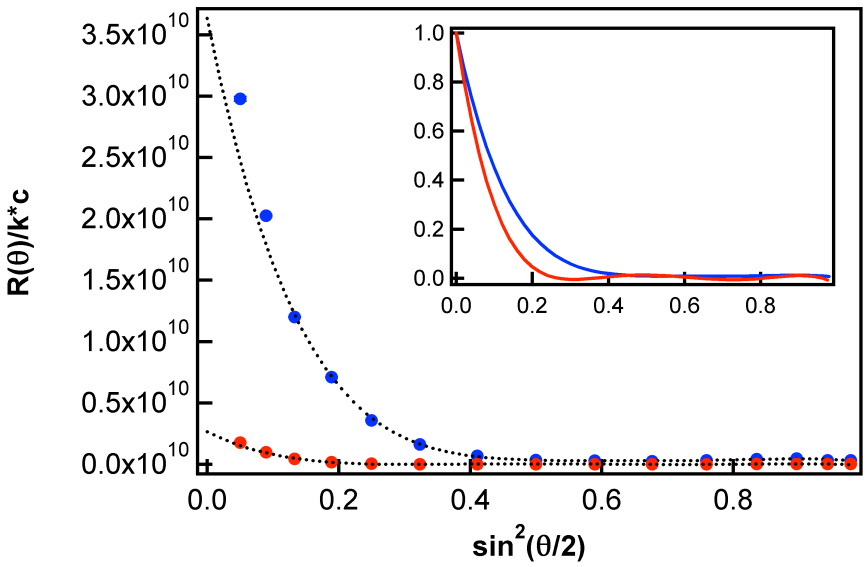

Figure 6.3. Example Debye plots for 30 mol% microgels (red) and for those microgels in the presence of 24 μM cytochrome c (blue) with polynomial fitting of the angle-dependent data shown (dotted black line). Inset: normalized polynomial fits for the particles in the bound (blue) and unbound (red) state.

The loading results in a decrease in particle radius (r_h and r_{rms}). The r_{rms} of microgels containing 30 mol% AAc decreased from 229 nm to 174 nm from the empty to loaded states, respectively (pH 7.0, I = 20 mM, [cyt c] = 24 μM). This size change correlates to a volume decrease of ~55% during the binding event. A similar volume decrease was observed in the measurement of r_h by DLS under the same solution conditions (~53%).

Microgels interact with oppositely charged cyt c via polyelectrolyte interactions. Coulombic forces between the microgel and cyt c results the formation of a polymer-protein complex, releasing counterions associated with the polymer and protein. Entropy is gained through counterion release, providing a net gain in free energy which drives the formation of a cross-linked protein-polyelectrolyte complex (**Scheme 6.1**).[7]

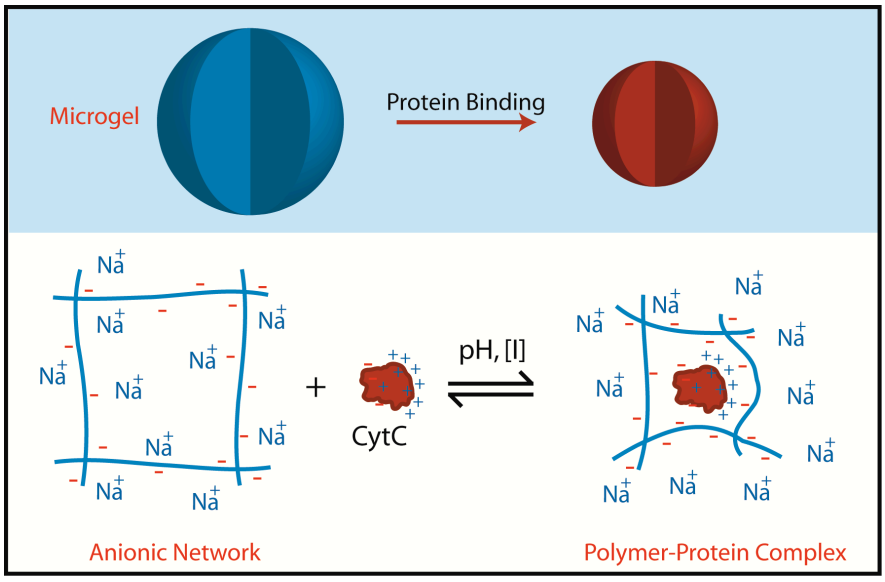

Scheme 6.1. Proposed interaction of microgels with oppositely charged cyt c.

Using the scattering data, the polyelectrolyte capacity (*PC*) of the polymer may be calculated (**Figure 6.2,** inset**)**. The *PC* is a frequently used metric for the loading capacity of macroscopic hydrogels reported in the literature.[7] Conventionally, the amount of loaded material is measured by weighing the dehydrated bulk gels (equation 6.2).

Eq. 6.2
$$PC = \frac{\text{g of protein}}{\text{1 g of polymer}}$$

Using MALS, the *PC* is instead determined through the ratio of the mass of loaded protein per the mass of a single sphere.

Eq. 6.3.
$$PC_{MALS} = \frac{\text{mass of protein loaded}}{\text{mass of a single microgel}} = \frac{M_{tot,cytc}}{Mw_{unbound} * (1/N_A)}$$

where $M_{tot,cytc}$ is the total mass of protein per microgel, $Mw_{unloaded}$ is the molar mass of native microgels (without protein), and N_A is Avagadro's number. The $M_{tot,cytc}$ was determined through

Eq. 6.4. $$M_{tot,cytc} = \frac{dMw}{Mw_{cytc}} * \frac{1}{N_A} * Mw_{cytc} = \frac{dMw}{N_A}$$

where dMw is the overall change in molar mass as described by equation 2 of the main text. Combining Eq. S2 with Eq. S3 and simplifying yields Eq. 6.5. for calculating PC.

Eq. 6.5. $$PC_{MALS} = \frac{dMw}{Mw_{unloaded}}$$

To validate the MALS method for the measurement of *PC* in this fashion, traditional centrifugation/supernatant recovery assay methods were used to measure the fraction of protein bound under similar conditions (pH 7.0, [cytc] = 24 μm). As described in the *Methods*, microgels at varying concentration were mixed with the protein and subsequently separated by centrifugation. The concentration of bound cyt c was quantified by analysis of the supernatant by UV-vis (**Figure 6.4**).

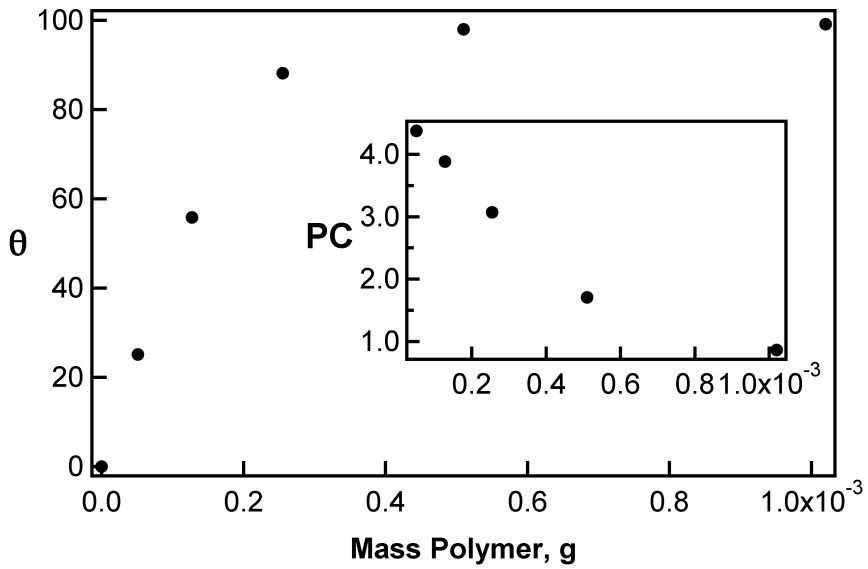

Figure 6.4. Traditional centrifugation/supernatant analysis methods to estimate the fraction of bound protein (θ) for 30 mol% AAc microgels at varying polymer concentrations in pH 7.0 and in the presence of 24 μM cyt c. Polyelectrolyte capacity values (inset) were calculated from the concentration of bound protein per mass of polymer.

The *PC* was found to converge to a value of ~4.4 for the particles in the presence of excess cyt c. Using the *MALS* approach, the *PC* was found to be ~4.5 for the 30 mol% AAc microgels, which is in good agreement with traditional centrifugation/supernatant assay methods for measuring encapsulation. To further validate the MALS method, the calculated *PC* for 30 mol% AAc microgels was compared with the *PC* values for macroscopic anionic hydrogels reported in the literature. The *PC* value varies significantly with the pH and the ionic strength of the medium. However, Kabanov et al. have reported *PC* values ranging from 13.2 – 16.5 for poly(acrylic acid) macroscopic gels under similar binding conditions to those reported in this work (pH 7, low ionic strength).[7] From the *PC* range reported by Kabanov (for AAc homopolymer gels), one would anticipate a *PC* value for 30 mol% AAc microgel to range from ~4.0 – 5.0. Our measured *PC* value for 30 mol% AAc microgels (~4.5) is thus in good agreement with the expected capacity of the hydrogels for protein.

Using MALS, loading was quantified for each particle in solutions of high protein concentration ([cytc] = 24 μM). For instance, the 30 mol% AAc microgels bind ~9.7 x 10^5 molecules of cyt c per sphere. Using the number of bound proteins and the volume of the microgel, we approximated the effective internal protein concentration to be ~17 mM (~210 g/L), which is a ~700-fold increase in the protein concentration relative to the 24 μM solution used for loading. The loaded concentration exceeds the solubility of cyt c in water (100 g/L at 25 ºC), which suggests that the microgel network facilitates solubilization of the protein. Microgels with lower AAc content loaded less cyt c: 20 mol% AAc microgels bound ~4.0 x 10^5 cyt c and 10 mol% AAc microgels bound ~1.0 x 10^4 cyt c per sphere. Those loading stoichiometries correspond to effective internal protein concentrations of ~4.0 mM and ~0.6 mM cyt c for 20 mol% and 10 mol% AAc particles, respectively. For particles synthesized without AAc, the MALS method was unable to detect a significant increase in light scattering in the presence of cyt c, which suggests minimal interaction with the protein.

Additional differences between particles were found by comparing the mole fraction (θ) of cytochrome c loaded per the total moles of acids in the microgel (θ = moles cyt c loaded / moles AAc available). Whereas the *PC* value reflects the total capacity of the polymer for protein, the value of θ reflects the capacity of the microgel to interact with the protein on a per site basis. For example, particles with 30 mol% AAc bind a significantly greater fraction of charged groups (θ = 0.13) than either the 20 mol% (θ = 0.05) or 10 mol% AAc microgels (θ = 0.01). In other words, the proteins are able to access a much larger number of the available charges within the high acid content microgels. The higher loading capacities for 30 mol% AAc microgels likely result from the increased network swelling, caused by the Donnan effect.[19, 24] The higher charge density in those microgels increases swelling pressure in the network. Gel swelling yields a lower polymer segment density in the network and greater gel porosity, yielding a higher loading capacity for cyt c. In the case of the lower acid content particles, it

appears that the decrease in charge density dramatically decreases the accessibility of those charges to protein binding. This effect was especially apparent for 10 mol% AAc microgels ($\theta = 0.01$), where the amount of protein binding (**Figure 6.2)** is commensurate with a sub-monolayer of the cyt c on the particle surface. The low binding stoichiometry suggests limited access of the protein to the interior polymer network in the case of low acid-content microgels. It may be the case that the initial protein binding events are surface localized, causing a condensation of the particle periphery, which limits subsequent protein binding within the microgels. Conversely, for the higher acid content microgels, the initial protein binding events may occur deeper within the microgel or may cause less network condensation, thereby presenting less of a steric hindrance to subsequent binding events.

Previous reports have described an anti-cooperative mechanism for binding between microgels and cationic molecules, being strongly dependent on the physicochemical properties of the loaded macromolecule (e.g. charge, hydrophobicity, molar mass).[15-16, 20] For example, the uptake of lysozyme (a small, cationic protein similar to cyt c) results in condensation of the polymer network in the periphery of particles, forming a collapsed shell and a semi-swollen particle interior.[11] Protein-protein interactions cause lysozyme to aggregate in the shell, resulting in a biphasic distribution of loaded constituents at the final stages of loading (with the greatest protein concentration in the particle periphery). Malmsten and coworkers noticed a similar effect in loading cationic peptides into charge microgels, where hydrophobic interactions between peptides greatly influences the resulting distribution of macromolecules in the microgels.[25] Although cytochrome c has been reported to form a collapsed polymer shell during loading, a recent study has shown that the high stability of the molecule (by protein-protein repulsion) enables diffusion through the collapsed shell during loading, eventually resulting in a uniform distribution of protein throughout the microgel at equilibrium.[6] Guided by the literature precedent, we anticipate that the highly acidic

microgels (30 mol% AAc) likely load cytochrome c with a similar mechanism as their macroscopic counterparts, resulting in a uniform distribution of proteins within the structure (**Scheme 6.1**). However, the decreased accessibility of the charge groups within 20 mol% and 10 mol% AAc microgels (θ = 0.05 and 0.01, respectively) may suggest a different loading mechanism, where the decreased swelling of the particles limits loading within the microgel exterior. However, additional work is needed to verify this hypothesis.

The interaction of cyt c with polyanionic microgels results in a highly condensed polymer structure presumably due to the release of counterions and solvent from the network, causing an overall decrease in particle volume. The observed decrease in volume, coupled with the increase in particle molar mass, results in a density increase (**Figure 6.5**).

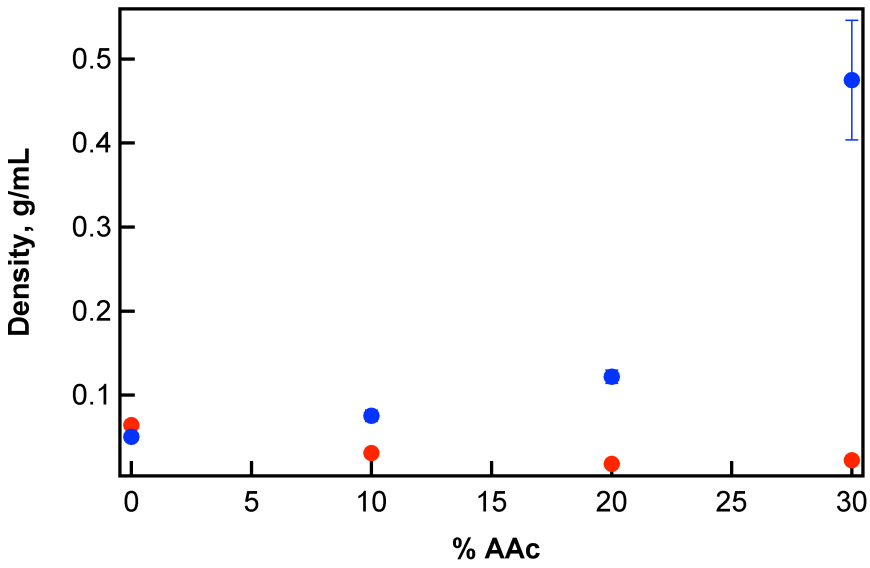

Figure 6.5. Influence of cyt c binding on density for loaded (blue, 24 μM) and unloaded (red) microgels. Density values for microgels were calculated through measurement of microgel volume and molar mass via DLS and MALS, respectively (pH 7.0, I = 20 mM, [CytC] = 24 μM).

For example, the density of 30 mol% AAc microgels increases ~20-fold in the presence of cyt c. For reference, the density of globular proteins typically ranges from 0.8-1.2 g/mL (density of cyt c = 0.9 g/mL). The microgel density increase is representative of a transition from of a porous, highly-swollen network (~0.02 g/mL), to a condensed, protein-rich material (~0.5 g/mL). This result may suggest that protein loading affects the modulus of the microgel particles. Others have described a strong relationship between particle shear modulus with the ionization of the network.[26] Protein loading and the occupancy of available charged groups may decrease network ionization, and thus decrease particle softness. This outcome may influence the deformability of particles in response to applied forces.

Under neutral pH conditions, AAc-functionalized microgels are ionized, and in the case of AAc containing pNIPAm microgels, have a uniform distribution of charges throughout the particle structure.[19] Conversely, cyt c is positively charged due to the presence of a lysine-rich region of the macromolecule (adjacent to the heme group). The mixing of microgels and cyt c under low ionic strength conditions results in microgel-protein association. However, the extent and strength of Coulombic interactions between polyanionic gels and cyt c is dependent on the solution composition, as reported for macroscopic hydrogels.[6-7, 11] For example, changes in pH or ionic strength modulate the swelling of charged hydrogels. These volume changes are primarily driven by the distribution of ions between the internal gel network and the external environment by the Donnan potential.[19, 24] This additional swelling pressure is thus dependent on the AAc content, pH, and the salt concentration in the medium. Additionally, as the ionic strength is increased, the strength of Coulombic interactions between ionized gel and the loaded protein is diminished as the charges become more screened.

To look more closely at this effect, the impact of solution ionic strength on protein loading was investigated for 30 mol% AAc microgels, which have the highest capacity for cyt c of the microgels studied here. For microgels in the absence of protein, a

decrease in particle r_h was measured with increasing ionic strength (20 – 100 mM) at neutral pH, as expected for polyanionic networks (**Figure 6.6**).

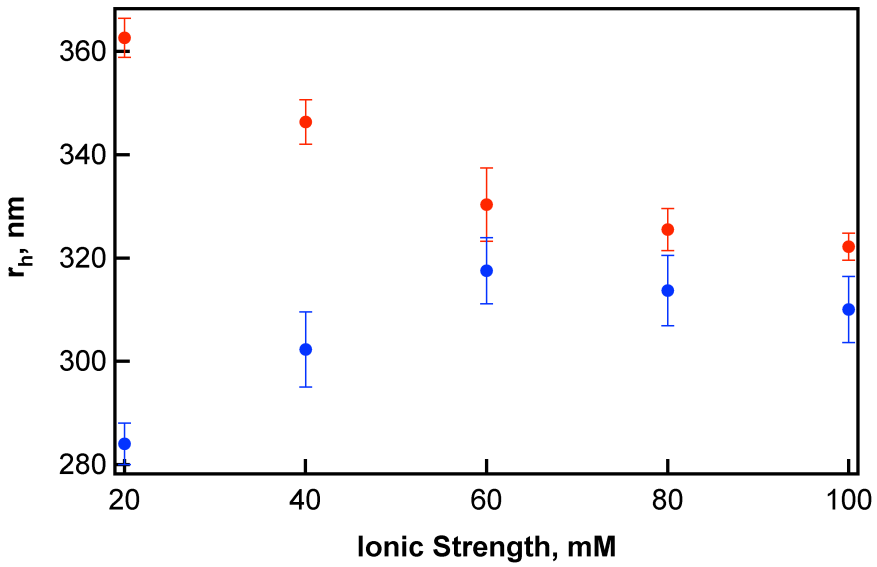

Figure 6.6. Influence of ionic strength on the hydrodynamic radius of loaded (blue, [cyt c] = 24 μM) versus unloaded (red) 30 mol% AAc microgels. All r_h values for were measured at identical particle concentrations in pH 7.0 phosphate buffer (10 mM) of varying salinity. Error bars represent one standard deviation about the means of several replicated measurements (n = 5).

The stoichiometry of protein binding to microgel is also affected by ionic strength; as the salt concentration is increased, the measured *Mw* of the complex decreases. At the highest ionic strengths studied (170 mM), the microgel *Mw* approaches a value that is similar to that measured for microgels in the absence of protein (**Figure 6.7**, green dotted line).

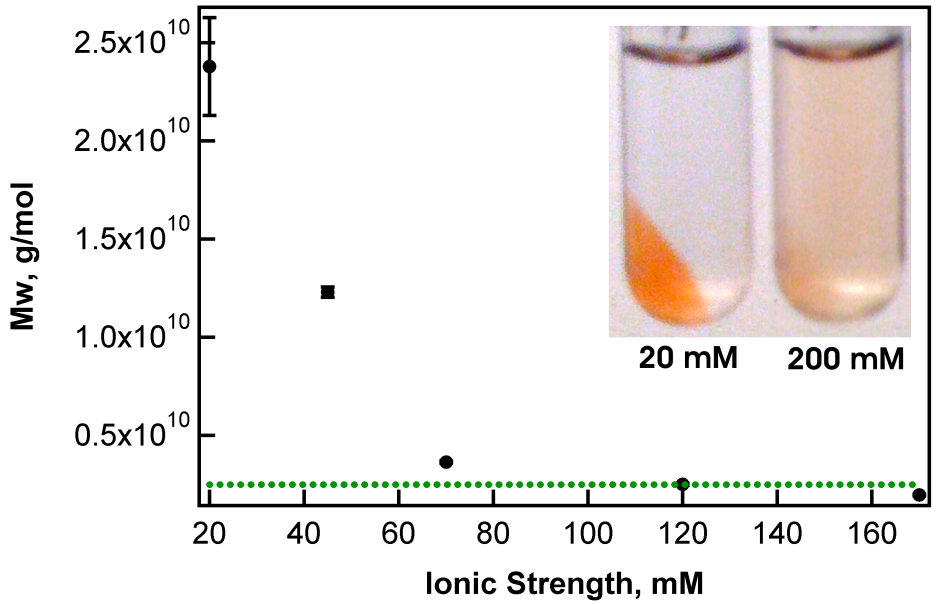

Figure 6.7 Influence of ionic strength on microgel-cyt c interactions. Increasing salinity results in a decrease in the measured *Mw* of 30 mol% AAc microgels. For reference, the *Mw* of unloaded microgels is shown (green dotted line). All measurements were made at neutral pH and at identical microgel and protein concentrations. Inset: visual observation of loading via mixing and separating microgels from free protein by centrifugation. Cyt c (red color) is localized with microgels in the pellet at low ionic strength (I = 20 mM).

The loading of microgels was also qualitatively observed by mixing 30 mol% microgels with cyt c and separating the bound and unbound fractions by centrifugation. Photographs were taken after centrifugation (**Figure 6.7**, inset). At low ionic strength, where charge screening is limited, cyt c is co-localized with particles in the pellet.

The decrease in protein loading at high ionic strength is likely caused by two factors, the change in swelling of the microgel network and charge screening between binding partners. As described earlier, entropy is gained through counterion release from binding cyt c, providing a net gain in free energy that drives the formation of a cross-linked protein-polyelectrolyte complex. As the salt concentration is increased, the total change in entropy experienced by the system during binding is diminished, making loading less favorable. Meanwhile, the Debye screening length is reduced at high ionic strength, decreasing the effective strength of Coulombic interactions. For microgels

composed of 30 mol% AAc, binding was not detected above 120 mM ionic strength. A similar trend has recently been reported for the interaction between polyanionic macrogels and oppositely charged peptides, where increasing ionic strength screened the Coulombic interactions between peptides bound to the gel.[25]

6.4 Conclusions

The physicochemical properties of microgels is altered through binding with various compounds, including polyelectrolytes,[27-28] polymers,[29] surfactants,[30] and small molecule compounds.[31] Namely, the adsorption or absorption of macromolecules affects swelling, density, charge and the stability of the polymer. In this chapter, we assessed cyt c loading into colloidal microgels by monitoring the properties of the particles (e.g. molar mass, radius) directly during encapsulation. Similar to their macroscopic counterparts,[6-7, 11] colloidal microgels load oppositely charged proteins via Coulombic interactions. The increase in particle M_w in the presence of cyt c was used to quantify the number and concentration of macromolecules within the particles. Microgels containing 30 mol% AAc were capable of loading extremely high concentrations of cyt c (~17 mM), beyond the solubility limit of the protein in aqueous media (8 mM, 25 ºC). Modulating AAc content was an effective means to tune binding stoichiometry; particles with greater AAc content showed the greatest capacity for loading. Microgels with low charge content (e.g. 10 mol% AAc) encapsulated a smaller fraction of proteins due to the decreased swelling and low porosity of those networks.

The detailed assessment of encapsulation in this chapter revealed import design parameters to consider as we pursue microgels and nanogels as peptide and protein delivery vehicles. For example, considerable changes in microgel morphology resulted from loading, where the density of the highly charged spheres (30 mol% AAc) increased ~20-fold. Decreased swelling during loading is likely to influence the modulus or "softness" of the particles, where previous reports have shown a strong relationship

between polyelectrolyte shear modulus and the ionization of the network.[26] The microgel softness is a critical property for the material in biomedical applications, affecting their behavior in confined environments.[32-33] The chapter also elucidated the effects of gel network structure on macromolecule encapsulation. Using network swelling and ionization as a tunable variable, future delivery vehicles may be designed with specific encapsulation and release properties for biomedical applications.

6.5 References

1. Bromberg, L. E.; Ron, E. S., Temperature-responsive gels and thermogelling polymer matrices for protein and peptide delivery. *Adv. Drug Delivery Rev.* **1998,** *31* (3), 197-221.

2. Antosova, Z.; Mackova, M.; Kral, V.; Macek, T., Therapeutic application of peptides and proteins: parenteral forever? *Trends Biotechnol.* **2009,** *27* (11), 628-635.

3. Raemdonck, K.; Demeester, J.; De Smedt, S., Advanced nanogel engineering for drug delivery. *Soft Matter* **2009,** *5* (4), 707-715.

4. Peppas, N. A.; Hilt, J. Z.; Khademhosseini, A.; Langer, R., Hydrogels in Biology and Medicine: From Molecular Principles to Bionanotechnology. *Adv. Mater.* **2006,** *18* (11), 1345-1360.

5. Bysell, H.; Malmsten, M., Visualizing the interaction between poly-L-lysine and poly(acrylic acid) microgels using microscopy techniques: Effect of electrostatics and peptide size. *Langmuir* **2006,** *22* (12), 5476-5484.

6. Johansson, C.; Hansson, P., Distribution of cytochrome c in polyacrylate microgels. *Soft Matter* **2010,** *6* (16), 3970-3978.

7. Kabanov, V. A.; Skobeleva, V. B.; Rogacheva, V. B.; Zezin, A. B., Sorption of Proteins by Slightly Cross-Linked Polyelectrolyte Hydrogels: Kinetics and Mechanism. *J. Phys. Chem. B* **2003,** *108* (4), 1485-1490.

8. Eichenbaum, G. M.; Kiser, P. F.; Dobrynin, A. V.; Simon, S. A.; Needham, D., Investigation of the Swelling Response and Loading of Ionic Microgels with Drugs and Proteins: The Dependence on Cross-Link Density. *Macromolecules* **1999,** *32* (15), 4867-4878.

9. Huo, D.; Li, Y.; Qian, Q.; Kobayashi, T., Temperature-pH sensitivity of bovine serum albumin protein-microgels based on cross-linked poly(N-isopropylacrylamide-co-acrylic acid). *Colloids Surf., B* **2006,** *50* (1), 36-42.

10. Zhang, Y.; Zhu, W.; Wang, B.; Ding, J., A novel microgel and associated post-fabrication encapsulation technique of proteins. *J. Control. Release* **2005,** *105* (3), 260-268.

11. Johansson, C.; Gernandt, J.; Bradley, M.; Vincent, B.; Hansson, P., Interaction between lysozyme and colloidal poly(NIPAM-co-acrylic acid) microgels. *J. Colloid Interface Sci.* **2010,** *347* (2), 241-251.

12. Wu, J.-Y.; Liu, S.-Q.; Heng, P. W.-S.; Yang, Y.-Y., Evaluating proteins release from, and their interactions with, thermosensitive poly (N-isopropylacrylamide) hydrogels. *J. Control. Release* **2005,** *102* (2), 361-372.

13. Hoare, T.; Pelton, R., Charge-Switching, Amphoteric Glucose-Responsive Microgels with Physiological Swelling Activity. *Biomacromolecules* **2008,** *9* (2), 733-740.

14. Blackburn, W. H.; Dickerson, E. B.; Smith, M. H.; McDonald, J. F.; Lyon, L. A., Peptide-Functionalized Nanogels for Targeted siRNA Delivery. *Bioconjug. Chem.* **2009,** *20* (5), 960-968.

15. Dickerson, E.; Blackburn, W.; Smith, M.; Kapa, L.; Lyon, L. A.; McDonald, J., Chemosensitization of cancer cells by siRNA using targeted nanogel delivery. *BMC Cancer* **2010,** *10* (1), 10.

16. Murthy, N.; Xu, M. C.; Schuck, S.; Kunisawa, J.; Shastri, N.; Frechet, J. M. J., A macromolecular delivery vehicle for protein-based vaccines: Acid-degradable protein-loaded microgels. *Proc. Natl. Acad. Sci. U. S. A.* **2003,** *100* (9), 4995-5000.

17. Nayak, S.; Gan, D.; Serpe, M.; Lyon, L., Hollow Thermoresponsive Microgels. *Small* **2005,** *1* (4), 416-421.

18. Andersson, M.; Wittgren, B.; Wahlund, K.-G., Accuracy in Multiangle Light Scattering Measurements for Molar Mass and Radius Estimations. Model Calculations and Experiments. *Anal. Chem.* **2003,** *75* (16), 4279-4291.

19. Hoare, T.; Pelton, R., Titrametric Characterization of pH-Induced Phase Transitions in Functionalized Microgels. *Langmuir* **2006,** *22* (17), 7342-7350.

20. Stieger, M.; Richtering, W.; Pedersen, J. S.; Lindner, P., Small-angle neutron scattering study of structural changes in temperature sensitive microgel colloids. *J. Chem. Phys.* **2004,** *120* (13), 6197-6206.

21. Baselga, J.; Llorente, M. A.; Nieto, J. L.; Hernández-Fuentes, I.; Piérola, I. F., Polyacrylamide networks. sequence distribution of crosslinker. *Eur. Polym. J.* **1988,** *24* (2), 161-165.

22. Mirkin, N.; Jaconcic, J.; Stojanoff, V.; Moreno, A., High resolution X-ray crystallographic structure of bovine heart cytochrome c and its application to the design of an electron transfer biosensor. *Proteins: Struct., Funct., Bioinf.* **2008,** *70* (1), 83-92.

23. Dumetz, A. C.; Snellinger-O'Brien, A. M.; Kaler, E. W.; Lenhoff, A. M., Patterns of protein–protein interactions in salt solutions and implications for protein crystallization. *Protein Sci.* **2007,** *16* (9), 1867-1877.

24. Ricka, J.; Tanaka, T., Swelling of ionic gels: quantitative performance of the Donnan theory. *Macromolecules* **1984,** *17* (12), 2916-2921.

25. Bysell, H.; Hansson, P.; Malmsten, M., Effect of Charge Density on the Interaction between Cationic Peptides and Oppositely Charged Microgels. *J. Phys. Chem. B* **2010,** *114* (21), 7207-7215.

26. Skouri, R.; Schosseler, F.; Munch, J. P.; Candau, S. J., Swelling and Elastic Properties of Polyelectrolyte Gels. *Macromolecules* **1995,** *28* (1), 197-210.

27. Kleinen, J.; Klee, A.; Richtering, W., Influence of Architecture on the Interaction of Negatively Charged Multisensitive Poly(N-isopropylacrylamide)-co-Methacrylic Acid Microgels with Oppositely Charged Polyelectrolyte: Absorption vs Adsorption. *Langmuir* **2010,** *26* (13), 11258-11265.

28. Wong, J. E.; Díez-Pascual, A. M.; Richtering, W., Layer-by-Layer Assembly of Polyelectrolyte Multilayers on Thermoresponsive P(NiPAM-co-MAA) Microgel: Effect of Ionic Strength and Molecular Weight. *Macromolecules* **2008,** *42* (4), 1229-1238.

29. Bradley, M.; Ramos, J.; Vincent, B., Equilibrium and Kinetic Aspects of the Uptake of Poly(ethylene oxide) by Copolymer Microgel Particles of N-Isopropylacrylamide and Acrylic Acid. *Langmuir* **2005,** *21* (4), 1209-1215.

30. Mears, S. J.; Deng, Y.; Cosgrove, T.; Pelton, R., Structure of Sodium Dodecyl Sulfate Bound to a Poly(NIPAM) Microgel Particle. *Langmuir* **1997,** *13* (7), 1901-1906.

31. Hoare, T.; Pelton, R., Impact of Microgel Morphology on Functionalized Microgel−Drug Interactions. *Langmuir* **2008,** *24* (3), 1005-1012.

32. Hendrickson, G. R.; Lyon, L. A., Microgel Translocation through Pores under Confinement. *Angew. Chem., Int. Ed.* **2010,** *49* (12), 2193-2197.

33. Merkel, T. J.; Jones, S. W.; Herlihy, K. P.; Kersey, F. R.; Shields, A. R.; Napier, M.; Luft, J. C.; Wu, H. L.; Zamboni, W. C.; Wang, A. Z.; Bear, J. E.; DeSimone, J. M., Using mechanobiological mimicry of red blood cells to extend circulation times of hydrogel microparticles. *Proc. Natl. Acad. Sci. U. S. A.* **2011,** *108* (2), 586-591.

CHAPTER 7

CONCLUSIONS AND FUTURE WORK

7.1 Introduction

In this dissertation, several nanogel and microgel chemistries were investigated as multifunctional drug delivery vehicles. However, a number of problems remain for those structures that must be overcome prior to practical clinical applications. The goal of this chapter is to provide concluding remarks for those projects and propose future directions of research. This chapter also describes preliminary research (unpublished data) that may serve as a starting point to enable those research directions.

7.2 Multicompartment Nanogels for siRNA Delivery

Since the discovery of RNA interference by Fire and Mello, there has been significant excitement over the use of siRNA as a means for human therapy. The hype may be largely attributed to the billions of dollars invested by several pharmaceutical giants in the area, both in terms of R&D and the massive capital investments in securing intellectual property rights. For example, in 2006 the field was gaining momentum as Alnylam (considered a leading biotechnology company in the field) began a major partnership with Roche. Roche agreed to pay over $330 million upfront for non-exclusive rights to Alnylam's technology (and potentially more over time). Responding to the deal, Merck purchased San Francisco-based Sirna Therapeutics for a surprising $1.15 billion. However, those relationships have ultimately failed. As of 2010, Roche had terminated all efforts to discover and develop drugs based on RNAi, effectively ending the collaboration with Alnylam.[1] Despite the significant investment in Sirna Therapeutics, Merck closed that facility in February of 2011. Roche and Merck aren't alone in this struggle; Novartis and Pfizer have also curtailed their RNAi programs in recent years.

One of the primary reasons for the slow progress experienced by those companies is technological: RNAi drugs are plagued by delivery challenges. As discussed in Chapter 3, oligonucleotides are hydrophilic, negatively charged, and unable to overcome several biological hurdles to reach disease sites in vivo. Although a number of siRNA-based therapeutics having made progress in clinical trials, the majority of advanced stage trials involve either topical or direct injection of siRNA (e.g. treatment of ocular degenerative diseases), where delivery is considered less challenging.[2] Intravenously administered therapeutic formulations are limited to delivery to the liver or other MPS organs. Targeted nanoparticle carrier vehicles are expected to enable delivery to other disease sites (i.e. cancers), although the majority of those vehicles are in early stages of development.

In Chapter 3, proof-of-principle experiments showed the utility of multicompartmental nanogels for the targeted delivery of siRNA for cancer cells. The outcome of those experiments was surprising: despite the nanogels being unoptimized with regard to siRNA loading and cell targeting, the vehicles showed good efficacy in transfection with very low cell toxicity. Preliminary transfection experiments (rodent model) showed that nanogels are capable of targeting tumors via the EPR effect in vivo (data unpublished). However, high uptake at the spleen and liver suggest macrophage recognition and non-specific clearance of the vehicle from circulation. Thus, future efforts in this project are aimed to improve various characteristics of the nanogels to improve in vivo delivery, some of those include:

<u>siRNA Protection and Release.</u>

Nanogels must guard siRNA from inactivation during circulation (e.g. by clearance, aggregation, degradation) while preventing premature release. Although the hydrophilic nanogel network has shown promise for siRNA protection, the release profile imparted by the gel network will require optimization to suit specific tumor phenotypes

and physiological conditions. Furthermore, stimuli-responsive characteristics may be engineered into these materials for cell-specific, triggered release events.

Cell Targeting and Transfection.

In vivo transfection will require optimization for both passive and active targeting mechanisms. In addition, the endosomal escape mechanism for nanogels requires elucidation.

Stealth.

Recognition of particles by phagocytes remains an ongoing challenge for a variety of synthetic siRNA vectors. Whereas nanogels are hydrophilic and have shown low levels of cytotoxicity, the properties of the nanogel periphery will need optimization (e.g. via poly(ethylene glycol) grafting) to enhance tumor accumulation via EPR while avoiding clearance by immune recognition.

Tissue Penetration.

The siRNA carrier must be capable of passage within confined environments *in vivo*, including the porous vasculature of tumors and the dense extracellular matrix of the target tissue. Previous nanogel pore translocation experiments by Hendrickson et al. showed that particle softness likely enables nanogel mobility in confined areas.[3-5] We anticipate that ongoing research via the resistive pulse analysis technique will yield additional insight into those properties and how to control particle penetration into dense tissues.

Clearance and Toxicity.

In order to permit repeated administration of the vector, while limiting toxicity, it is common to impart biodegradability. We have found cross-link scission to be a convenient means to enable erosion (Chapters 4-5), which may assist in nanogel clearance while

reducing off-target effects after repeated delivery. Additionally, nanogels with triggered erosion may enable tissue-specific release in future particle formulations, where network decomposition in response to cell-specific signal would provide greater specificity towards the siRNA release. These erodible properties will need to be included in future delivery vehicle architectures.

The number of features required in these siRNA vectors is large, as illustrated by the (by no means comprehensive) list above. However, we consider multifunctional nanogels likely candidates to meet those demands. The remainder of this section discusses the current (in-progress, unpublished) efforts to optimized the nanogels for drug delivery applications.

7.2.1 Improved Cell Targeting and Stealth

Of the list of features described in the previous section, we identified cell targeting and stealth as immediate concerns for forthcoming animal trials. In Chapter 1.4.2, surface modifications to improve nanogel biocompatibility were discussed. As described in that section, poly(ethylene glycol) modification is a common method to slow protein opsonization and non-specific clearance for circulating nanoparticles. PEG molecules are very hydrophilic, flexible, and are capable of shielding nanostructures from serum proteins that may adsorb.[6-7] We hypothesized that surface modification of nanogels with high molar mass PEG would improve plasma residence for circulating siRNA delivery vehicles. Previous nanogels (described in Chapter 3) did not contain PEG. Instead, targeting peptides were bioconjugated to shell-localized primary amines by carbodiimide coupling and subsequent maleimide-thiol chemistry. In order to conjugate PEG chains with high surface density, a new bioconjugation strategy was proposed (Scheme 7.1).

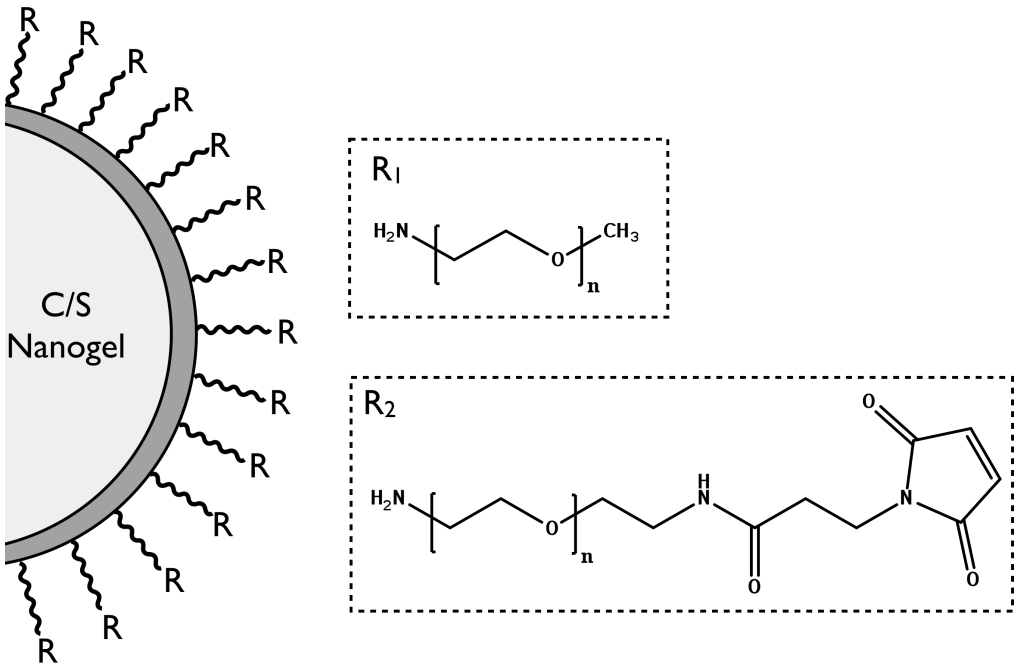

Scheme 7.1. Multicompartment nanogel platform for targeting optimization, consisting of a pNIPMAm-BIS core (light grey), and a thin pNIPMAm-BIS-AAc shell (dark grey). Particles are decorated with PEG molecules (R_1 and R_2) via carbodiimide coupling reactions.

For this new synthetic strategy, nanogels were synthesized with 5 mol% acrylic acid (AAc) in the shell for post-synthesis modification, using the "seed and feed" precipitation polymerization method. To those AAc groups, amine-functionalized PEG molecules were subsequently conjugated in excess via EDC coupling, using a similar approach as described in Chapter 3. Two bifunctional PEG molecules are shown in Scheme 7.1, either being carboxy- or maleimide-terminated (R_1 and R_2, respectively). PEG Molecule R_2 contains a maleimide group that enables thiol coupling to Cysteine-terminated targeting peptides. By changing the molar ratio of R_1:R_2 used during the EDC coupling step, the number density of peptide targeting ligands may be tuned within the final structure. Since the peptide molecules are conjugated to the terminal end of PEG, shielding of the targeting groups by PEG would be avoided.

7.2.2 Current status of nanogel optimization and delivery

Core particles were produced with the same synthetic method as described previously (Chapter 3). Instead of including APMA in the shell synthesis, AAc was added at 5 mol% of the total monomer concentration ([Total Monomer] = 50 mM). Resulting nanogels were of similar size as the previously investigated delivery vehicles: nanogels were characterized via DLS in pH 3.0 formate buffer ($r_{h,core}$ = 75 ± 1 nm, $r_{h,core/shell}$ = 79 ± 1 nm). However, the core/shell particles demonstrated pH responsivity due to the presence of acid groups in the shell ($r_{h,pH3}$ = 79 ± 1 nm, $r_{h,pH7}$ = 85 ± 1 nm). Additional titrations and electrophoretic mobility measurements are necessary to quantify total acid content in the particle shell. To investigate the effects of PEG modification alone (without peptide targeting) on macrophage recognition, nanogels were modified with R_1 only via EDC coupling of the carboxylic acid groups to the primary amines of R_1. A second batch of nanogels was coupled with R_1 and R_2 in a 4:1 ratio to serve as an initial targeted nanogel. Following conjugation, the second nanogel structure was coupled with YSA peptide (in excess to the maleimide groups present, assuming 100% yield from EDC coupling).

The nanogels will be investigated extensively over the next few months by another student in the Lyon group, who will assess peptide conjugation efficiency, perform additional physicochemical characterizations, and synthesize other carriers with varying ratios of R_1:R_2. Meanwhile, researchers in the McDonald research group (GaTech, Biology) will perform macrophage recognition assays and assess transfection *in vitro* and *in vivo* for the various carriers. Through this collaborative effort, we will likely determine improved shell chemistries for both targeting and stealth.

7.3 Role of Shell Composition in Macromolecule Encapsulation

Chapter 6 describes the tunable encapsulation of cationic proteins into anionic microgels. From that work, some of the "design rules" for macromolecule encapsulation were determined (i.e. the effects of charge and swelling on loading), which may enable the rational design of new carrier vehicles. For instance, a charged microgel core particle may be chosen for specific loading and macromolecule retention, whereas a shell material may be added to impart targeting and to shield the charges present in the core (reducing opsonization). However, little is know regarding the effects of shell addition of macromolecule encapsulation. Recently, the influence of microgel architecture on loading was investigated.

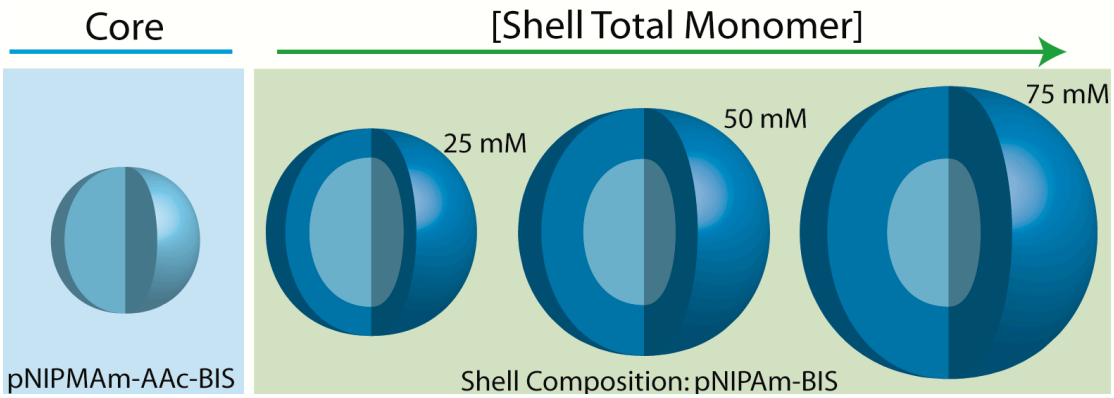

Scheme 7.2. Series of microgel structures produced by modulating the total monomer concentration in shell synthesis (from 25 mM to 75 mM).

7.3.1 Shell Synthesis

Core microgel particles were synthesized using an adapted synthetic approach from Chapter 3.2.2. However, the composition of the particles was adjusted to include AAc. The overall composition of the core particles was 68% NIPMAm, 2% BIS, and 30% AAc (140 mM = [total monomer], 8 mM = [APS] and [SDS]). A series of shells were added with varying thickness using a "seed and feed" precipitation polymerization approach. To vary the total mass of hydrogel shell added, the concentration of monomer

in synthesis was varied from 25 mM to 75 mM while maintaining a constant shell composition of 98% NIPAm and 2% BIS (Scheme 7.2). Reactions were performed by first dissolving NIPAm and BIS in distilled, deionized water. A small amount of SDS was added to each suspension to yield a total surfactant concentration of 0.3 mM. Monomer solutions were filtered through 0.2 μm Acrodisc syringe filters and subsequently added to 100 mL three-neck round-bottom flasks. To this flask, a small volume of core particles (5 mL, ~50 mg polymer) was added to serve as "seeds" to polymerize the hydrogel shell. The total volume of the reactions was 50 mL. Once equilibrated at 70 °C, the reaction mixtures were purged with N_2 for 1 hr while stirring (400 RPM). The polymerizations were initiated by delivering a 1.0 mL aliquot of 35 mM APS solution by pipette. All reactions were allowed to proceed for 24 hours under an N_2 blanket while continuously stirring. Once cooled, reaction products were filtered through 0.8 μm Acrodisc syringe filters and purified via repeated ultracentrifugation and resuspension in distilled, deionized water.

7.3.2 Core/Shell Microgel Characterization

Post synthesis characterization was perfomed via Dynamic Light Scattering (DLS), Calypso/MALS, and ζ-potentiometry using similar methods as described in Chapter 6.

Table 7.1. Characterization data for microgel core/shell particle series.

[Shell] (mM)	r_h, pH 7 (nm)	r_h, pH 3 (nm)	ρ (g/mL)	ζ-potential (mV)
0	128 ± 1	76.7 ± 0.9	0.012	-28 ± 1
25	133 ± 1	100 ± 1	0.035	-13 ± 1
50	144 ± 1	126 ± 1	0.041	-6 ± 1
75	157 ± 1	143 ± 1	0.064	-

Increasing the concentration of total monomer in shell synthesis resulted in an increase in particle dimensions under all pH conditions. The responsivity of the core

particle was found to attenuate as thicker shells are added. This effect was observed by comparing of the pH-response of the particle before and after shell addition. For instance, the radius of core particles (without an added shell) decreased by ~51 nm when the pH is decreased from pH 7 to pH 3 (Table 7.1). This response is caused by a change in the ionization of AAc groups in the core and a decrease in osmotic pressure as charges are protonated in the hydrogel. In contrast, microgels with a 75 mM shell responded by ~14 nm. Core compression effects likely cause the decrease in pH responsivity (core compression is reviewed in Chapter 1.3.2.). Core compression is also suggested by the increase in density (ρ) observed as shell thickness is increased (Table 7.1). The addition of shell decreases the electrophoretic mobility of the microgels by screening the charges imparted by the core.

Using MALS, the weight average molar mass (M_w) for microgels was characterized both in the presence and absence of 24 μM cytochrome c (cyt c). All microgels were found to load a comparable amount of protein, quantified by the total number of proteins (*#P*) loaded per sphere (the MALS method for quantifying loading is described in Chapter 6) (**Table 7.2**).

Table 7.2. Microgel molar mass was quantified in the presence or absence of cytc.

Shell Conc (mM)	M_w Unloaded (x 10^8 g/mol)	M_w Loaded (x 10^9 g/mol)	#P (x 10^4)
0	0.61 ± 0.01	0.73 ± 0.1	5.4
25	2.1 ± 0.06	1.04 ± 0.02	6.8
50	3.1 ± 0.1	1.12 ± 0.01	6.6
75	6.3 ± 0.2	1.31 ± 0.01	5.5

It is important to note that additional characterization is necessary to fully compare the microgel structures for total loading. Specifically, the total acid content for each sphere should be quantified via potentiometric titration. With knowledge of the total AAc content, the total binding per site may be depicted. Disregarding this limitation of

the experiment, the extent of loading shown in Table 7.2 is surprising. Although a significant amount of core compression occurs through shell addition (Table 7.1), microgels with thick shells appear to load a comparable amount of cyt c into their structure. Although the addition of a loosely cross-linked shell (2 mol% BIS) affects the swelling of the 30 mol% AAc core, the shells do not attenuate total loading in the microsphere.

7.3.3 Future efforts

The outcomes described in the previous section suggest that shell addition does not diminish loading within the particles. The result also suggests that shell addition can be used to decrease the surface charge of the particle (while maintaining core loading). To confirm these hypotheses, additional experiments are necessary: In addition to potentiometric titrations and additional binding experiments, assessment of the morphology of the shells is important. For instance, the shells in those studies may be deposited heterogeneously around the core particles, thus making the shells "leaky". Size and surface morphology assessment via microscopy (e.g. in-liquid atomic force microscopy or cryo-TEM) is necessary.

After completion of the shell thickness study, investigating the effects of hydrogel shell density would be an interesting avenue for research (Scheme 7.3).

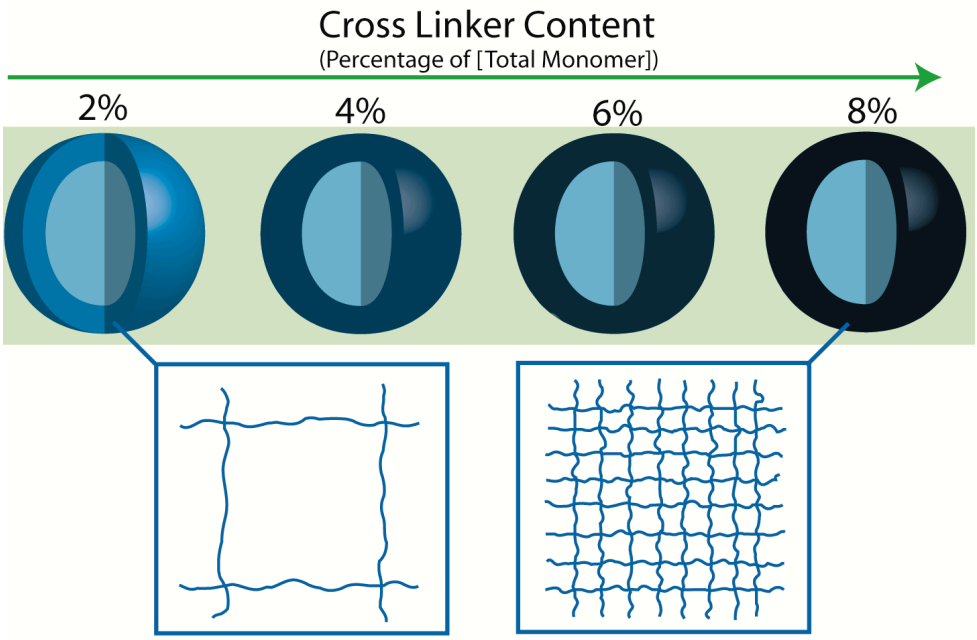

Scheme 7.3. Proposed core/shell microgel series with varied BIS content in the shell synthesis.

Increasing cross-linker concentration is hypothesized to increase network connectivity within the structures. During loading, it is likely that protein diffusivity through the shell would be decreased if the polymer segment density were increased. The protein may also be inhibited from loading via size-exclusion effects. This outcome would be highly enabling in the design of next generation carriers, where shell porosity may gate the loading and release of loaded macromolecules.

7.4 Tunable Encapsulation of siRNA within Cationic Nanogels

Previous studies demonstrated the high capacity of hydrogel particles for the encapsulation of proteins, where the resulting polymer-protein complex (induced by Coulombic interactions) was sensitive to solution ionic strength and pH. Using similar approaches, the loading of oligonucleotides into nanogels of varying charge (neutral to positive) may be studied. In contrast to positively charged cyt c studied in Chapter 6 and Chapter 7.3, siRNA molecules are negatively charged, rod-like molecules. In Chapter 2, nanogels of neutral charge were found to load a significant fraction of siRNA, as

determined by traditional centrifugation/supernatant assay methods. However, introduction of cationic charge groups into the core of those structures may greatly increase loading and retention.

7.4.1 Cationic Nanogel Synthesis

A new synthetic strategy was developed for synthesizing nanogels containing a quaternary amine-containing comonomer (i.e. [2-(methacryloyloxy)ethy] trimethylammonium chloride (DMAEMA-Q)). In contrast to previous synthetic methods used in this dissertation, the reactions required a cationic initiator 2,2'-azobis(2-methylpropionamidine)dihydrochloride (v50) and cationic surfactant dodecyltrimethylammonium bromide (DTA) to increase particle stability during the reaction. Quaternary amine groups were chosen in anticipation of producing core/shell nanogels at a later time. Similar to the previous core/shell nanogels for siRNA delivery, primary amines would be incorporated in the shell compartment (for post synthesis EDC coupling of targeting ligands). The quaternary amines in the core would not disrupt coupling to amine chemoligation sites in the shell.

Nanogel core particles were synthesized by free-radical precipitation polymerization, using a modified approach to what is described in Chapter 3.2.2.[8] The molar composition for the particles was 88% *N*-isopropylmethacrylamide (NIPMAm), 2% *N,N'*-methylenebis(acrylamide) (BIS), and 10% DMAEMA-Q with a total monomer concentration of 140 mM. Salt was added (150 mM) to adjust the ionic strength of the reaction. Previous work from our group by Hu et al. demonstrated the effects of ionic strength on the yield and size of particles during precipitation polymerization.[9] Added salt likely screens Coulombic repulsion between positively charged DMAEMA-Q units in the copolymer, which enables greater homopropagation of chains during the reaction. Block copolymers of pNIPMam and DMAEMA-Q undergo chain collapse more readily in the reaction, thus resulting in greater incorporation into the resulting nanogel. Similar

to the siRNA delivery vehicles, a small amount (0.1 mM) of acrylamidofluorescein (AFA) was added to render the nanogels fluorescent for visualization via confocal microscopy.

For the synthesis, 50 mL of a filtered, aqueous solution of NIPMAm, BIS, and DTA ([DTA] = 2 mM) was added to the reaction flask, which was then heated to 70 ºC. The solution was purged with N_2 gas and stirred vigorously until the temperature remained stable. The AFA was added, and after 10 minutes the reaction was initiated by the addition of a 1 mL solution of 100 mM ammonium persulfate (APS) to make the final concentration of APS in the reaction 2 mM. The solution turned turbid, indicating successful initiation. The reaction was allowed to continue for 4 h under an N_2 blanket.

7.4.2 Nanogel characterization and preliminary binding results

Resulting nanogels were small in radius (r_h = 76 ± 1 nm) with high size polydispersity values (Pd ≅ 30%). As described by Hu et al.,[9] high ionic strengths in the reaction results in charge-screening conditions, which may destabilize particles during the reaction and increase polydispersity values in the final product. A4F/MALS was employed to accurately assess size dispersity prior to loading experiments.

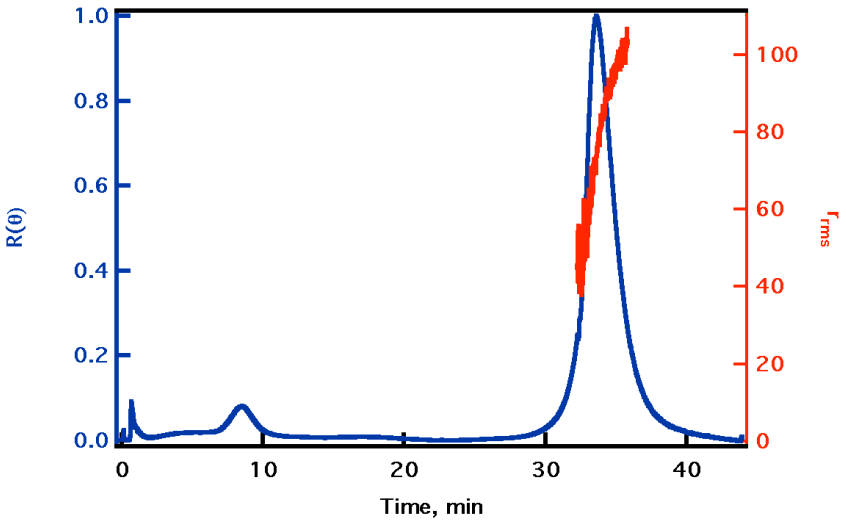

Figure 7.1 Characterization of cationic nanogel via A4F/MALS. Particle were separated in pH 7.0 phosphate buffer (ionic strength = 20 mM).

The broad distribution of nanogel sizes was determined via A4F/MALS (Figure 7.1). As can be seen in that fractogram, particle sizes ranged from 40-100 nm across the peak associated with nanogels (t_R = 34 min). We hypothesized that similar to anionic microgels (Chapter 6), the cationic nanogels would bind to oppositely charged macromolecules at low ionic strength. In a preliminary binding experiment, nanogels were characterized in the presence of lactalbumin, which is a small, anionic protein. The nanogel was mixed with increasing concentrations of lactalbumin in pH 7.0 phosphate (ionic strength = 20 mM) and subsequently characterized using the A4F/MALS method. By using A4F prior to light scattering detection, binding could be characterized despite the broad distribution of particle sizes present in the system.

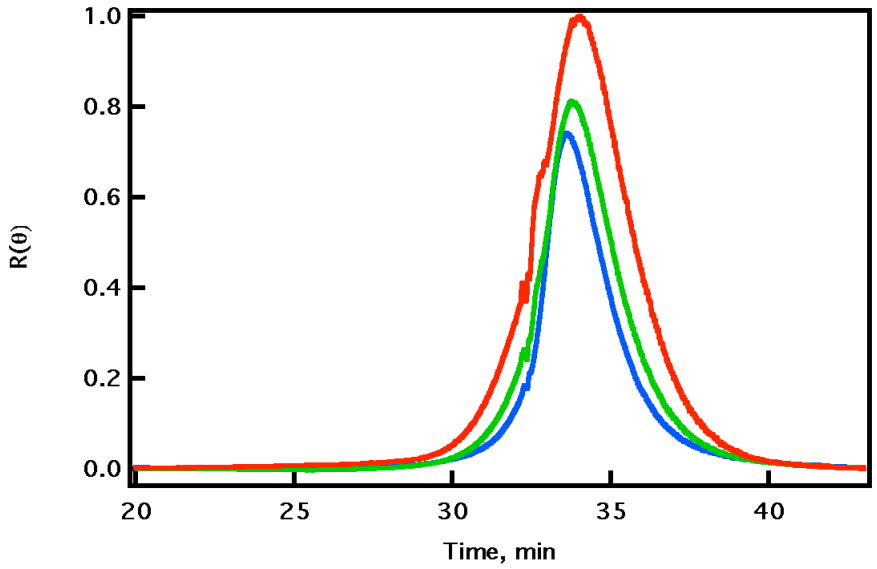

Figure 7.2 Nanogel-protein mixtures characterized via A4F/MALS in the absence (blue) or presence of 6.4 μg (green) and 32 μg (red) of lactalbumin. Particles were separated in pH 7.0 phosphate buffer (ionic strength = 20 mM) using an identical nanogel concentration.

The increase in peak area for nanogels (t_R ~34 min) may be indicative of protein loading within the structures. However, the mean r_{rms} value for the peaks increases with increasing protein concentration. The nanogels are ~77 nm without lactalbumin present (Figure 7.1). In the presence of lactalbumin (Figure 7.2), the r_{rms} increases to ~96 nm and ~102 nm for 6.4 μg and 32 μg of protein, respectfully. These results are in contrast to previously studied anionic microgels, which decrease in size due to the formation of a polymer-protein complex (Chapter 6). The increase in r_{rms} observed in this work may be caused by three factors. First, the binding of protein to the nanogel may destabilize particles in solution, resulting in the formation of aggregates that distort low angle data and thus increase the apparent r_{rms} value. Second, the protein may be binding to the periphery of the nanogels selectively, unable to access buried charges in the interior of the particle. Binding to the periphery may increase the r_{rms} since the mass distribution of scatterers would change in the particle. Third, the A4F/MALS method may be inducing protein and nanoparticle aggregation during the fractionation, distorting the subsequent data analysis.

7.4.3 Future Efforts

Preliminary experiments suggest that cationic nanogels are responsive to oppositely-charged lactalbumin. A series of experiments must be performed to investigate the nature of that response (observed in Figure 7.2). As described in the previous section, it is unclear whether the increase in scattering from nanogels is a result of protein loading, particle/protein aggregation, or both effects simultaneously.

The nanogels should be characterized offline, both in the presence and absence of protein. Through assessment without fractionation, one could determine whether A4F has a destabilizing effect on the particles or protein. Nanogels should be characterized via DLS to determine the change in r_h in the presence of lactalbumin. Assessment of the ratio of r_{rms}: r_h would provide insight into whether surface-localized binding occurs in the

particles: although a large increase in r_{rms} was observed in the data (presented in Figure 7.2), the nanogels show only a slight increase in retention via A4F, which may indicate a small increase in particle r_h from loading. For surface-localized binding, an increase in the ratio of r_{rms}:r_h would be expected. Nanogels should be characterized in the presence of other oppositely charged macromolecules, including globular proteins and oligonucleotides. We hypothesized that the nanogels would bind oppositely-charged macromolecules via Coulombic interactions. Thus, performing loading and A4F/MALS characterization at high ionic strengths and varying pH may attenuate loading in those structures. Finally, nanogels of varying charge and reduced polydispersity may be synthesized. Through repeated assessment of those particles, the "design rules" for loading a variety of cationic macromolecules would be obtained.

7.5 Closing Remarks

In this Chapter several new research directions were proposed to improve the performance of nanogels for delivery applications. For example, additional research into cationic nanogels (Section 7.4) may give rise to tunable core compartments for those vehicles, where siRNA or protein encapsulation may be modified by the concentration of charged groups within the network. To those cores, PEG containing shells may be added (Section 7.2), where the ratio of targeting and stealth characteristics can be modulated through the ratio of coupled ligands on the surface. The effects of adding those shells to the core nanogels may be anticipated through additional research in Section 7.3. Thus, these projects together may enable new generations of nanogels, each with tunable features for various drug delivery applications.

7.6 References

1. Schmidt, C., RNAi momentum fizzles as pharma shifts priorities. *Nat. Biotechnol.* **2011,** *29* (2), 93-94.

2. Kim, D. H.; Rossi, J. J., Strategies for silencing human disease using RNA interference. *Nat. Rev. Genet.* **2007,** *8* (3), 173-184.

3. Hendrickson, G. R.; Lyon, L. A., Microgel Translocation through Pores under Confinement. *Angewandte Chemie-International Edition* **2010,** *49* (12), 2193-2197.

4. Holden, D. A.; Hendrickson, G.; Lyon, L. A.; White, H. S., Resistive Pulse Analysis of Microgel Deformation During Nanopore Translocation. *J. Phys. Chem. C* **2011,** *115* (7), 2999-3004.

5. Holden, D. A.; Hendrickson, G. R.; Lan, W. J.; Lyon, L. A.; White, H. S., Electrical signature of the deformation and dehydration of microgels during translocation through nanopores. *Soft Matter* **2011,** *7* (18), 8035-8040.

6. Gref, R.; Domb, A.; Quellec, P.; Blunk, T.; Muller, R. H.; Verbavatz, J. M.; Langer, R., The Controlled Intravenous Delivery Of Drugs Using PEG-Coated Sterically Stabilized Nanospheres. *Adv. Drug Delivery Rev.* **1995,** *16* (2-3), 215-233.

7. Otsuka, H.; Nagasaki, Y.; Kataoka, K., PEGylated nanoparticles for biological and pharmaceutical applications. *Adv. Drug Delivery Rev.* **2003,** *55* (3), 403-419.

8. Blackburn, W. H.; Lyon, L. A., Size-controlled synthesis of monodisperse core/shell nanogels. *Colloid Polym. Sci.* **2008,** *286* (5), 563-569.

9. Hu, X. B.; Tong, Z.; Lyon, L. A., Synthesis and physicochemical properties of cationic microgels based on poly(N-isopropylmethacrylamide). *Colloid Polym. Sci.* **2011,** *289* (3), 333-339.

VITA

MICHAEL H. SMITH

Michael was born in White Plains, NY. He attended high school at Proctor Academy (Andover, NH), where he found a passion for snowboarding, tennis, and chemistry. At Wheaton College (Norton, MA), Michael obtained his B.A. in Chemistry and a minor degree in Biology. Michael enrolled at Georgia Tech in the Fall of 2007 and began research with Professor L. Andrew Lyon that winter. When out of the lab, Michael enjoys spending time with his wife, Sarah, walking their dog, "Betty", and playing guitar. Following graduation, Michael will be conducting drug delivery research at Merck & Co., Inc. (West Point, PA).